NOTE TO USERS

ACTIVE MACH-ZEHNDER INTERFEROMETERS WITH FEEDBACK

by

Ronnie Francis Van Dommelen

Submitted
in partial fulfillment of the requirements
for the degree of

DOCTOR OF PHILOSOPHY

Major Subject: Electrical and Computer Engineering

at

DALHOUSIE UNIVERSITY

Halifax, Nova Scotia August 9, 2005

Your file Votre référence
ISBN: 0-494-13056-3
Our file Notre référence
ISBN: 0-494-13056-3

DALHOUSIE UNIVERSITY

To comply with the Canadian Privacy Act the National Library of Canada has requested that the following pages be removed from this copy of the thesis:

Preliminary Pages
- Examiners Signature Page
- Dalhousie Library Copyright Agreement

Appendices
- Copyright Releases (if applicable)

To Jennifer

Table of Contents

List of Figures

List of Tables

List of Symbols and Abbreviations

Greek Symbols

α	waveguide loss [cm^{-1}]
α_N	linewidth enhancement factor
α'	total attenuation/gain coefficient [cm^{-1}]
β	propagation constant [rad m^{-1}]
$\tilde{\beta}$	propagation constant [rad m^{-1}]
β_m	mth derivative of propagation constant
β'	real valued propagation constant [rad m^{-1}]
γ_1	material gain constant [cm^{-1} nm^{-2}]
γ_2	material gain constant [cm^{-1} nm^{-3}]
$\Delta\eta$	refractive index change
$\Delta\theta$	optical phase difference measured between arms of MZI [rad]
$\Delta\tau$	time delay of input pulses in differential XPM [s]
$\Delta\phi$	phase change imparted by SOA [rad]
$\Delta\omega$	spectral width of optical input [rad s^{-1}]
ε	displacement from stable or metastable operating point [W]
ϵ_0	permittivity of free space [F m^{-1}]
ϵ_b	dielectric constant of the unpumped material
ϵ	complex dielectric constant
η	refractive index
η_g	group refractive index
η_b	refractive index of the unpumped material
κ_0	peak material gain shift constant [nm cm^{-3}]
λ	wavelength [nm]
λ_0	peak material gain wavelength at transparency [nm]
λ_N	peak material gain shift [nm]
λ_{CW}	wavelength of CW input to MZI [nm]
μ_0	permeability of free space [H m^{-1}]
ν_i	frequency [rad s^{-1}]
ν_g	group velocity [m s^{-1}]
θ	facet angle [degrees]
σ	conductivity [Ω^{-1} m^{-1}]

τ_N	spontaneous emission carrier lifetime [s]
Γ	confinement factor
ϕ	phase of the optical input [rad]
χ	susceptibility
χ_0	unpumped susceptibility
χ_p	susceptibility due to pumping
χ'	dummy variable used to collect various susceptibility terms
ω	frequency [rad s^{-1}]
ω_0	center frequency of optical input [rad s^{-1}]

Roman Symbols

a	differential gain or material gain constant [cm^2]
A	nonradiative recombination rate [s^{-1}]
$A(z,t)$	envelope of optical input
APR	arm power ratio
b	transfer function offset [W]
B	bimolecular recombination rate [$cm^3\ s^{-1}$]
c	speed of light in a vacuum [m s^{-1}]
C	Auger recombination rate [$cm^6\ s^{-1}$]
$\tilde{E}$	complex electric field amplitude [V m^{-1}]
$F(x,y)$	optical field distribution
g	material gain [cm^{-1}]
$g_{N,i}$	material gain [cm^{-1}]
$\tilde{G}(z,\omega)$	optical field, frequency domain
$\tilde{G}_0(\omega)$	optical field at input to SOA
$G(z,t)$	optical field, time domain
G	input-to-output gain of an SOA
G_{MAX}	gain of SOA at ripple peak
G_{MIN}	gain of SOA at ripple trough
G_{fb}	lumped optical gain in feedback loop
h	Planck's constant [J s]
I	electrical current [A]
I_{SOA}	injection current into the feedback SOA [A]
$Input$	optical input (either two or three level) to SOA gate [W]
k_0	wavenumber in free space [cm^{-1}]
L	length of SOA active region [cm]
m	slope of the transfer function
n	number of passes of the optical feedback loop

n_1	refractive index of waveguide core
n_2	refractive index of waveguide cladding
N	carrier density [cm^{-3}]
N_0	carrier density at transparency [cm^{-3}]
N_{ph}	photon density in active region [cm^{-3}]
Output	optical output from any SOA gate [W]
P	power [W]
P_{Cross}	power of steady state operating points [W]
P_i	optical power into a modulated SOA [W]
P_{In}	MZI input power used to study stable operating points [W]
P_{lower}	power in lower arm of MZI immediately before output [W]
P_{Out}	MZI output power used to study stable operating points [W]
P_{total}	power at the interferometer output [W]
P_{upper}	power in upper arm of MZI immediately before output [W]
q	electron charge [C]
R	carrier recombination rate [$cm^{-3}\ s^{-1}$]
$R_{1,2}$	SOA facet reflectivities
R_g	power reflection coefficient
Reset	optical signal used to reset a flip-flop [W]
R_{st}	stimulated emission rate [s^{-1}]
S	transverse cross sectional area of SOA active region [cm^2]
Set	optical signal used to set a flip-flop [W]
t	time [s]
Three-Level	three power-level optical input signal into Three-Level flip-flop [W]
TL	see *Three-Level* [W]
w_{full}	mode full power width [nm]
V	volume of SOA active region [cm^3]
$\hat{\mathbf{x}}$	polarization unit vector
z	longitudinal axis of an SOA [cm]
z'	dummy variable

Abbreviations and Acronyms

ASE	amplified spontaneous emission
CIPI	Canadian Institute for Photonic Innovations
CSD	critical slowing down
CW	continuous wave
DVD	digital video disc
EDFA	erbium-doped fiber amplifier
FBG	fiber Bragg grating
FWHM	full-width half-maximum
FWM	four wave mixing
IP	internet protocol
LD	laser diode
MI	Michelson interferometer
MZI	Mach-Zehnder interferometer
NRZ	non-return-to-zero
OTDM	optical time division multiplexed
PC	polarization controller
PM	polarization maintaining (fiber)
RZ	return-to-zero
SLALOM	semiconductor laser amplifier in a loop mirror
SOA	semiconductor optical amplifier
TE	transverse electric
TLI	three-level-input
TM	transverse magnetic
TOAD	terahertz optical asymmetric demultiplexer
XGM	cross-gain modulation
XPM	cross-phase modulation
UNI	ultrafast nonlinear interferometer
WDM	wavelength division multiplexed

Acknowledgments

I would like to extend very special thanks to my supervisor, Dr. Michael Cada. Thank you for your encouragement and support, suggestions and ideas, time and trust, patience and proofreading. It has been a great learning experience with you over the years, and very rewarding.

I am also very grateful to Dr. John Cartledge at Queen's University, for allowing me to visit for five weeks in early 2004. It was an exciting learning experience and very satisfying to be able to bring ideas into fruition. I appreciate the time of both Dr. Cartledge and his students, particularly David Krause and Iannick Monfils. In the same way I would like to thank Dr. Harold Haugen of McMaster University for allowing me to visit and prepare SOA samples, and Michael Brennan, for sharing his time and expertise. Thanks also to Dr. Haugen for the donation of those samples to our lab.

To all my friends in the Photonics Applications Lab; a fun and friendly atmosphere makes everything more enjoyable. Special thanks to Sean Nutter and Ellis Barefoot for sharing in the excitement and for those productive brainstorming sessions. You contributed greatly to this thesis.

Endless thanks to my family for their love and encouragement. To my parents for always being there and to my wife, Jennifer, for always making me happy.

Financial support from the CIPI (Canadian Institute for Photonic Innovations), eMPOWR-NSERC (Microelectronics, Photonics, Optoelectronics, Wireless and Radio Engineering - Natural Sciences and Engineering Research Council of Canada), Dalhousie University, and Dr. Michael Cada is gratefully acknowledged.

Abstract

The integrated active Mach-Zehnder interferometer (MZI) has received considerable attention in recent years for use as a wavelength converter or to perform logical functions. Such devices are foreseen as being important in the design of all-optical routers for high-speed long-haul fiber communications systems. This thesis considers several designs in which external feedback is applied to the same MZI.

Under proper operating conditions bistability is observed and the system can be used as an all-optical memory. Several system variations were studied using a numerical model. Both static and dynamic characteristics were investigated. A previously patented memory design based on an MZI is shown to be impractical due to limitations imposed on the resetting input signal. A second memory design is shown to suffer from critical slowing down. A third proposed design is shown to avoid the problems associated with the first two designs. In addition to the numerical simulations, a simple linear model and a graphical approach are developed to explain some of the dynamic system behaviors. Numerical simulations and the linear model are also applied to the design and stability analysis of an optical ring oscillator.

Experimentally, both single bit flip-flop and multi-bit buffer-type memory designs were constructed. It is postulated that sub-optimal electrical and optical biasing conditions limit the observed transient response times and contribute greatly to the observed noise levels. Critical slowing down is also experimentally investigated in a controllable manner. An all-optical ring oscillator is demonstrated. Finally, simple digital electric circuits that are functionally equivalent to the optical memory designs are used to validate numerical simulation results.

The major original contributions of this thesis are the newly proposed all-optical flip-flop and buffer memories, including the design, numerical simulation, electrical equivalent-circuit simulation, and experimental testing. Other contributions include the design and testing of the all-optical oscillator and the use of a simple graphical analysis to explain the operation of the oscillator and the optical memory designs.

CHAPTER

1

INTRODUCTION

Modern optics has an enormous, if often overlooked, impact on our daily lives. From bar code scanners, to compact disc and DVD technology, to fiber optic communications, semiconductor and silica-fiber optical technologies play an important role in many recent inventions.

At the same time as these products have become commonplace, people have been dreaming of optical computers, envisioning computation 'at light speed' [CNN03]. Unfortunately, serious technological hurdles such as miniaturization of sources and waveguides prevent us from developing an optical desktop computer in the foreseeable future. As well, electronics continues to advance at an amazing pace, with terahertz transistors now possible [AMD01], making it difficult for optical computing to maintain a speed advantage. Nonetheless, there are some exceptions in which optics can be used to provide an advantage over electronics.

The first situation for which optics is ideally suited is in the area of massively parallel calculations. The bosonic nature of light allows complex mathematical functions, such as the Fourier transform, to be carried out on two-dimensional images, using relatively simple hardware. Applications include cross-correlation systems for image matching and recognition [STAR99], and target tracking systems [LANE00].

Another situation where optics has an advantage over electronics is in digital optical fiber communication systems. In this case information is already in optical

form as it is transported from router to router as it passes though the network. In systems today, the routing is still done electronically, however, system designers would prefer an all-optical network [JOUR01, ROBE99a]. Performing packet routing and related calculations in the optical domain reduces the complexity by eliminating optical and electronic domain conversions. It also allows more flexibility in the system design. Such optical packet processing is not necessary everywhere in the system, but mostly for the very high throughput network backbones. It is this application that is of interest in this thesis.

1.1 MOTIVATION

This thesis began as a research project within the Canadian Institute for Photonic Innovations (CIPI). The objective was to study and use the nonlinearities associated with semiconductor optical amplifiers (SOAs) to an advantage. These devices are very similar in form to laser diodes, the major difference being that laser diodes are a light source, while SOAs are light amplification devices.

The project focussed on the application to communications systems and in particular on digital signal processing within these systems. This is a very active field of research worldwide because of the potential benefits that it can provide including increased flexibility, reduced complexity, and increased performance. The topic of research shifted somewhat over time, beginning with the process of four-wave mixing and the development of a family of logic gates for processing wavelength encoded data [VAND00a, VAND00b]. It later moved to the process of cross-phase modulation in Mach-Zehnder interferometers with SOAs in each arm (MZI-SOAs) and their application to all-optical memory elements [VAND001, VAND002, VAND003].

Optical memory is a basic building block for any optical serial digital signal processing circuitry. Many designs have been proposed over the last few

decades, but none has proven to be ideal [KAWA97, ZHOU97, POUS98a, MANN99, HILL01]. The primary objective of this thesis is to present a new hardware arrangement that can be used as a single bit or multi-bit optical memory. It is felt that the designs presented in this thesis are an important addition to the various all-optical memories developed thus far. In particular, they rely on an active Mach-Zehnder interferometer, with nonlinear semiconductor optical amplifiers in each arm. These devices have been commercially available and much research has been carried out with them for use in related applications such as wavelength converters and all-optical logic gates. In this thesis, feedback is applied to the interferometer to allow it to be used as a memory element. Benefits include the development of a single technology for use in multiple end products, improved interoperability due to a common building block, and economy of scale.

1.2 CONTRIBUTIONS

In this thesis several contributions are made to the topic of active Mach-Zehnder interferometers with feedback, both in the theoretical understanding and in the development and experimental verification of new memory designs.

The major contribution of this thesis was the design and experimental verification of an all-optical memory based on an active Mach-Zehnder interferometer with feedback. The hardware arrangement was shown to work in two ways: as a single-bit flip-flop type memory and as a buffer-type memory for storing packets with full read/write capability. One important benefit of these memory designs, over existing memories based on other methods, is the ability to handle non-return-to-zero (NRZ) format data as well as return-to-zero (RZ) data. Many competing designs are limited to RZ operation only. In addition, the flip-flop is bit-rate independent, and the buffer-type memory can handle a wide

range of bit-rates. Both of the memories offer many of the benefits associated with MZI-SOAs and cross-phase modulation. These include low sensitivity to input wavelength and input power. Although the prototype was sensitive to input polarization, it is not inherently so, and future improvements in MZI design may allow the designs to be polarization insensitive.

In addition to these proposed memory designs, two other flip-flop designs were studied. The first was a previously patented design [ROBE99b]. Through a general understanding of the operation of the device and supported by numerical simulations, the design is shown to suffer from serious practical operating limitations. Specifically, resetting the flip-flop can cause the device to begin oscillating. A second flip-flop design was also studied. It provided an excellent opportunity to study what is known as critical slowing down. This is an effect that limits the switching time of bistable devices to values longer than the fundamental carrier-lifetime limited switching times. Finally, an all-optical ring oscillator was investigated theoretically, numerically simulated, implemented and experimentally verified.

In the analysis of these various hardware arrangements, numerical simulations were carried out using self-coded programs written for *Mathematica* and designed for the purpose. The programs are based on carrier-rate equations and travelling wave equations and allow both static and dynamic behavior of the MZIs to be simulated. In addition, a very simple graphical method is proposed that uses the transfer functions of the MZIs in the design and understanding of the behavior of the feedback devices. This includes the effects of critical slowing down, noise, and the general operation of the memory elements.

Finally, electrical circuits that were functionally equivalent to the patented flip-flop and the proposed flip-flop were constructed and tested. It was shown that these circuits operated as predicted by the numerical simulations.

1.3 SCOPE

The thesis presents several hardware arrangements based on a Mach-Zehnder interferometer with feedback. Numerical models were developed to aid in the development of the different memory designs and to understand their basic behavior. Those designs that could be built with the hardware available were implemented and experimentally verified. The purpose was not to optimize the memory operation as there are numerous design parameters that can be varied, while the available hardware allowed only certain parameters to be controlled. However, some suggestions for possible design improvements are given in the concluding chapter. A complete numerical model of the memory designs would be exceedingly complex, so a simplified model was used. In addition, being a commercial device, the details of the MZI were unknown. So, while the results of the model do not precisely match the experimental data, the two are consistent.

1.4 ORGANIZATION

An introduction to semiconductor optical amplifiers is given in Chapter 2. Construction of discrete amplifiers and related design issues are discussed. Strategies for the integration of amplifiers and waveguides on an optical chip in the form of a Mach-Zehnder interferometer are briefly considered. The nonlinear behavior of the amplifiers is described. Particular attention is given to how the nonlinearity is used in functional devices. Techniques such as cross-gain modulation, cross-phase modulation, and four wave mixing are introduced.

The applied topic of digital optical signal processing of serial data is covered in Chapter 3. The various functional devices that have been created from MZI-SOAs for use in fiber communication systems are discussed. Competing optical memories based on bistable laser diodes, terahertz optical asymmetric

demultiplexers, and ultrafast nonlinear interferometers are presented. The chapter ends with a description of how such memories can be used for optical packet switching.

A numerical model, and simulation results based on this model, are detailed in Chapter 4. The model is based on a carrier rate equation and a travelling wave equation. Simulation results are first given for a single SOA. Next, a complete Mach-Zehnder interferometer, using cross-phase modulation, is simulated. Feedback is then applied to the MZI. A patented flip-flop is simulated and shown to be unsuitable for practical use due to oscillations that can occur when the device is reset. A second flip-flop design is presented that suffers from critical slowing down when reset. The critical slowing down is considered in further detail with a simple linear mathematical model and graphical method. Finally, a third flip-flop hardware arrangement is proposed and analyzed.

Experimental results, using an Alcatel integrated active MZI are presented and discussed in Chapter 5. Static behavior of the MZI with and without feedback is investigated. The proper operation of the proposed flip-flop is shown. Related topics such as rise and fall times, critical slowing down, and noise are treated in detail. The same hardware arrangement is also shown to operate as a buffer-type memory. Results showing the full read/write capability are given. Results are then given for a modified hardware setup, in which the MZI with feedback operates as a ring oscillator.

In Chapter 6, conclusions are given and the main contributions are summarized. Suggestions for future work are discussed.

CHAPTER

2

SEMICONDUCTOR OPTICAL AMPLIFIERS

This chapter reviews the topic of semiconductor optical amplifiers (SOAs). In the introduction, the reasons for the development of SOAs are given, in relation to the co-development of another optical amplifier, the erbium doped fiber amplifier. The construction and operation of basic SOAs is described. Strategies for the integration of amplifiers and waveguides on an optical chip in the form of a Mach-Zehnder interferometer with SOAs in each arm are considered. Packaging issues are also briefly considered. Next, the nonlinear behavior of the amplifiers is described in the context of how it can be exploited for use in signal processing applications. The principles of cross-gain modulation and cross-phase modulation are examined in detail. Two other concepts, differential cross-phase modulation and four wave mixing, are also briefly described.

2.1 INTRODUCTION

Fiber-based optical amplifiers revolutionized high-throughput wavelength division multiplexed (WDM) fiber communication systems [AGRA92 pg. 6]. Prior to the 1980s, a single channel needing amplification had to be converted to an electrical signal, amplified electronically, and retransmitted using another laser. If

multiple wavelength multiplexed channels were used on the fiber they needed to be separated and amplified individually, then retransmitted using multiple lasers and optically multiplexed at the output. In 1987, the erbium doped fiber amplifier (EDFA) was invented. The EDFA works by pumping a segment of erbium doped fiber with an out-of-band laser diode operating at 980 nm. This device allowed the multiple channels to be amplified simultaneously and without the need for optoelectronic conversions. The economic benefits have made the EDFA hugely successful. In addition to allowing higher aggregate bit rates in new systems, it also allowed older single channel systems to be upgraded to WDM systems without the need to lay additional fiber.

Even before the EDFA was invented, semiconductor optical amplifiers were well known [CONN02]. In its simplest form, the SOA is simply a laser diode without feedback, providing gain to an optical signal passing through it. The SOA did not have such an impact as the EDFA for various reasons. Early on, there was a difficulty in reducing the feedback to levels low enough to prevent wavelength dependent cavity resonance effects [OMAH88]. Another early problem was polarization dependence [OLSS92]. These problems have been overcome but the SOA still suffers from a low gain-saturation. The EDFA is far more linear and can amplify larger input powers. This linearity is very important when considering that in a WDM system, several channels will be amplified. The linearity is required to avoid crosstalk [OLSS92]. These are important considerations for long-haul systems. However, for so-called metro applications SOAs are finding a niche. In these city-wide systems, the shorter transmission distances mean that lower optical powers can be used, allowing the SOA to operate as a linear device. Another advantage of SOAs over EDFAs in metro applications is that they can be made cheaper because they are powered directly from an electrical source, while EDFAs are optically pumped, requiring additional hardware [STUB00].

While a low saturation power can be a problem for simple amplifiers, it can be used to great benefit in designing other, higher functionality devices such as wavelength converters, signal regenerators, logic gates, and memories. This is where considerable research has been conducted since the late 1980s.

2.2 SOA STRUCTURE

The laser diode (LD) and the SOA are very similar in structure. Both use an electrically pumped semiconductor p-n junction to provide optical gain. The principal difference is that the laser diode requires feedback while the SOA typically aims to have no feedback.

A depiction of a LD/SOA structure that was grown at McMaster University is shown in Figure 2-1 [WALL01]. While it was not used for any of the experiments in this thesis, it illustrates a typical structure used. In addition, the author had

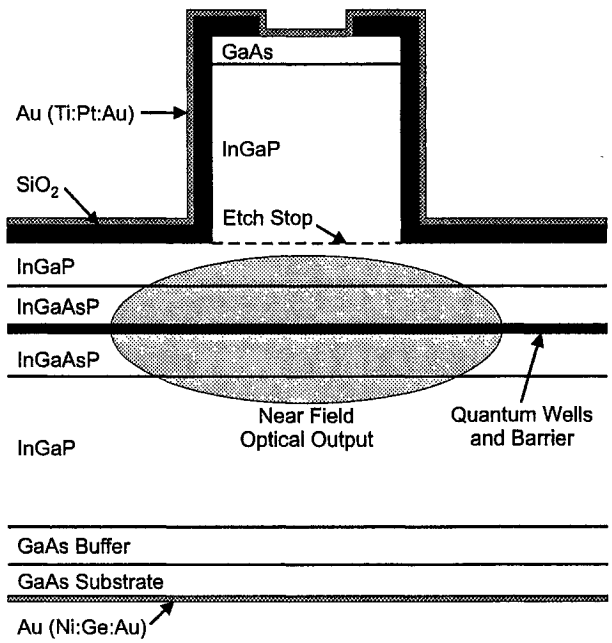

Figure 2-1 The structure of a laser/SOA from McMaster University as an example of an SOA structure. Redrawn from [WALL01].

some experience preparing these particular devices. The structure uses a ridge waveguide for lateral confinement, contains two quantum wells, and operates at roughly 980 nm.

In the case of a laser diode, the structure is grown such that the ridge is parallel to one of the crystallographic axes of the semiconductor medium, as shown in Figure 2-2. Strips of the wafer are then cleaved to form atomically smooth facets perpendicular to the ridge. Reflection from the facets, due to the change in refractive index between the semiconductor and air, provides sufficient feedback for lasing action.

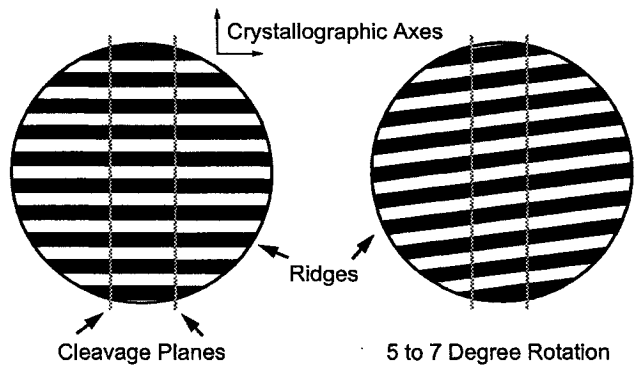

Figure 2-2 Illustration of how rotation of the mask during the growth of the device allows the ridge to be oriented at a small angle to the crystallographic axes, for the purpose of reducing the feedback at the facets for improved SOA operation.

In the case of an SOA, feedback can be suppressed by simply rotating the mask that defines the ridge during the growth process. For the light reflected at the semiconductor-air boundary, this reduces the coupling back into the waveguide as illustrated in Figure 2-3. The detailed relationship between the power reflection coefficient and the facet angle (and waveguide width) is rather complex [MARC89], but to a limited degree can be approximated by

$$R_g = \frac{n_1 \cos\theta - \sqrt{1 - n_1^2 \sin^2\theta}}{n_1 \cos\theta + \sqrt{1 - n_1^2 \sin^2\theta}} \exp\left[-\left(\frac{2\pi n_2 w_{full} \theta}{\lambda_0} \right)^2 \right] \qquad (2.1)$$

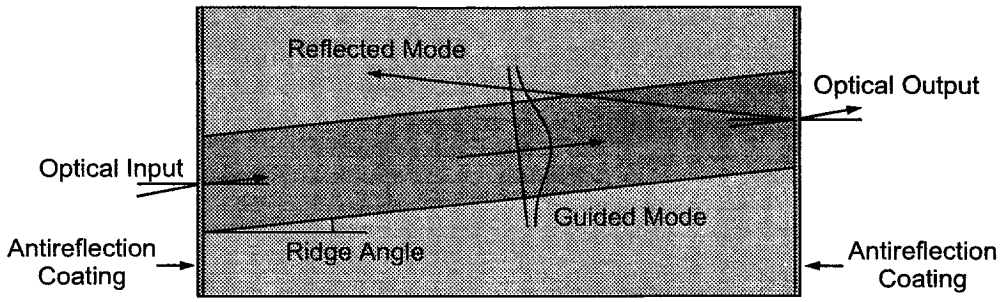

Figure 2-3 Top view of the cleaved SOA showing the reduction in the reflected-mode coupling back into the waveguide. Antireflection coatings are also shown. Adapted from [WALL01].

where n_1 and n_2 are refractive indices of the waveguide core and cladding, θ is the facet angle, w_{full} is the mode full power width, and λ_0 is the free space wavelength. The first fraction accounts for the Fresnel reflection at a semiconductor-air boundary. It should be noted that the approximation is a continuously decreasing function while the detailed function is not. Both are compared in [MARC89]. While large facet angles are desirable for reduced reflectivity, they complicate coupling and antireflection coating design [CONN02 pg. 29]. An angle of approximately 7° between the ridge and the crystallographic axis is typically used.

To reduce feedback levels still further, antireflection coatings are applied to the facets of the device [WALL01]. An uncoated semiconductor-air boundary has a reflectivity of about 32%; an optimized single layer antireflection coating can reduce it to about 10^{-3} to 10^{-4}. The reduction in reflectivity depends on the thickness and refractive index of the coating. One material that is used for this purpose is silicon oxynitride, SiO_xN_y. It is evaporated onto the facets of the device using chemical vapor deposition. The amount of oxygen and nitrogen in the film determines the refractive index of the material. The range of refractive indices possible is from 1.46 to 3.4. An ellipsometer is used to measure the thickness of the film. At McMaster University the ellipsometer was separate from the deposition machine and the thickness of the films were measured after they

were grown. In more advanced deposition chambers, an ellipsometer is built into the unit allowing active measurement of the film thickness as it is being grown. Single layer antireflection coatings tend to be polarization sensitive and optimized for a single wavelength only. Better results can be achieved through multilayer coatings; however, these are far more difficult to analyze [CONN02].

Other methods of reducing feedback are through the use of waveguides that flare out near the facets and so-called window facets or buried facets, in which transparent semiconductor extends beyond the end of the active waveguide [AGRA95, CONN02]. In each case, the idea is to allow the propagating mode to spatially expand before reaching the facet. In this way, little reflected light is coupled back into the waveguide.

These various methods for reducing the facet reflectivity can be combined to improve performance. A travelling wave amplifier is classified as one in which the residual Fabry-Perot gain ripple is less than 3 dB. Thus

$$\frac{G_{MAX}}{G_{MIN}} = \left(\frac{1+G\sqrt{R_1 R_2}}{1-G\sqrt{R_1 R_2}} \right)^2 < 3\,\text{dB}, \tag{2.2}$$

where G is the input-to-output gain of the SOA and R_1 and R_2 are the reflectivities of each facet [AGRA95 pg. 250], which simplifies to $G\sqrt{R_1 R_2} < 0.17$. This type of amplifier is relatively wavelength insensitive. If the gain ripple is greater than 3 dB, then the amplifier is classified as a Fabry-Perot amplifier.

For many applications it is desirable to have a polarization insensitive amplifier. When the SOA is fiber pigtailed using standard non-polarization maintaining fiber, it is important to provide fixed gain to an incoming signal regardless of the incoming polarization. As an example, the datasheet for a commercial SOA from Axon Photonics specifies a polarization dependent gain of less than 0.1 dB. At least two methods exist for creating a polarization insensitive SOA. The first involves controlling the transverse dimensions of the active region [CONN02]. In this way the confinement factors, and thus the gains

in the TE and TM directions can be adjusted [OMAH88]. A second, more common method uses strained quantum wells [YAMA95].

2.3 PACKAGING AND INTEGRATION

When used as a stand alone device, the SOA will generally be packaged in a hermetically sealed, fiber pigtailed case. A thermoelectric Peltier cooler and a temperature sensor such as a thermistor are used to maintain the SOA at the desired operating temperature. A variety of lenses can be used to provide optical coupling between the fiber and semiconductor waveguides, including aspheric lenses, ball lenses, and graded index lenses.

One advantage of SOAs over fiber amplifiers is that they can be integrated on a chip with other components. Of interest in this thesis is an integrated Mach-Zehnder interferometer (MZI) with an SOA in each arm of the interferometer. A bulk version of this type of interferometer is extremely sensitive to shock and temperature variations due to the separate paths that the light follows in each arm. For this reason, practical MZI-SOAs must be integrated on a chip. Devices such as these were reported in the mid 1990s [DURH94, PAN95]. More ambitious designs also integrate a continuous wave (CW) input laser [SPIE98]. Because integration of optical devices is in its infancy, there are still technological challenges to be overcome. Nonetheless, there is much promise in the area.

In the case of the MZI, designers would ideally like to have discrete SOAs connected with passive waveguides. This is very difficult to do, thus the whole chip is usually active. This is the case for the device used in this thesis that was previously commercially available from Alcatel. The whole device is an MZI shaped SOA. Functionality is achieved by segmenting the metal electrical contacts on the surface of the device. In this way the currents supplied to different areas of the device can be controlled independently. This type of

device, being monolithic, can be produced in a straightforward fashion. The alternative is to combine discrete active SOAs with passive waveguides [SPIE98]. Use of hybrid technologies such as SOAs and polymer waveguides may be a viable option [FAN98]. Work continues in this area with good results being reported recently [SATO04].

2.4 EXPLOITING THE NONLINEAR SOA

As mentioned in the introduction, SOAs have proven to be unsuitable for in-line amplification in WDM systems because of a low saturation power. Instead, researchers have used this nonlinearity as an advantage for other applications. A nice overview of nonlinear SOAs is given by [ADAM95]. This section considers the three most common methods used to exploit the nonlinear SOA. These are cross-gain modulation (XGM) [VAND01], cross-phase modulation (XPM) [VAND01], and four-wave mixing (FWM) [VAND00a]. Extra attention will be given to XPM which is the focus of this thesis and to the technique of XGM which is necessary for the understanding of XPM. Differential cross-phase modulation and FWM will also be discussed. Another technique, cross-polarization modulation will not be discussed [SOTO99], as it has received little attention in the literature.

2.4.1 Cross Gain Modulation (XGM)

This technique relies directly on gain saturation in the SOA. Because the saturation power of an SOA is relatively small, compared to other amplifiers such as the erbium doped fiber-amplifier, it is well suited to perform cross-gain modulation (XGM) [OLSS92]. In this technique, two optical inputs are used. The first is an amplitude modulated input signal that is to be processed. The other is an unmodulated, or continuous wave (CW) signal. These are often referred to as

the pump and probe, respectively. The intense input signal (pump) modulates the carrier density, and thus the gain of the SOA. The CW probe input experiences this modulated gain and thus the probe amplitude is modulated at the output of the SOA. The modulation of the gain is clear from a gain saturation curve shown in Figure 2-4. The exact relationship between the input intensity, carrier density, and gain is treated mathematically in Chapter 4.

The pump and probe may be launched into the SOA such that they travel in the same direction or in opposite directions, as shown in Figure 2-5. These two variations are referred to as co-propagation and counter-propagation schemes, respectively. The co-propagation scheme requires a filter to separate the pump from the probe. The counter-propagation scheme does not need a filter and allows the pump and probe to operate at the same wavelength, if required. This is advantageous for wavelength conversion applications where a signal may only occasionally need to be switched to a new wavelength.

A clear benefit of XGM is the simplicity; only one SOA is required. One drawback is extinction ratio degradation [DUUR96]. The output signal will always have a smaller extinction ratio than the input when converting the input signal to the same or a longer output wavelength. This limits the number of converters

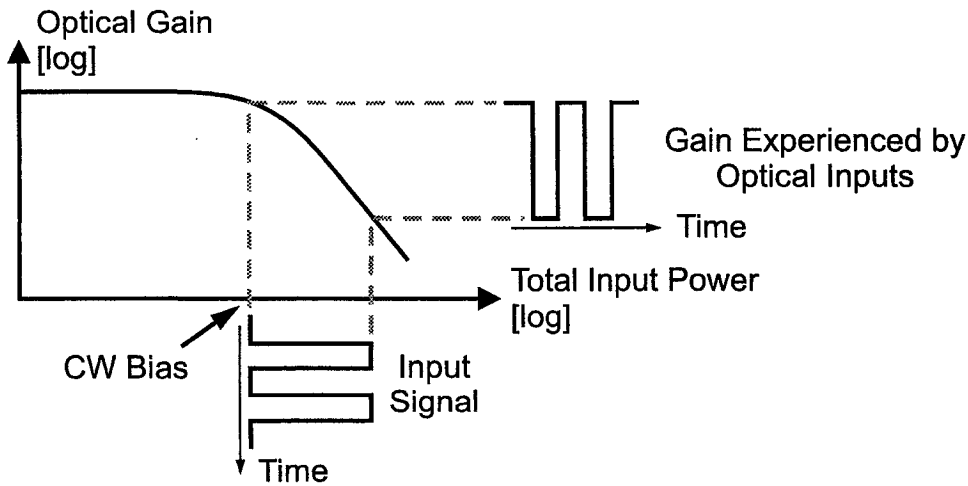

Figure 2-4 Schematic of XGM in an SOA. An amplitude modulated input signal modulates the gain of the SOA and thus the output power of a second, CW input. Adapted from [WILL95].

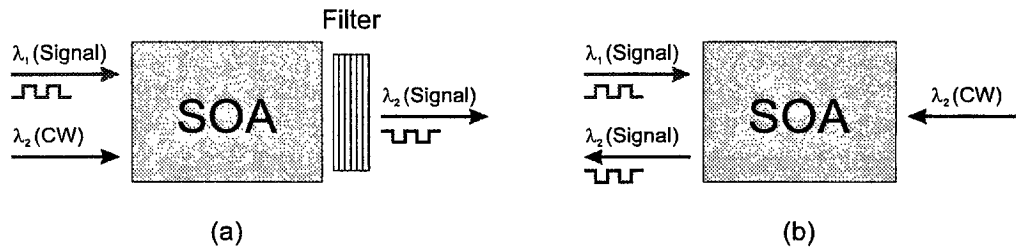

Figure 2-5 Schematic of the a) co-propagation and b) counter-propagation XGM schemes.

that can be cascaded, while maintaining an acceptable signal to noise ratio. Another problem is that the large change in carrier density imparts considerable chirp on the converted signal [DUUR96]. Chirp is undesirable when the output signal is to be sent down a long length of fiber, because the signal will suffer from dispersion. However if the signal is to be used locally, for instance for further logical processing, this may not be as serious an issue. Finally, the converted signal is inverted with respect to the input signal. This may be undesirable in some circumstances, although it can be remedied by using a second XGM device.

2.4.2 Cross Phase Modulation (XPM)

This technique makes use of the change in refractive index associated with a change in carrier density within an SOA. The change in carrier density may be produced by a change in the injection current, or in the case of all-optical switching, through gain saturation. The relationship between carrier density and refractive index is given by

$$\Delta\eta = \frac{-a\left(N - N_0\right)\alpha_N}{2\,k_0}, \tag{2.3}$$

where a is the differential gain, N is the carrier density, N_0 is the carrier density at transparency, α_N is the linewidth enhancement factor, and k_0 is the wavenumber in free space. The linewidth enhancement factor describes the relationship

between the refractive index and the gain of the SOA, each as a function of carrier density. Its name comes from its effect of spectral broadening of the lasing wavelength in semiconductor lasers [CONN02 pg. 130]. An excellent overview of the linewidth enhancement factor is given by [OSIN87]. The value of α_N depends on the material and the device structure. Tables are given for various estimates of α_N at 1.55 μm (InP/InGaAsP), with most values being close to 6. Mathematically, it is often written as,

$$\alpha_N = -2\,k_0 \frac{\partial\eta/\partial N}{\partial g/\partial N}, \tag{2.4}$$

where g is the gain per length. Substituting (2.4) into (2.3) and noting that $\partial g/\partial N = a$, we obtain

$$\Delta\eta = (N - N_0)\frac{\partial\eta}{\partial N}. \tag{2.5}$$

The phase change of light travelling through the SOA, associated with a change in carrier density is [ASGH97]

$$\Delta\phi = \frac{2\pi L\Gamma\Delta\eta}{\lambda_{CW}} = \frac{2\pi L\Gamma(N - N_0)}{\lambda_{CW}}\frac{d\eta}{dN}, \tag{2.6}$$

where L is the length of the SOA, Γ is the waveguide confinement factor, and λ_{CW} is the wavelength of the light on which the phase shift is being measured. The confinement factor represents the fraction of the optical mode energy confined within the active region and its value depends on the device structure [SALE91 pg. 621, AGRA86 pg. 30].

An interferometer is used to convert the optical phase modulation into intensity modulation. Early designs relied on Michelson interferometers (MI) [MIKK94] and asymmetric Mach-Zehnder interferometers (MZI) [DURH94], [RATO95] as shown in Figure 2-6. These structures are typically integrated onto a chip, represented by the gray shaded area in the figure. In the MI, the right

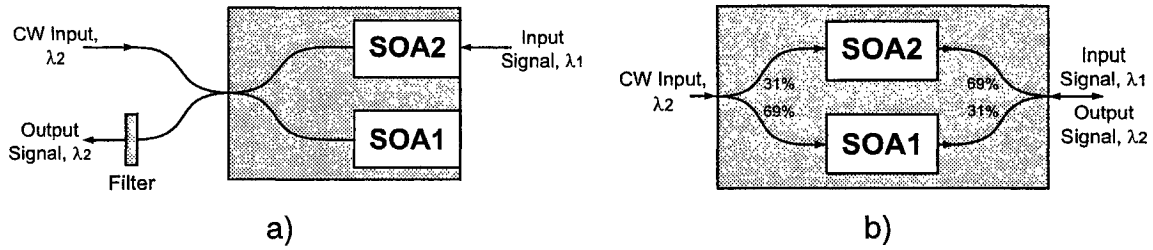

Figure 2-6 a) A Michelson interferometer, and b) an asymmetric Mach-Zehnder interferometer for converting phase modulation to amplitude modulation.

hand side of the chip is uncoated, providing the necessary reflection for the CW input. The input signal modulates the gain and refractive index of SOA2, producing a phase shift in the CW input light in the upper arm of the interferometer. The MZI uses asymmetric couplers/splitters so that the input signal produces a larger phase shift in the upper arm than the lower arm.

The MZI was later improved through the use of additional waveguides as shown in Figure 2-7. This design uses symmetric coupler/splitters and provides separate ports for the input signal and converted output signal, ensuring that only one of the SOAs is modulated, thus improving performance. The optical power exiting the interferometer is calculated using

$$P_{total} = \frac{1}{2}\left(P_{upper} + P_{lower} + 2\sqrt{P_{upper} \cdot P_{lower}} \cos\Delta\theta\right), \tag{2.7}$$

where P_{upper} and P_{lower} are the optical powers in upper and lower arms, respectively, of the interferometer immediately before the waveguide coupler. $\Delta\theta$ represents the phase difference between the two modes at the output-branch of the waveguide interferometer where the two modes interfere. This equation is derived in Section 4.1 and further details can be found in [NISH85].

Generally an SOA is placed in each arm of the MZI, even if only one of the SOAs is to be modulated [DURH96]. This allows the output powers of the two SOAs to be comparable, which is necessary for a good extinction of the output

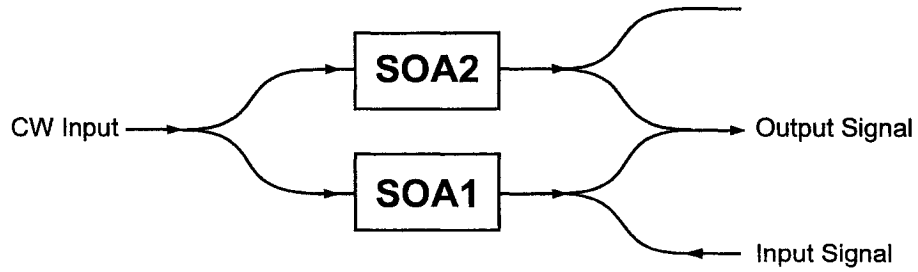

Figure 2-7 Schematic of a Mach-Zehnder interferometer with a semiconductor optical amplifier in each arm. The entire structure is produced on an optical chip.

signal upon destructive interference. The first experimental results for a device similar to the one shown in Figure 2-7 were published in 1994 [SCHI94]. The whole chip was 0.75 mm wide and 3 mm long and produced an output extinction ratio of 26 dB for an input extinction ratio of 8 dB.

The currents supplied to the SOAs in each arm can be controlled independently, resulting in a controllable phase difference between the upper and lower arms of the MZI, for a given input signal power. Added flexibility is achieved by adding a separate phase shifting section in one of the arms [RATO97]. The phase difference can also be controlled in the design stage by using asymmetric arm lengths. Using these techniques, the MZI-SOA can be designed to produce destructive interference at the output waveguide coupler for any value of input signal power. This flexibility allows the device to be used in either an inverting or a noninverting mode, offering a significant advantage over cross-gain modulation. Examples of inverting and noninverting transfer functions are shown in later chapters (e.g. Figure 4-8).

Slow carrier lifetimes, or relaxation times, on the order of hundreds of picoseconds [CONN02], have long been known to be a problem in SOAs, limiting the speed at which they can operate. All of the very high speed experiments have overcome this problem by using what has variously been called differential, push-pull, or delayed interference XPM. It was first proposed for use with

MZI-SOAs in 1993 where it was called a symmetric Mach-Zehnder switch [TAJI93]. Subsequent experimental verification produced 8 ps FWHM output pulses from the MZI, the width of which was limited by the measurement equipment [NAKA94]. Apparently unaware of these first reports, the technique was reported again three years later [MIKK97].

This differential XPM works by sending an input pulse into one arm of the MZI, and a second, delayed and attenuated pulse, into the other arm of the interferometer as shown in Figure 2-8. The MZI is designed such that the CW input experiences destructive interference at the output of the interferometer with no input signal. For simplicity, it will be assumed in this explanation that this is accomplished with asymmetric interferometer arm lengths, so that the SOAs can be considered to be symmetric in their design and operating conditions. The first input pulse arrives at SOA2 and changes its refractive index of such that the CW signal experiences constructive interference at the output of the interferometer. After the peak of this input pulse has passed through SOA2, the carrier density begins to recover, limited by the relaxation time. The second input pulse arrives

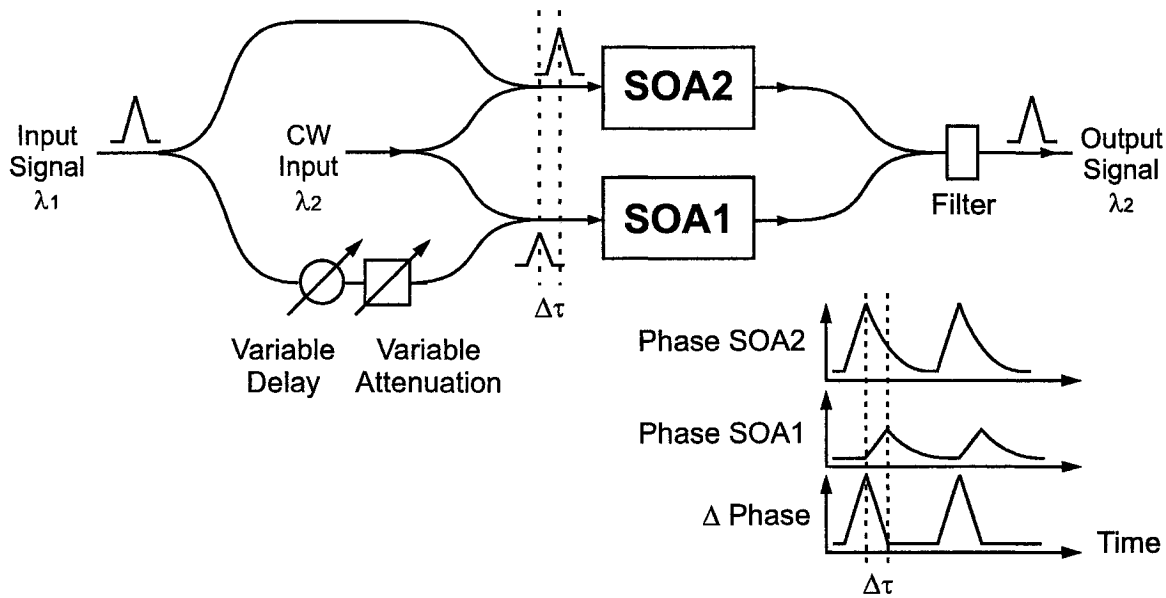

Figure 2-8 Schematic showing differential cross-phase modulation. Redrawn from [MIKK97, STUB00].

at SOA1 with a delay of $\Delta\tau$ and changes its refractive index. The goal is to have the peak phase change imparted on the CW input by SOA1 equal to the recovering phase change imparted on the CW input by SOA2. The CW input again experiences destructive interference at the interferometer output, completing the formation of the output pulse. The carrier densities of both SOA1 and SOA2 continue to recover, in a similar enough manner that destructive interference of the CW input is maintained. In this way very short pulses can be processed, leading to high bit rate operation. However, the repetition rate remains limited by the carrier lifetime as the SOAs return to their initial states. Still, high speed data could be demultiplexed and processed in parallel, if necessary.

2.4.3 Four Wave Mixing (FWM)

Four wave mixing in SOAs has been much investigated for use in wavelength conversion [VAND00a]. It is a coherent process by which two optical fields form a dynamic gain and refractive index grating in the SOA [AGRA88]. One of the fields is a pump and the other is a signal (probe). The dynamic grating frequency is at the frequency detuning, or the beat frequency, of the two fields. The pump is diffracted by the grating producing a new, conjugate field [AGRA88], [USKO94]. This process is shown schematically in Figure 2-9. At low input frequency detunings, modulation of the carrier density is primarily responsible for the creation of the gratings. At higher detunings, spectral hole burning and

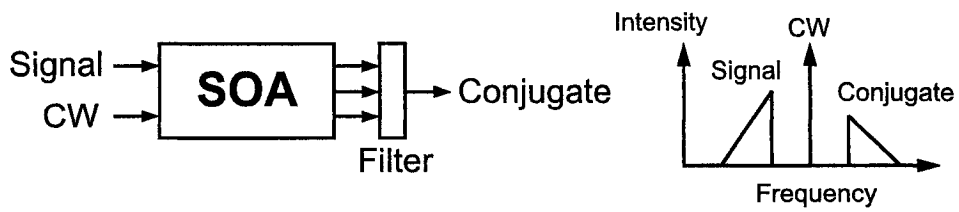

Figure 2-9 Schematic showing the operation of FWM in an SOA.

carrier heating, both valence intraband effects, dominate. These are much faster physical processes, with response times on the order of hundreds of femtoseconds, allowing FWM to operate at high speeds [USKO94]. Unfortunately, they are also weak, limiting the efficiency of FWM [DURH96].

One requirement for efficient FWM is that the polarization of the input fields must be the same [CONN02]. As the input polarization of the signal may not be known, many schemes have been proposed to provide polarization insensitivity [LACE98], the most basic of which is shown in Figure 2-10 [LACE97].

In comparing FWM to XPM, the former has the advantage of being able to convert multiple wavelengths simultaneously [STUB00]. A disadvantage of FWM is that the output wavelengths are different than the input wavelengths. The FWM process was touted as superior to cross-phase modulation because of the high speed, but the development of differential XPM and the ultrafast nonlinear interferometer (UNI, discussed in the following chapter) have changed things somewhat. Differential XPM is far easier to implement and operates at speeds that should be sufficient for the development of next generation optical routers. The UNI operates at speeds similar to FWM and is more efficient.

There has been little application of FWM to higher functionality devices such as logic gates. There are a couple of exceptions, but these tend to be complex [NESS94, MORI96, VAHA97]. Thus, FWM will not be considered in the remainder of this thesis.

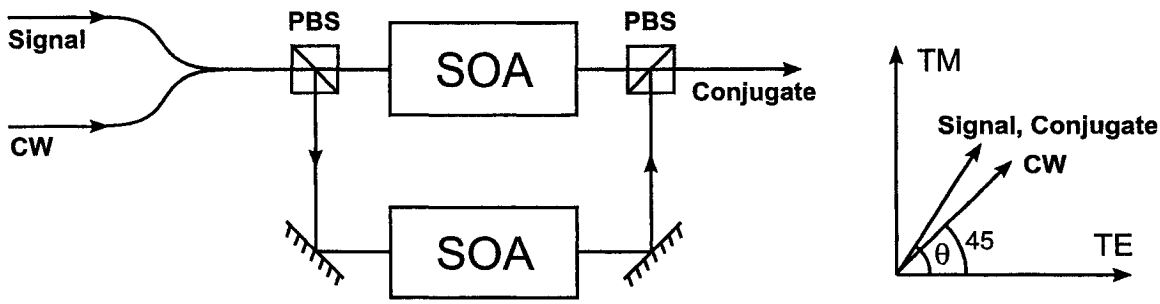

Figure 2-10 Polarization insensitive FWM, using polarizing beam splitters (PBS). Redrawn from [LACE97].

CHAPTER

3

DIGITAL OPTICAL SIGNAL PROCESSING

Long-haul fiber communications systems transmit large amounts of data at multiple wavelengths. There has been much effort in creating a network that can process this data optically rather than electronically. Considerable attention has been paid to the semiconductor optical amplifier (SOA) as a nonlinear device capable of performing several digital optical signal processing functions [STUB00]. In this chapter, various devices for performing these functions will be described including wavelength converters, demultiplexers, regenerators, logic gates, and memories. Particular attention will be paid to the role of cross-phase modulation in these devices. Alternative technologies for optical memory will then be discussed. Finally, brief consideration will be given to the overall communications network, to gain a better understanding of where digital optical signal processing would be used.

3.1 INTRODUCTION

As discussed in the previous chapter, the widespread use of the optical amplifier led to a revolution in optical communications, allowing wavelength division multiplexing to be widely employed. However, we are still faced with large

amounts of electronics within communications systems. Designers would like to make new systems that are more optically transparent in the sense that data can remain in optical form through more of the system, without optoelectronic conversions. Much literature exists on this broad topic; a nice introduction is given in [MIDW93], which includes a chapter on the role of SOAs.

There has been progress in the pursuit of an all-optical network. Micro-mechanical switches are used to switch the entire optical content of one fiber onto a choice of other fibers [YASE99, HOFF99]. However, these switches are relatively slow and are most useful only to reconfigure a network when a particular fiber route becomes damaged or otherwise unusable.

Wavelength converters go a step further than micromechanical switches. If data from two fibers is being merged onto a single fiber, there may be channel conflicts, where two channels of the same carrier wavelength need to be switched onto a single output fiber. A wavelength converter, as its name implies, takes one optical channel and translates its optical carrier wavelength to a new, unused wavelength. Thus channel switching is achieved. At higher modulation speeds, the wavelength converter can also be used as a multiplexer/demultiplexer for packets or even individual bits [WOLF00].

For higher levels of processing, optical logic and memory are required. These could be used in conjunction with a wavelength converter, for instance, to determine what wavelength is free to be used for channel switching. More ambitious plans would involve processing packet header information [BARE02, BARE03, BLUM00, DANI98, HUNT98, CLAV04]. In this way a packet switch could be created. This topic will be considered in more detail at the end of this chapter.

At each stage described above: fiber switching, channel switching, and packet switching, the network becomes more flexible and allows increased throughput.

Regeneration is also currently the realm of electronics, but is being investigated in the optical domain [NUTT03]. Popularly classified as either 2R or 3R regenerators, 2R regenerators provide reamplification and reshaping of incoming pulses, and 3R regenerators also provide retiming. Reshaping of an optical pulse improves the signal-to-noise ratio of the data stream. The retiming of a pulse attempts to remove any pulse jitter accumulated in the remainder of the system.

3.2 FUNCTIONAL DEVICES

3.2.1 Wavelength Converters

Of the devices described in this section, perhaps the one that has received the most attention recently, at least with regard to SOAs, has been the wavelength converter [VAND01]. As has already been shown, the principles of XGM, XPM, and FWM can be exploited for the purpose of all-optical wavelength conversion. MZI-SOAs have been used to perform wavelength conversion at up to 40Gb/s [JOER97, WOLF00].

3.2.2 Demultiplexers

For very high bit rate optical time-division multiplexed (OTDM) systems, demultiplexers and add/drop multiplexers are critical for extracting a particular channel. This is accomplished by replacing the CW input of Figure 2-7 with a pulsed input, designated the Demux Control in Figure 3-1. One Demux Control pulse is required for every bit that is to be extracted from the OTDM signal. The setup then functions as an AND gate. If there is no OTDM signal, a Demux Control pulse will experience destructive interference at the interferometer output, because the interferometer is noninverting, and no output pulse will be

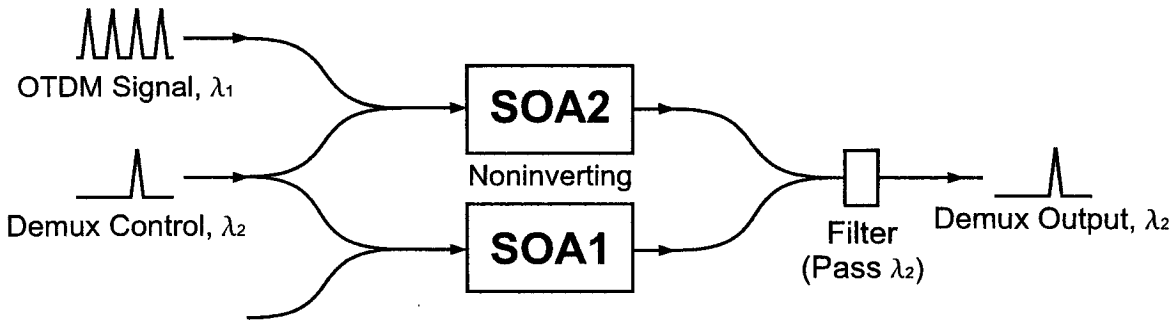

Figure 3-1 Example of demultiplexing of an OTDM signal using regular co-propagating XPM.

observed. If an OTDM pulse is present, the Demux Control pulse will experience constructive interference, and a pulse will be observed at the interferometer output and will pass through the filter. An OTDM demultiplexer has been reported at 40 Gb/s [WOLF00] using differential XPM. A full add/drop multiplexer has also been reported at the same speed, using the same technique [FISC00].

3.2.3 Signal Regenerators

Another application which has received some attention is the optical regenerator [NUTT03]. While the erbium-doped fiber amplifier [SALE91] and the Raman amplifier [ISLA02] perform very well as simple linear amplifiers they cannot be used to reshape a digital signal. The purpose is to remove noise and sharpen the edges of a rounded pulse, leading to fewer bit errors at the receiver. This application is suited to long-haul network links, where the reshaping may be performed, as required, in mid-link. Currently this process is performed electronically. Some regenerators also provide signal retiming [LAVI98] to reduce the effects of jitter, and research has been carried out on the development of optical retimers, but it will not be discussed here.

Due to its poor conversion efficiency or extinction ratio degradation [SPIE98], XGM is not suited for regeneration applications. On the other hand, XPM performs well and experimental operation at 40 Gbit/s is reported [WOLF00].

3.2.4 Logic Gates

Optical logic gates are basic building blocks that would find widespread use in all-optical switches. A good review is given in [STUB00]. While a few logical operations can be accomplished using XGM, the low conversion efficiency limits the number of gates that could be connected together [WANG00, ZHEN00]. Also, to the author's knowledge, the XOR operation has not been demonstrated with XGM. This function is a particularly important function for use in parity checking and data encryption [FJEL00a].

All of the basic logic gates have been demonstrated using MZI-SOAs including NOT, AND, OR, and XOR. These gate designs have also been patented [ROBE99]. Experimental verification includes an XNOR at 10 Gbit/s [LEE02], the OR at 10 Gbit/s [FJEL00b], the XOR at 20 Gbit/s [FJEL00a], and the AND at 20 Gbit/s [KANG00].

During the course of this thesis, logic gates that process wavelength encoded digital data were designed [VAND00b]. One set of gates relied on XPM, while a second set relied on FWM. However, it was felt that these were too complex to be practical and will not be discussed further.

3.2.5 Memory

Functional devices that exhibit memory are of primary interest in this thesis. Optical memory elements can conveniently be divided into two groups: single bit memories and buffer-type memories. An example of a single bit memory is a flip-flop. With this type of memory, it is possible to read the bit at any time. If multiple bits are to be stored, multiple memory elements are required. In contrast, buffer-type memories are used to store many bits of data, perhaps in the form of a packet. These bits circulate in a loop and can be read once each time the data circulates around the loop.

In electronics the flip-flop is the most basic memory element [HORO89]. Several variations exist, depending on the application. The simplest is the SR or set-reset flip-flop shown in Figure 3-2. In this type of flip-flop, the output responds immediately to a change in the input signals. As drawn, the flip-flop remains in its memory state when both inputs are low. When one of the inputs goes high, the flip-flop is set or reset as appropriate. When both inputs are high, the output is indeterminate and may oscillate. If necessary, this state can be avoided by conditioning the input signals with an additional stage of logic.

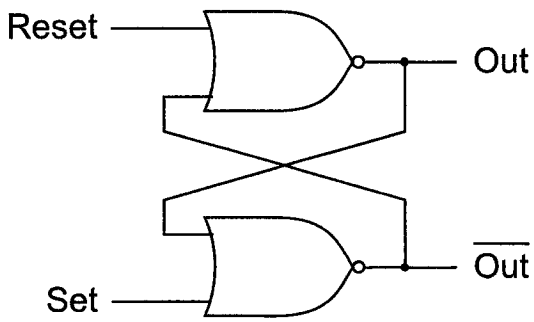

Set	Reset	Out_{t+1}
0	0	Out_t
0	1	0
1	0	1
1	1	Indeterminate

Figure 3-2 A electronic set-reset type flip-flop and its truth table.

In some systems it may be desirable to have a clocked flip-flop. This is easily achieved by inserting an AND gate before each of the inputs to the flip-flop. Thus the set and reset signals are ANDed with the clock signal and the inputs only progress to the flip-flop when the clock is high. When the clock is low, the flip-flop remains in the memory state. A problem with this circuit is that the output of the flip-flop will not be synchronized to the clock signal. This is because the set or reset signals may change the output of the latch halfway through a clock pulse. To solve this problem, a type of double stage clocked flip-flop is used. This is more commonly known as master-slave or D type flip-flop. Only one input is used and the output of the flip-flop is updated only at the falling edge of the clock signal. By allowing the output to change only at one point in the clock signal, the output is then synchronized.

Flip-flops have many purposes and can be used in many ways. They are used in counters, arithmetic accumulators, and shift registers among other things. Clocked flip-flops can be combined with logic gates, resulting in a simple yet powerful system known as a sequential circuit or synchronous system [HORO89]. This scheme, shown in Figure 3-3, forms the basis for many electronic systems. In the case of a telecommunication system, the circuit may generate its clock signal from the incoming data so that the two are synchronized.

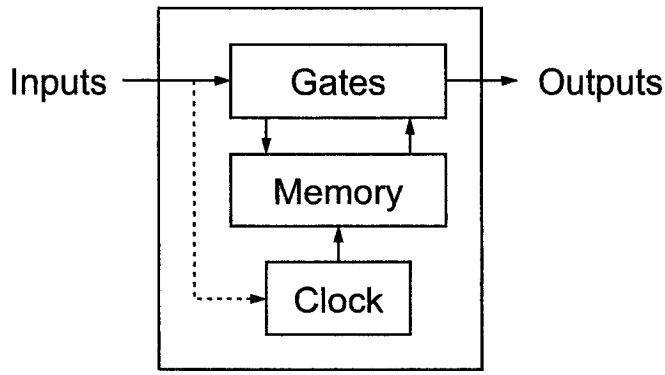

Figure 3-3 Block diagram of a sequential circuit. The dotted line represents a clock signal that is derived from the incoming data signal.

Both single-bit flip-flop type and buffer type memories can be constructed using XPM in SOA-based MZIs. In principle, a flip-flop could be built exactly as shown in Figure 3-2, but using optical NOR gates. However, it would be advantageous to reduce the hardware. The only work in this area to date has been a single patent for a flip-flop type memory [ROBE99b], and a system-level design incorporating a seemingly identical patent-pending flip-flop [CLAV04]. As will be shown in upcoming chapters, it is possible for the design to enter an undesirable oscillating state. One of the main contributions of this thesis is to propose an alternative design for a flip-flop type memory that overcomes this

problem [VAND02, VAND03]. A second contribution is a proposed modification to the flip-flop design that allows it to be used as a buffer type memory.

3.3 COMPETING TECHNOLOGY

Several techniques are described below as alternatives to the memory developed in this thesis. Bistable laser diodes are suitable for flip-flop-type memories, while TOADs and UNIs are suitable for buffer-type memories.

3.3.1 Bistable Laser Diode Memory

Considerable work has been carried out in the area of bistable laser diodes for use as optical memory elements [KAWA94, KAWA97, VAND99, WANG97]. These devices, exhibiting hysteresis, are suitable for flip-flop-type memories. Unfortunately, many of these systems suffer problems that would limit their usefulness in practical systems. For instance, in many cases the device is set optically but must be reset electrically. Even with an optical reset, it may need to be of a different wavelength or power level compared to the set [ODAG89]. The devices tend to be very sensitive to the power levels and/or wavelength of the input signals. In many devices the characteristic of the output light that is bistable may be the polarization [KAWA98] or the wavelength, making it difficult to incorporate into existing communications systems. Many bistable systems require an inverted or so-called dark reset pulse. This too is undesirable.

Ideally the device should allow identical set and reset pulses, with respect to power, wavelength, and polarization. The device should also be insensitive to variations in those characteristics.

There are a few cases that avoid most of the problems described above. Perhaps the first experiment reporting bistable switching with identical set and reset pulses used a two-segment multi-quantum-well distributed-feedback laser

diode [ZHOU97]. The two segments of the laser diode cavity were operated as a saturable absorber and a gain medium, respectively. The optical loss of the absorber segment prevented the gain segment from reaching lasing threshold. A set pulse injected into the saturable absorber made it transparent, initiating laser action. A reset pulse then stopped the laser action through gain quenching. The maximum repetition frequency of the flip-flop was limited to hundreds of megahertz, due to a slow carrier recovery time.

A recently developed flip-flop uses a nonlinear directionally coupled waveguide as a means of resetting a typical bistable laser diode [TAKE04]. This flip-flop also includes a saturable absorber at one end and is set in the same way as the previously described device. The nonlinear directionally coupled waveguide parallel to the laser cavity, and a reset pulse injected into it, are then used to stop laser action by extracting light from the laser cavity. The saturable absorber again becomes opaque, resetting the flip-flop. Experimental verification at 2 GHz with a 10 dB extinction ratio were described.

3.3.2 Terahetz Optical Asymmetric Demultiplexer (TOAD) Memory

Nonlinear Sagnac interferometers have received a great deal of attention as functional devices. Early devices used fiber as the source of the nonlinearity; however, as the nonlinearity of fiber is weak, a very long length was required. An SOA was used as the nonlinear element in later variations, allowing a much more compact design. These designs are referred to as semiconductor laser amplifier in a loop mirrors (SLALOMs) [EISE92, EISE95] and terahertz optical asymmetric demultiplexers (TOADs) [SOKO93]. As the differences between these devices are trivial, they will be considered below as a single device and referred to as the TOAD. The basic design of the TOAD is shown in Figure 3-4. The optical data signal is injected into port 1 of a 50:50 coupler.

The operation of the TOAD is as follows. The coupler produces a lower power pulse at both port 3 and port 4, one travelling clockwise around the loop,

and the other travelling counterclockwise. The pulses are assumed to be low enough in power that they do not elicit a nonlinear response from the SOA. Two cases are possible; first consider the case of no control pulse. The clockwise pulse arrives at the SOA and a short time later the counterclockwise pulse arrives. As they are low power, the SOA remains in the linear regime and the two pulses experience the same gain and phase delay. When they return to the coupler they have equal powers and phases. They combine to produce an output at port 1 with no signal at port 2. In the second case, a control pulse is used and is timed to arrive at the SOA after the clockwise pulse, but before the counterclockwise pulse. The control pulse has a sufficiently high power that it quickly saturates the gain of the SOA. The gain recovery of the SOA is relatively slow compared to the gain saturation so the counterclockwise pulse experiences a lower gain than the clockwise pulse and thus also a phase delay. When the clockwise and counterclockwise pulses return to the coupler the difference in power and phase lead to a pulse being observed at port 2.

Though not mentioned in the early papers, the control pulse will create pulses at both port 1 and port 2. Thus the control pulse and data should be set to different wavelengths, and the output requires a filter to separate the data from

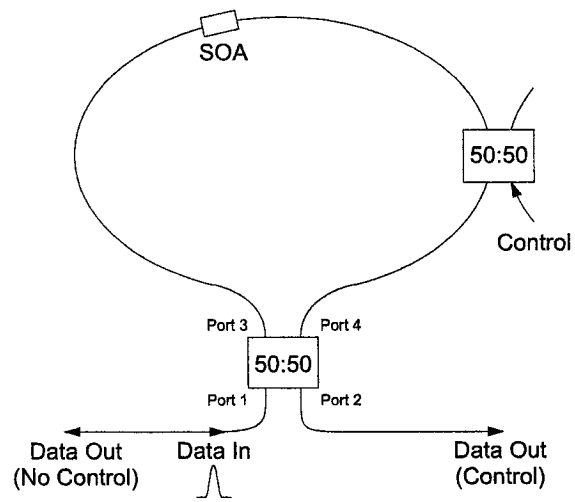

Figure 3-4 Schematic of a terahertz optical asymmetric demultiplexer.

the control signal. This additional consideration is alluded to by Poustie *et al.* [POUS97, POUS98a]. For simplicity, these filters are not shown in the schematic.

A buffer type memory was demonstrated using two TOADs with feedback [POUS97], and later the device was improved to provide full read and write capability [POUS98a] through the use of a third TOAD and a circulator. A schematic of the more complex memory is shown in Figure 3-5. The operation is as follows. The pulse stream at the input of TOAD1 is normally reflected back out the same port. When a data signal arrives, pulses are instead directed to the output port of TOAD1. TOAD2 simply acts as a wavelength converter so that the circulating memory bits can be used as a control signal for TOAD1. The data is read from the memory each time it circulates, through the use of a tap. Without the circulator and TOAD3, that constitutes a simple memory element. To read selected bits only, Poustie *et al.* propose using the circulator and the third TOAD. With no extract signal, TOAD3 reflects the memory bits back into the memory loop. When an extract pulse is applied, the memory bit is removed from the loop and appears at the output of TOAD3.

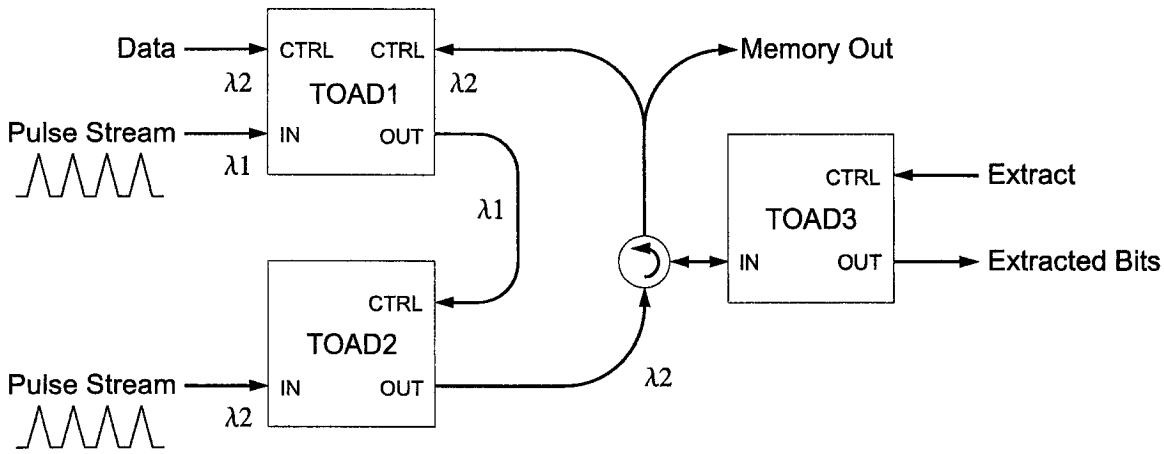

Figure 3-5 Schematic of a buffer-type memory with read and write capability, based on TOADs. Adapted from [POUS98a].

The memory was experimentally demonstrated at a bit rate of 1 Gb/s and an output extinction ratio of 15 dB. It should be noted that because this TOAD-based memory works with a pulsed input, it can be used for buffer-type memories that can be read once per loop delay as the data circulates around the loop; however, it cannot be used for single bit memories that can be read at any time. Another downside of this design is that the amount of necessary hardware is quite high when the generation of the two pulse streams is included.

Another buffer memory based on a TOAD-like arrangement was proposed by [HONG99] and is shown in Figure 3-6. It is far less hardware intensive than the design shown in Figure 3-5; however, to the author's knowledge, it has not been experimentally verified. The operation is straightforward, the upper loop acting as a TOAD, and the bottom loop providing feedback.

In addition to the memory described in detail above, TOADs have been used to build more complex optical systems. A series of papers reports experimental

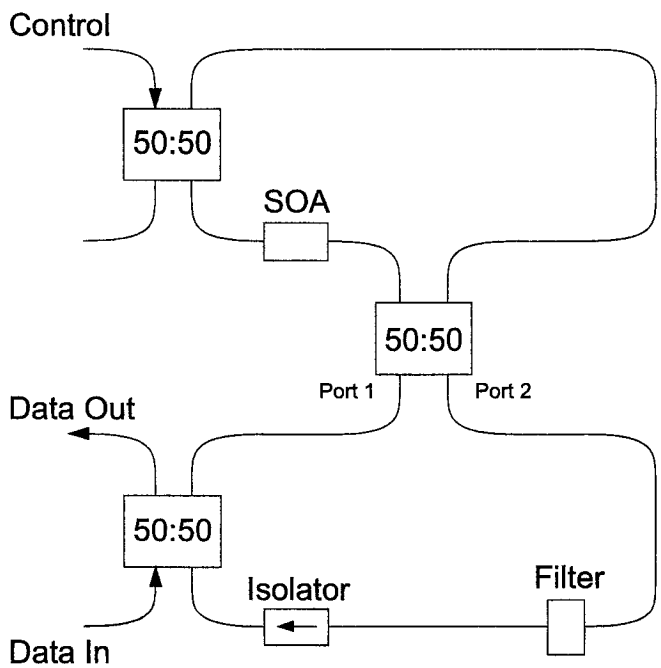

Figure 3-6 A second buffer type memory based on a Sagnac interferometer. Adapted from [HONG99].

verification of all-optical counters [POUS00], all-optical half-adders [POUS98b], and all-optical shift registers [POUS96].

These TOADs have been widely reported in the literature. Nonetheless they do have at least two limitations. The first is that they are bit-rate dependent [JOER97]. If a TOAD is designed for a high bit rate and operated at a low bit-rate, the position of the SOA in the loop must be modified, and the length of the loop might have to be increased. Secondly, TOADs can only handle return-to-zero (RZ) signals [STUB00].

3.3.3 Ultrafast Nonlinear Interferometer (UNI) Memory

Another method of performing logical operations with an SOA is through the use of an ultrafast nonlinear interferometer (UNI) [MANN99], shown in Figure 3-7. In this device, a single input pulse is sent through a few meters of polarization maintaining (PM) fiber at 45 degrees relative to the fast and slow axes of the fiber. The birefringence of the PM fiber creates two orthogonally polarized pulses separated in time. The two pulses pass through a polarization insensitive SOA and an equal length of PM fiber with the fast and slow axes reversed, such that the two pulses overlap in time again. The recombined pulse then passes through a polarizer set at 45 degrees to the axes of the fiber.

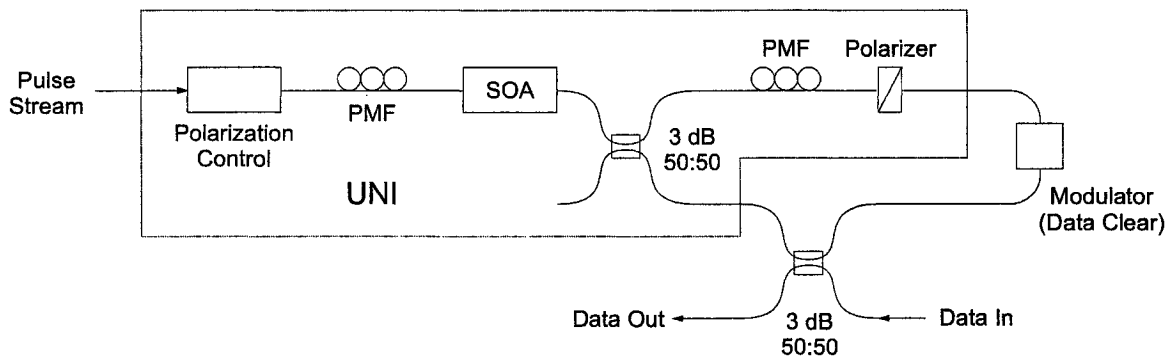

Figure 3-7 Schematic diagram of a buffer-type memory based on an ultrafast nonlinear interferometer (UNI). From [MANN99].

When an intense control pulse arrives at the SOA between the two data pulses, it imparts an additional π phase shift on the second data pulse via gain saturation in the SOA, which is associated with a refractive index change. After passing through the second length of PM fiber the pulses recombine, but with a polarization that is now orthogonal to the polarizer and thus the light is blocked. Manning *et al.* then applied feedback to the UNI so that the output data became the control pulses for the next pass of the memory loop.

Unfortunately, the UNI as described is inverting, thus the data in the memory loop will be inverted with each pass and will only be correct at the output on every second pass. Data is input and output from the memory loop via a 50:50 coupler and is cleared using a modulator placed inside the loop. The feedback loop also used two EDFAs to provide gain and a filter to remove noise. For simplicity none of these are shown in the diagram. Although not mentioned, it seems likely that an isolator would also be necessary to prevent light from travelling counterclockwise around the loop. The whole setup was shown to operate at a bit-rate of 10 Gb/s with an extinction ratio of 20 dB.

While the results of this experiment are good, the setup as described in the paper used an acousto-optic modulator in the feedback loop. Thus optical clearing of data was not demonstrated. For all-optical operation, a second UNI would be required to replace the acousto-optic modulator.

3.3.4 Other Optical Memory

Another recent optical memory uses coupled Mach-Zehnder interferometers as the basis for a flip-flop [HILL01]. Two MZIs, each with an SOA in one arm only, are configured as shown in Figure 3-8. Each MZI is designed to operate with an inverting transfer function. In this way, a high output from one of the MZIs suppresses the output of the other MZI. A pulse injected into the first MZI causes

its output power to drop, allowing the output power of the second MZI to increase. The high output from the second MZI then maintains the low output power state of the first MZI. Expected operating parameters such as maximum bit rate and extinction ratio are not given and the experimental data demonstrates the device operating at only 10 Hz. Nonetheless, the flip-flop does not seem to suffer from any obvious problems and operation to a few gigabits per second should be possible. For higher speed operation, the authors suggest a similar flip-flop based on differentially operated MZIs with SOAs in each arm. While that device is more complex than the flip-flop discussed here, the basic operating principles are the same.

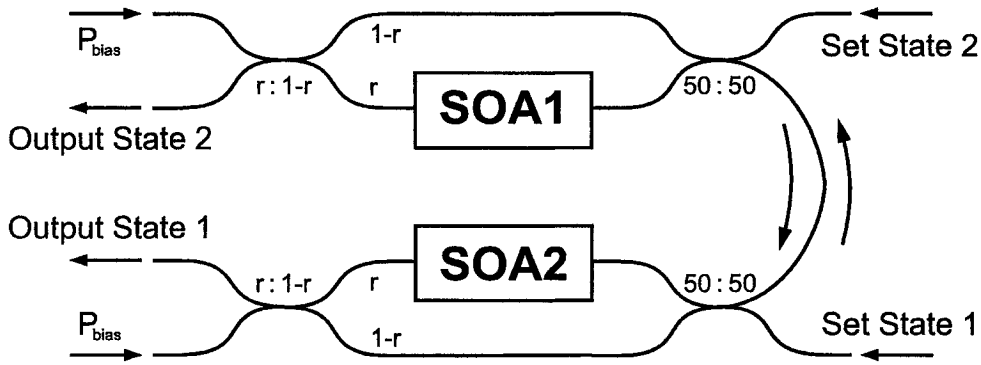

Figure 3-8 A flip-flop based on coupled Mach-Zehnder interferometers [HILL01]. The variable, r, is used to represent an asymmetric splitter.

3.4 OPTICAL PACKET SWITCHING

It is useful to have insight into how, why, and where optical memory might be used in an optical communications system. At the beginning of this chapter, the progression from a fiber switched network to a channel or wavelength switched to a packet switched network was introduced. This section briefly considers some of the issues related to an optical packet switched network, including

packet labeling, methods of routing, and packet switching. A good overview of the issues is given by [JOUR01]. In that paper, it is stated that the two main hurdles still to be overcome are a 'lack of deep and fast optical memories' and the 'poor level of integration' available today.

All-optical label swapping is a proposed method of forwarding and routing discrete packets in the optical layer of a communications network [BLUM00]. The goal is to route packets without regard to the packet length or bit-rate. The general idea is to encapsulate the IP (internet protocol) packet using an optical label that is suitably designed to work with the processing hardware. At each router the label is separated from the payload of the packet and processed. The appropriate switching action is taken and a new label is attached to the payload as it exits the router. First generation optical packet switched networks may process the label electronically while the payload is sent through an optical buffer. Later generations may process the labels optically.

Several packet labeling schemes have been proposed [BLUM00]. The label may be serial, appearing at the beginning of the optical packet and separated from the payload by a temporal guard band so that it can easily be isolated from the rest of the packet. Another scheme is to use the label data to modulate a sub-carrier before being added to the packet data. In this way the label exists at the same time as the payload but at a slightly offset frequency, although it modulates the same optical carrier as the payload. The label is then isolated from the payload using a narrowband filter such as a fiber Fabry-Perot filter.

It is generally accepted that the optical label should be designed such that it uses a lower bit-rate and perhaps a different modulation format than the payload [BLUM00, HUNT98]. This simplifies the design of the processing circuitry and provides transparency to the system. This is beneficial for both electrical and any proposed optical processing schemes.

A particularly interesting concept is that of Cartesian routing, which could employ either serial or sub-carrier modulated labeling. In this system, the desire

is to eliminate lookup tables in the router. These tables constitute the bulk of the label processing and are costly in terms of both processing time and the amount of memory required. In the Cartesian system arbitrary IP addresses are replaced with a coordinate based address which could be composed of latitude and longitude or some similar scheme. In this way a simple comparison between the destination address of the packet and the address of the router is required. Again, because of encapsulation, such a network is completely transparent to the packets travelling through it. An all-optical processing scheme based on Cartesian routing has recently been proposed, taking advantage of the simplified label processing [BARE02, BARE03].

After processing the packet label, the next task of a router is to forward or switch the packet to the correct output port. The primary concern of any switch is to adequately handle packet contention, that is, if packets from two input ports are destined for the same output port, one must be delayed in time so that they do not interfere [HUNT98]. The process of delaying certain packets is called buffering or queuing. Optical buffering is advantageous as it removes the need for conversion between the optical and electronic domains [MASE93]. While it has been said that "for most practical purposes, there is no such thing as optical memory in a form that might serve as a FIFO (first in, first out) buffer" [MIDW93 pg. 10], progress continues and the buffer memory proposed in this thesis is one option.

Interestingly, wavelength conversion has been shown to be very important in improving the performance of optical packet switches [DANI98]. One of the leading contenders for wavelength conversion is cross-phase modulation in MZI-SOAs. If these devices are produced in large numbers for this purpose, the economy of scale suggests that the price will become low for MZI-SOAs making them economically attractive for use as memory elements.

CHAPTER

4

NUMERICAL SIMULATIONS

Simulations of various devices, including logic gates and flip-flops, were performed by modeling the semiconductor optical amplifiers (SOAs) with coupled differential equations. These equations include a travelling wave equation and a carrier rate equation. Numerical solutions to the equations were used to investigate both static and dynamic behaviors of the devices. This chapter begins by presenting the model and simulating the basic behavior of a single SOA. The model of the whole interferometer is then constructed. Detailed static and dynamic simulations are performed on three potential flip-flop designs. One of the flip-flops, which was patented [ROBE99b], is shown to be sensitive to reset pulse duration and can experience undesirable oscillations when reset. A second flip-flop design is considered but is shown to suffer from critical slowing-down. The topic of critical slowing down is investigated through a simple linear analysis of the interferometer transfer function. A third flip-flop design is then proposed that avoids the problems associated with the first two. This new flip-flop design is one of the major contributions of this thesis. Its sensitivity to various input parameters is investigated. Results suggest the flip-flop is tolerant to changes in input pulse wavelength and power. Finally, an optical ring oscillator is simulated and its stability is investigated in detail.

4.1 THE MODEL

A schematic representation of the device that was modeled is shown in Figure 4-1. The variables are explained later in this section. Several variations of the design were also considered, and will also be discussed later. The SOAs are integrated into a Mach-Zehnder interferometer (MZI) and make use of counter-propagating cross-phase modulation (XPM). It is assumed that there is independent control of the initial gain and phase of each arm of the interferometer. This can be achieved through the use of an electrically tuned phase shift element in the unmodulated arm [RATO97] or by changing the length of the arms during the design stage. The schematic is simplified, as it is generally necessary to include filters and isolators into the design. The filters remove much of the spontaneous emission and amplified spontaneous emission (ASE) from the signal, ensuring that it maintains a good extinction ratio before being fed back into the lower SOA. The isolators restrict the feedback to the clockwise direction. In the prototype described in the following chapter, one filter and isolator were used at the output coupler of the interferometer and another filter and isolator were used between the feedback gain element and the *Input* coupler.

The device is assumed to be a hybrid active/passive circuit. Thus it can be described by modeling the two SOAs in the interferometer and the SOA that provides a lumped gain in the feedback loop. The model used to simulate each

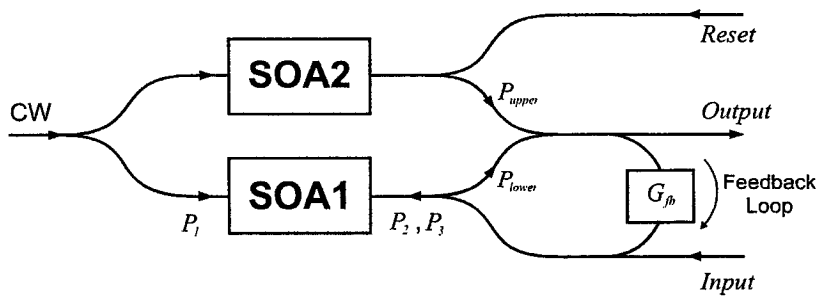

Figure 4-1 Schematic of the simulated device.

of the SOAs is closely based on [WILL95], though similar models can be found in [ASHG97] and [MARC97]. The SOAs are assumed to be connected by passive lossless waveguides. It is assumed that all the waveguide splitters and couplers are symmetrical (50:50) and have only their inherent 3 dB loss. The overall device model combines the results from each SOA with the splitter and coupler losses and the interference effects of the interferometer.

In the following discussion all variables are listed in Table 1 [WILL95], unless otherwise stated. The travelling wave and carrier rate equations for SOA1 are given, respectively, by [WILL95, ASHG97, MARC97]

$$\frac{dP_i}{dz} = \left(\Gamma g_{N,\lambda_i} - \alpha\right) P_i, \quad i = 1,2,3 \tag{4.1}$$

and

$$\frac{dN}{dt} = \frac{I}{qV} - \frac{N}{\tau_N} - \sum_{i=1,2,3} \frac{\left(\Gamma g_{N,\lambda_i} - \alpha\right) P_i}{h\nu_i S}, \tag{4.2}$$

where P_1, P_2, and P_3 represent the continuous wave (CW), input signal, and feedback optical powers, respectively, that are coupled into SOA1 (see Figure 4-1), and S is the cross-sectional area of the active waveguide.

The travelling wave equation can be derived from the general time-independent wave equation; the details can be found in Appendix A. The carrier rate equation must be derived using a density-matrix approach [AGRA86] and is beyond the scope of this thesis. It calculates the change in carrier density in the active region by balancing the addition of carriers due to injection current against the loss of carriers due to radiative and nonradiative recombinations. On the right hand side of (4.2), the first term describes the contribution of the injection current, the second term accounts for nonradiative emission and spontaneous emission, and the third term accounts for the gain of the input optical signal due to stimulated emission.

In (4.2), amplified spontaneous emission noise (ASE) is neglected for simplicity. ASE is produced when a photon produced through spontaneous emission travels along the longitudinal axis of the SOA and experiences gain. The effect on the system is to slightly reduce the gain provided by the SOA and to add noise to the *Output* and the feedback signal. A narrowband filter at the output of the interferometer can minimize the noise added to these signals. The use of the filter is possible because the device is operating with a fixed-wavelength CW input.

The material gain provided by an SOA is dependent upon the carrier density and wavelength. It is modeled using an empirical formula with a cubic dependence on the wavelength, and with a peak gain that is linearly dependent on the carrier density, giving [WILL95]

$$g = a(N - N_0) - \gamma_1(\lambda - \lambda_N)^2 + \gamma_2(\lambda - \lambda_N)^3, \tag{4.3}$$

where the peak gain spectral shift is described by [WILL95]

$$\lambda_N = \lambda_0 - \kappa_0(N - N_0). \tag{4.4}$$

The carrier lifetime dependence on the carrier density is

$$\tau_N = \left(A + BN + CN^2\right)^{-1} \tag{4.5}$$

and includes several loss mechanisms [CONN02 pg. 52]. A models nonradiative recombination due to defects, impurities, and other traps. B is the radiative recombination rate and models spontaneous emission. C approximates the effects of several Auger processes. Auger recombination involves the interaction of four electrons and holes and in some cases phonons or traps as well. The inclusion of this parameter is important for long wavelength amplifiers such as those used in communications. An entire chapter in [AGRA86] is devoted to recombination in semiconductors and for further details the reader is directed to that text.

Table 1 Parameters and values used in the numerical simulations.

Parameter	Description	Value and Units
P_i	Power	W
$g_{N,i}$	Material Gain	cm^{-1}
Γ	Confinement Factor	0.3
α	Waveguide Loss	$20\,cm^{-1}$
I	Current	$80 \cdot 10^{-3}$ A
q	Electron Charge	$1.6 \cdot 10^{-19}$ C
V	Active Region Volume	$1.5 \cdot 10^{-10} cm^3$
L	Active Region Length	$0.05\,cm$
N	Carrier Density	cm^{-3}
τ_N	Carrier Lifetime	s
$h\nu_i$	Photon Energy	J
a	Material Gain Constant	$2.5 \cdot 10^{-16} cm^2$
N_0	Transparency Carrier Density	$0.9 \cdot 10^{18} cm^{-3}$
γ_1	Material Gain Constant	$0.074 cm^{-1} nm^{-2}$
γ_2	Material Gain Constant	$3.155 \cdot 10^{-4} cm^{-1} nm^{-3}$
λ_N	Peak Material Gain Shift	nm
λ_0	Peak Material Gain Wavelength at Transparency	1605 nm
κ_0	Peak Material Gain Shift Constant	$3 \cdot 10^{-17}$ nm/cm^3
A	Nonradiative Recombination Constant	$2.5 \cdot 10^8 s^{-1}$
B	Bimolecular Recombination Constant	$1 \cdot 10^{-10} cm^3 s^{-1}$
C	Auger Recombination Constant	$9.4 \cdot 10^{-29} cm^6 s^{-1}$
$d\eta/dN$	Change in Refractive Index with Carrier Concentration	$-1.2 \cdot 10^{-20} cm^3$

Solution of the equations presented above is detailed in [MARC97]. Considering equation (4.1), separation of variables and integrating over the length of the SOA yields

$$P_i(t,L) = P_i(t,0)\exp\left[\int_0^L \left(\Gamma g_{N,\lambda_i} - \alpha\right)(z')dz'\right], \tag{4.6}$$

where z' is a dummy variable.

In the above equation, the gain, which is a function of carrier density, is shown to be also a function of z. While this is true, a good approximation can be obtained by neglecting this variation, especially in the case of counter-propagating XPM. This was verified by the author by numerically dividing an SOA into two and four sections, each with the same injection current but with independently varying carrier densities. It was found that the effect on the transfer function of the device was minor. With this approximation, we can rewrite (4.6) as,

$$P_i(t,L) = P_i(t,0)\exp\left[\left(\Gamma g_{N,\lambda_i} - \alpha\right)L\right]. \tag{4.7}$$

Another useful way to write the integration of (4.1) is

$$\int_0^L \left(\Gamma g_{N,\lambda_i} - \alpha\right)P_i\, dz' = P_i(t,L) - P_i(t,0) = \left(\exp[\left(\Gamma g_{N,\lambda_i} - \alpha\right)L] - 1\right)P_i(t,0). \tag{4.8}$$

Now integrating (4.2) over the length of the SOA, using (4.7) and (4.8), we obtain

$$\frac{dN}{dt} = \frac{I}{qV} - \frac{N}{\tau_N} - \frac{1}{h\nu_i SL}\sum_{i=1,2,3}\left(\exp[\left(\Gamma g_{N,i} - \alpha\right)L] - 1\right)P_i(t,0). \tag{4.9}$$

If detailed comparison with [MARC97] is carried out, it should be noted that two minor typographical errors exist in equation 7 of that paper. Also in that paper, the transparency carrier density is assumed to vary with wavelength. This is an important consideration when modeling wavelength conversion; however, for our model it is assumed that the signal and CW inputs are of similar wavelength and so only one value of transparency is used. On the other hand, the frequency

difference between CW and signal inputs is assumed to be large enough that FWM is negligible.

For the steady state case, the left hand side of (4.9) is set to zero, yielding

$$0 = \frac{IL}{qV} - \frac{NL}{\tau_N} - \sum_{i=1,2,3} \frac{\left(\exp[(\Gamma g_{N,\lambda_i} - \alpha)L] - 1\right)P_i}{h\nu_i S}. \tag{4.10}$$

When steady state modeling is carried out, this equation is used to solve for the carrier density N in the SOA. For dynamic simulations, the steady state equation is solved using the initial conditions. Subsequent points are then found by applying Euler's method to (4.9). Error was minimized by using a sufficiently small time-step to capture the dynamics of the system. In this thesis, time-steps ranging from 1 ns to 10 ps were used.

The relationship between the accumulated phase shift of the optical signal and the refractive index of the SOA is obtained using the same derivation as that for the travelling wave equation and is given by

$$\frac{\partial \Delta\phi}{\partial z} = \Gamma k_1 \Delta\eta, \tag{4.11}$$

where k_1 is the wavenumber of the CW source. Integrating over the length of the SOA, and assuming a linear dependence of refractive index to carrier density, yields [ASGH97]

$$\Delta\phi = \frac{2\pi L\Gamma(N - N_0)}{\lambda_1}\frac{d\eta}{dN}, \tag{4.12}$$

where λ_1 is the wavelength of the CW source. SOA2 is modeled using similar equations as those presented.

The waveguide junctions (couplers and splitters) can be described using the S matrix approach [SANC91, MWAR92, LEUT98]. The three port Y junction at the left side of the interferometer is described by

$$\begin{bmatrix} E_{OUT1} \\ E_{OUT2} \\ E_{OUT3} \end{bmatrix} = \begin{bmatrix} 0 & \sqrt{\frac{1}{2}} & \sqrt{\frac{1}{2}} \\ \sqrt{\frac{1}{2}} & 0 & 0 \\ \sqrt{\frac{1}{2}} & 0 & 0 \end{bmatrix} \begin{bmatrix} E_{IN1} \\ E_{IN2} \\ E_{IN3} \end{bmatrix}, \tag{4.13}$$

where it is assumed the junction is symmetric with a 50:50 splitting ratio [NISH85]. The variables in the two vectors represent the input and output complex field amplitudes at each port as shown in Figure 4-2. Likewise, the five port coupler to the right of the interferometer is described by

$$\begin{bmatrix} E_{OUT1} \\ E_{OUT2} \\ E_{OUT3} \\ E_{OUT4} \\ E_{OUT5} \end{bmatrix} = \begin{bmatrix} 0 & 0 & \sqrt{\frac{1}{2}} & \frac{1}{2} & 0 \\ 0 & 0 & 0 & \frac{1}{2} & \sqrt{\frac{1}{2}} \\ \sqrt{\frac{1}{2}} & 0 & 0 & 0 & 0 \\ \frac{1}{2} & \frac{1}{2} & 0 & 0 & 0 \\ 0 & \sqrt{\frac{1}{2}} & 0 & 0 & 0 \end{bmatrix} \begin{bmatrix} E_{IN1} \\ E_{IN2} \\ E_{IN3} \\ E_{IN4} \\ E_{IN5} \end{bmatrix}, \tag{4.14}$$

where, again, the variables are shown in Figure 4-2.

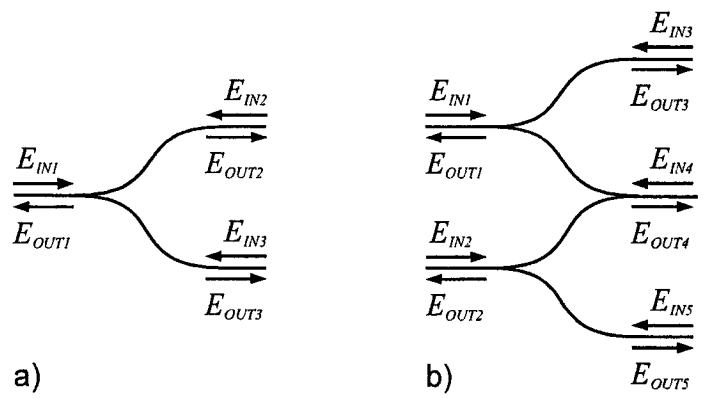

Figure 4-2 Schematic diagram of the a) three port and b) five port junctions.

Using (4.13), it can be shown that the power exiting the interferometer is

$$P_{total} = \frac{1}{2}\left(P_{upper} + P_{lower} + 2\sqrt{P_{upper} \cdot P_{lower}} \cos\Delta\theta\right), \tag{4.15}$$

where P_{upper}, P_{lower} and $\Delta\theta$ represent the optical powers and the phase difference between the two waves at the output-coupler of the waveguide interferometer where the two waves interfere. This term includes the phase shifts imparted by the SOAs, given by (4.12), and any additional phase shifts produced by possible unequal arm lengths. This equation is consistent with [NISH85 pg.40]. It should be noted that the equation given by Connelly [CONN02 pg.141] is incorrect and differs by a factor of one half. That equation fails to consider that in a single mode waveguide, power coupled into higher-order modes is radiated by the waveguide and lost.

The simulations were performed using Mathematica software. By default, this program performs real-number calculations using the number of significant digits determined by the machine precision [WOLF96 pg.703]. In this case the machine precision was 16 digits. In addition, Equation (4.9) was normalized to make each of the terms similar in order.

4.2 SIMULATING A SINGLE SOA

The equations presented in Section 4.1 were used to model a single SOA. Using typical parameter values, some basic SOA behaviors were simulated to ensure that the model was operating properly.

If spontaneous emission was measured, without the effects of amplified spontaneous emission, the spectra would conform to the gain curves shown in Figure 4-3. The carrier densities for the various curves correspond to injection currents of 20 mA, 40 mA, 60 mA, and 80 mA, with no optical input. With increasing carrier density the peak gain increases and shifts to shorter wavelengths. If a saturating optical input were applied to the device, the carrier density would decrease inside the amplifier, and the peak gain would drop and shift accordingly.

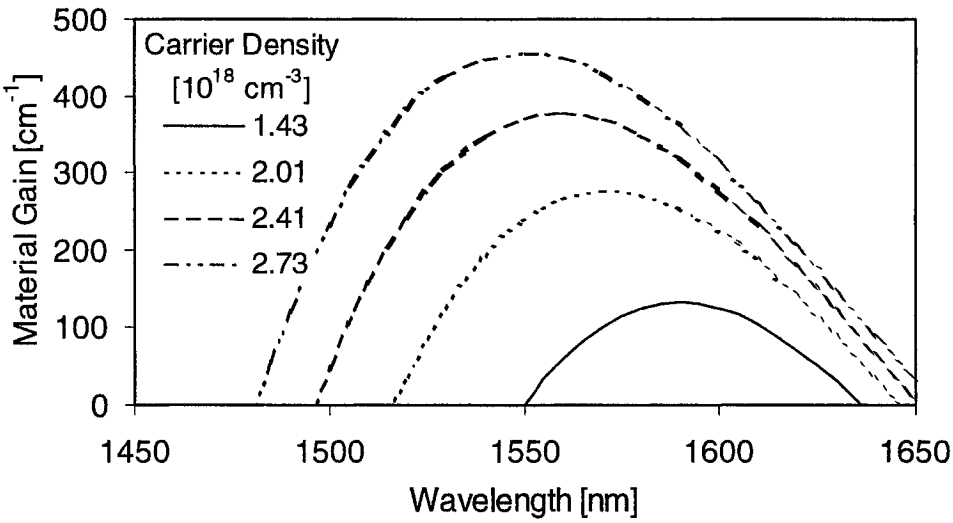

Figure 4-3 Material gain, as a function of wavelength, of a single SOA at various carrier densities.

By fixing the injection current and varying the input power, gain saturation of the amplifier is observed, as shown in Figure 4-4. The figure shows relatively constant gain for small input powers, with the gain decreasing for progressively larger input powers. The maximum gain is several decibels higher than the gain measured experimentally in an SOA from Axon Photonics; however, the commercial device experiences losses due to coupling with the optical fiber at each end of the SOA. These losses are on the order of 3 dB [CONN02]. For larger input powers than are shown in the figure, the theoretical curve asymptotically approaches 0 dB. This is reasonable, for if it is assumed that the amplifier would not be damaged by such large optical inputs, we would expect the amplifier to add negligible power to a very large optical signal being amplified.

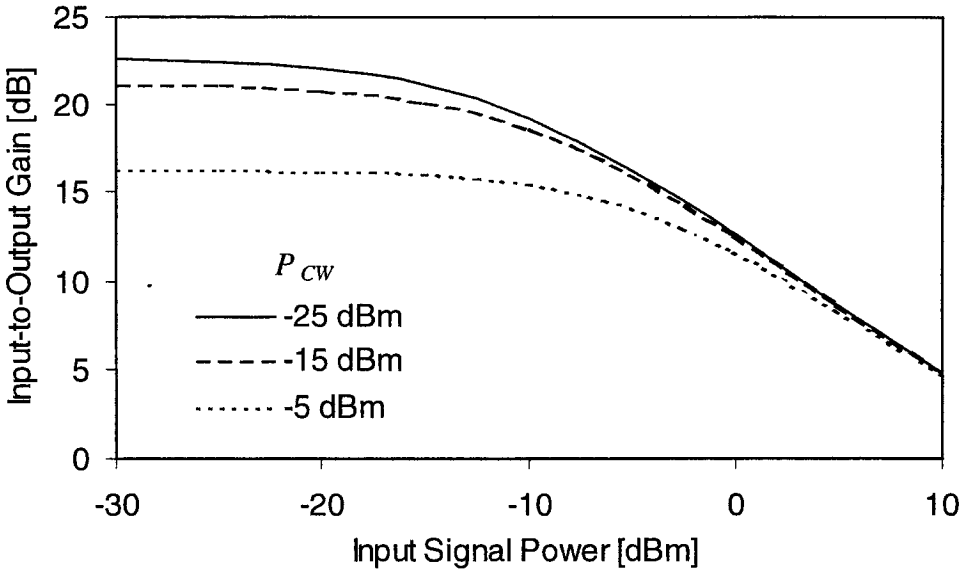

Figure 4-4 Input-to-output gain of an SOA as a function of *Input* signal power, for various values of CW input power.

4.3 SIMULATING A MACH-ZEHNDER INTERFEROMETER

As discussed in Chapter 3, the nonlinear effect of gain saturation of an SOA in the arm of an MZI can be used to perform all-optical signal processing. Depending on the geometry and operating conditions, various functions can be achieved. This section begins by simulating an MZI-SOA without feedback to confirm that the model works as expected. Next, feedback is applied to the MZI. A patented feedback design [ROBE99b, CLAV04] is simulated and shown to suffer from serious limitations in the resetting of the flip-flop. An alternative design is proposed that uses a three-level input, but it is shown to have a different problem with the reset. In this case, critical slowing down severely limits the turn-off response time of the flip-flop. Finally, a third design is proposed, which solves the problems related to the first two designs.

4.3.1 Simulation of an MZI Without Feedback

To begin, the results of simulations carried out on a Mach-Zehnder without feedback are presented. As discussed previously, such a device can be used for a variety of applications including wavelength conversion, regeneration, and for logical operations.

According to equation (4.3), the gain of an SOA is dependent upon the carrier density, N. Thus in Figure 4-4, as the gain drops, so does the carrier density. The phase delay imparted by the SOA to the optical modes travelling through it also depends on the carrier density, according to equation (4.12). The phase delay, plotted as a function of input signal power and with a CW power of -15 dBm, is shown in Figure 4-5, where the phase is measured relative to the phase produced when the input signal power is -30 dBm. When used in an MZI, a phase shift of π radians is required for complete switching. In this example this could be accomplished with a change in input signal power from -10 dBm to 4 dBm, a 14 dB extinction ratio. This can easily produce a 20 dB or more extinction ratio in the output signal of the MZI.

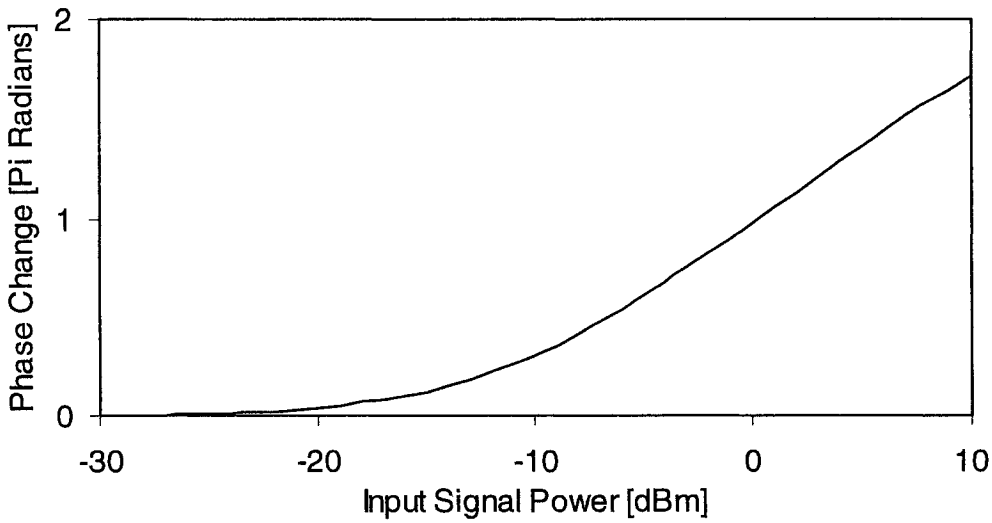

Figure 4-5 Phase change of CW beam in response to signal power.

Now that the phase shift imparted by the SOA to the CW wave is known, the entire MZI, shown in Figure 4-6, can be modeled. Rewriting equation 4.15 in terms of the CW bias power, P_{CW}, gives

$$P_{OUT} = \frac{P_{CW}}{8}\left(G_{upper} + G_{lower} + 2\sqrt{G_{upper}G_{lower}}\cos\left(\theta_{upper} - \theta_{lower}\right)\right) \qquad (4.16)$$

where G_{upper} and G_{lower} are the gains experienced by P_{CW} in the upper and lower SOAs, respectively. θ_{upper} and θ_{lower} are the total phase shifts accumulated by the CW waves in the upper and lower arms of the MZI, respectively. The G and θ terms must be determined numerically.

The transfer function of the MZI can be controlled and tailored to the specific application. Two possible transfer functions are shown in Figure 4-7. In those two cases the phase and the optical power from the unmodulated arm of the MZI have been designed to be exactly equal to those in the modulated arm when the *Input* power is –15 dBm and 0 dBm, respectively. These are referred to as noninverting and inverting transfer functions, respectively. In general, a wide variety of curves are possible. In Figure 4-7 the destructive interference is shown to lead to an output extinction ratio of, theoretically, infinity. In practice two limitations restrict the extinction ratio. The first is spontaneous emission and amplified spontaneous emission, generated by the SOAs, that falls within the bandwidth of the filters in the feedback loop. The second is variation in the gain and phase shift imparted by the SOAs on the CW light, due to electrical biasing drift. While these effects are very difficult to model accurately, the restricted extinction ratio can be approximated in the model by mismatching the power in the unmodulated arm so that there is not perfect interference. In the model developed in this thesis, the mismatch is designated as the *arm-power ratio* (*APR*) which is defined here as

$$APR = \frac{P_{upper}}{P_{lower}}, \qquad (4.17)$$

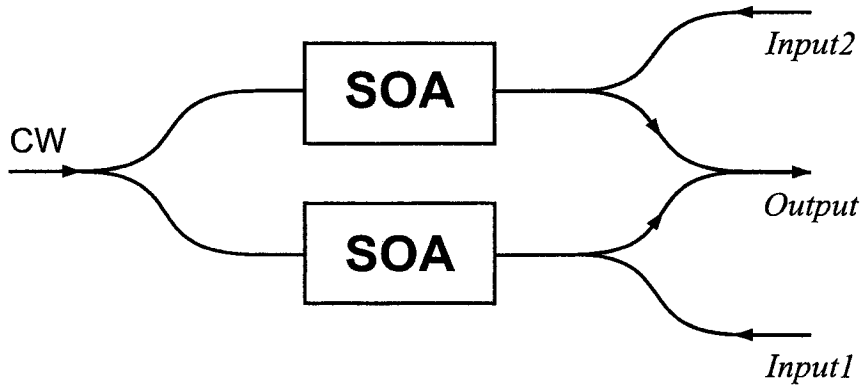

Figure 4-6 Block diagram of an MZI-SOA without feedback.

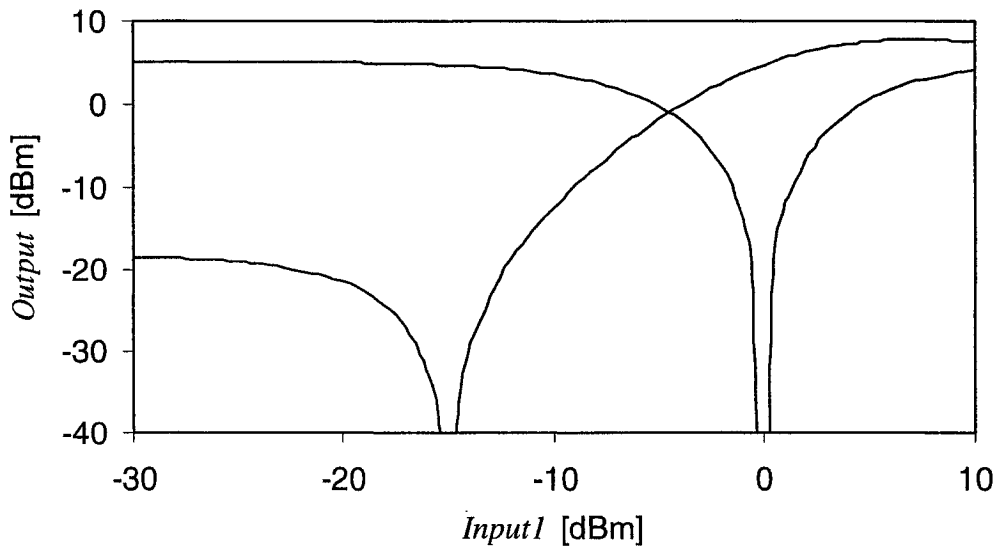

Figure 4-7 Simulated transfer functions of an MZI-SOA.

measured when the arm phase difference is π. An example of the effect of $APR \neq 1$ on the transfer function is shown in Figure 4-8. This technique is not used in other literature, but is reasonable as it is physically possible to control P_{upper} and P_{lower}. In addition, it does not significantly alter the shape of the transfer function other than at the point of maximum destructive interference.

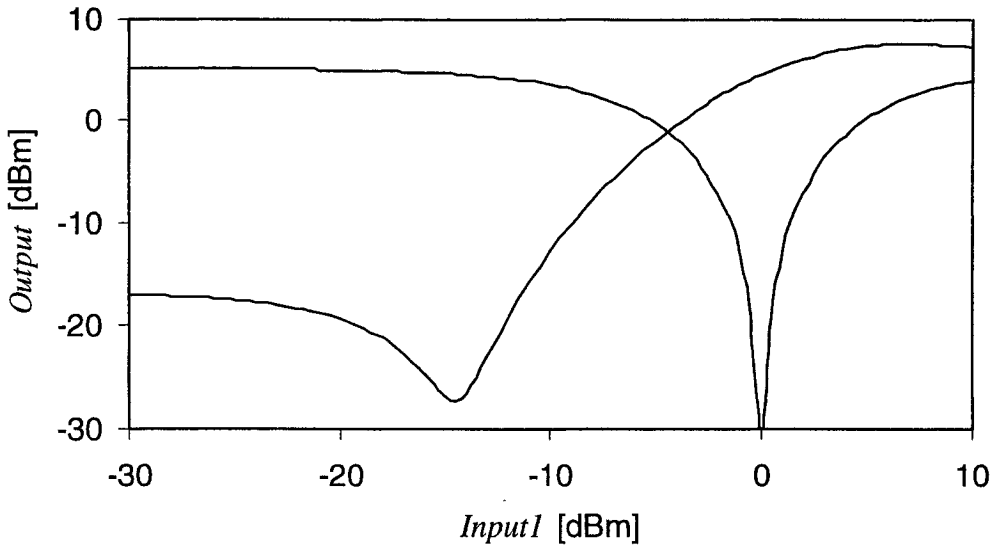

Figure 4-8 Simulated transfer functions of an MZI-SOA with an arm-power ratio (*APR*) of 0.95.

For the purpose of wavelength conversion, either noninverting or inverting transfer functions may be used. For logic gates, specific transfer functions are required. Only the XOR gate will be considered here, as it has relevance to later discussions. An XOR gate is constructed as shown in Figure 4-6. In this case it is necessary to have a noninverting transfer function with respect to both *Input1* and *Input2*. When both of the inputs are high, the two SOAs produce the same phase shift and the output becomes low. This behavior is shown in Figure 4-9.

It is also useful to briefly discuss some dynamic properties of the MZI-SOA. The two main mechanisms that control the speed of an MZI-SOA are the carrier lifetime and the travelling wave effect.

The carrier recombination rate is described by [AGRA86 pg. 36]

$$R = AN + BN^2 + CN^3 + R_{st}N_{ph}, \tag{4.18}$$

where N_{ph} is the photon density in the active region and R_{st} is the stimulated emission rate given by

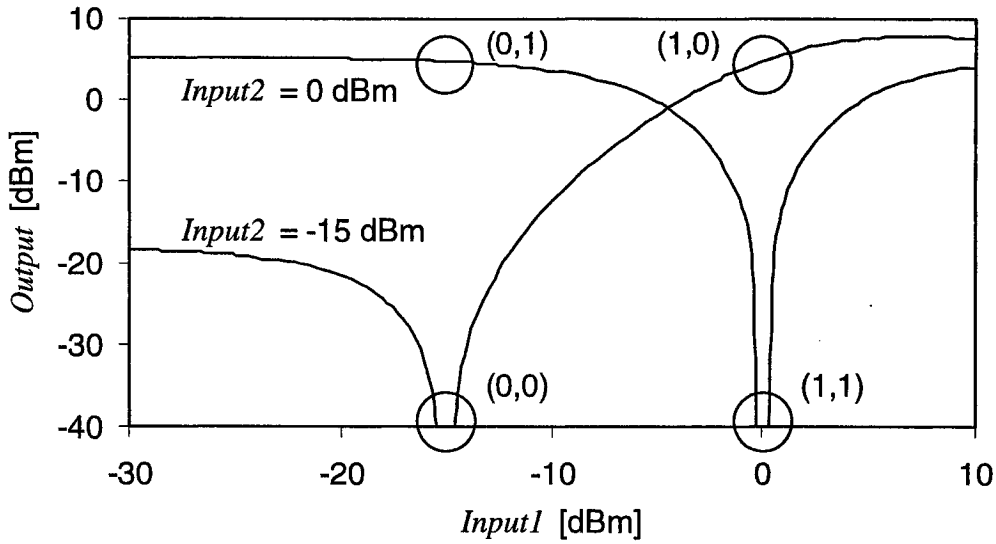

Figure 4-1 Static transfer functions relating to the XOR gate. Shown is the *Output* related to *Input1* when *Input2* is low and high. The circles represent the four logical states for the gate.

$$R_{st} = \frac{c\, g(N)}{\eta_g}, \tag{4.19}$$

where c is the speed of light, $g(N)$ is given by (4.3), and η_g is the group index given by [SALE91 pg. 189]

$$\eta_g = \eta - \lambda \frac{d\eta}{d\lambda}. \tag{4.20}$$

Fast SOA response times are achieved through a both high carrier density and a high photon density. Externally, this is achieved by using large injection currents and intense optical inputs [ASGH97].

The travelling wave effect was discovered in 1995 when wavelength conversion experiments had bandwidths higher than what was expected by considering the carrier response time alone [DAVI95]. The effect has since been studied through both simplified analytical models and numerical calculations [DAVI95], [MARC95], [MECO96], [Mark97], [ASGH97]. The traveling wave effect occurs when the leading edge of an input pulse reduces the carrier density

through stimulated emission. The stimulated emission response time is much faster than the carrier recovery time, thus the leading edge of the pulse is greatly amplified, but the remainder of the pulse experiences a reduced or compressed gain (often described as gain quenching when discussing bistable laser diodes). As an example, Figure 4-10 shows what the input pulse looks like after it has passed through a 750 μm SOA with 105 mA injection current. As the intense leading edge travels through the SOA it quickly depletes the carriers causing a fast change in refractive index. At the trailing edge of the pulse the reverse occurs; when the pulse ends, the carrier density is slow to recover. Thus the power of the pulse drops to a very low level before recovering. This distortion amplifies the high frequency content of the input switching pulse as it travels through the SOA. When combined with the low-pass characteristics of the carrier response, it acts to extend the bandwidth of the SOA. High carrier densities and long SOA lengths increase the travelling wave effect.

As discussed, controllable parameters that influence the speed of an MZI-SOA include injection current, CW input power level, and the length of the SOAs. Simulations were carried out for several values of each of these parameters to

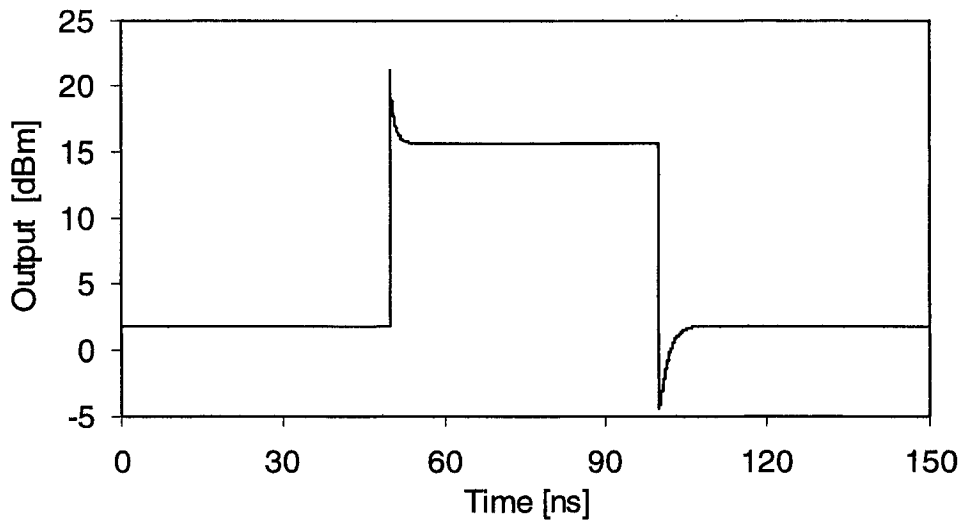

Figure 4-10 The input pulse after it has passed through the SOA. It is distorted by the travelling wave effect.

demonstrate how switching times were affected. In each case the input pulse was rectangular. The results are given in Table 2 for a varying injection current, in Table 3 for a varying SOA length, and in Table 4 for a varying CW input power. In Table 3, the injection current density was held constant as the length of the SOA increased. The time step used for these calculations was 50 ps, except for the two longest SOAs for which the time step was 10 ps. An increased injection current and SOA length have the largest impact on the rise and fall times of the MZI.

Another simulation was performed in which all three parameters investigated above were modified. In that simulation SOA length was 1 mm, injection current was 200 mA, and input power was 0 dBm. The rise and fall times of the output pulse of the modulated MZI-SOA were 0.62 ns and 0.50 ns, respectively, indicating that the highest speed is obtained when all these parameters are increased.

4.3.2 Simulation of the Patented Flip-Flop

Of specific interest to this thesis is the application of feedback to the basic MZI for the purpose of designing a flip-flop or a memory element. This section considers a patented design [ROBE99b]. It will be shown, both conceptually and through dynamic simulations, that this patented design suffers from a design limitation related to the resetting of the flip-flop. A diagram of the device is shown in Figure 4-11. In fact, the diagram of the device in the patent does not show a gain element in the feedback loop. Rather, feedback gain is discussed in the text where it is explained that the feedback gain must be designed to be sufficient to hold the device in a high logical state after being set.

Table 2 Rise and fall times of an Output pulse from a modulated MZI-SOA, as a function of SOA injection current. The length is 0.5 mm and the CW input power is –6 dBm.

Injection Current [mA]	Rise Time [ns]	Fall Time [ns]
50	8.15	8.25
70	4.45	5.55
90	2.85	4.10

Table 3 Rise and fall times of an Output pulse from a modulated MZI-SOA, as a function of SOA length. The injection current is 70 mA and the CW input power is –6 dBm.

Length [mm]	Rise Time [ns]	Fall Time [ns]
0.50	4.45	5.55
0.75	1.38	2.39
1.00	0.56	1.26

Table 4 Rise and fall times of an Output pulse from a modulated MZI-SOA, as a function of CW input power. The injection current is 70 mA and the length is 0.5 mm.

CW Input Power [dBm]	Rise Time [ns]	Fall Time [ns]
-6	4.45	5.55
-3	4.95	4.35
0	5.00	3.35

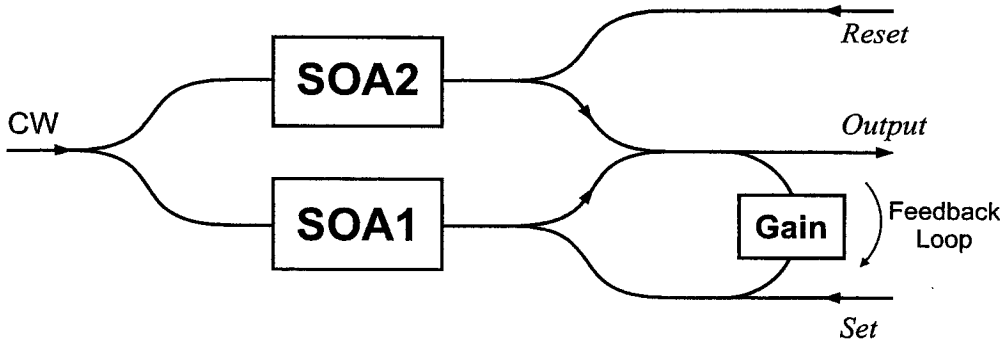

Figure 4-11 Diagram of the patented flip-flop design. There are two binary inputs: *Set* and *Reset*. Note that the *Reset* does not have a direct impact on the feedback loop.

In this flip-flop, the MZI is designed and operated such that the output of the interferometer is low when the *Set* and *Reset* are low. Thus the outputs of the two arms of the interferometer are initially out of phase as in the noninverting case. To set the flip-flop, a pulse is applied to the *Set* input. The presence of the *Set* pulse causes the *Output* to go high. The feedback loop allows some of this output optical power to be fed back into SOA1. Even after the *Set* pulse ends, there is sufficient power being fed back into SOA1 to maintain the high *Output*. For the *Output* to remain continuously high, the whole feedback loop must be filled with light. Thus the *Set* pulse must remain present until the resulting high *Output* from the interferometer arrives at the *Set* input coupler.

The static transfer function relating the *Output* optical power of the flip-flop to the applied optical power at the *Set* input is shown in Figure 4-12, for various amounts of feedback gain. The logic high *Set* power must be chosen so that it is greater than the power of the upward transition of the bistability in the transfer function. The logic low *Set* power must be chosen so that the transfer function is multivalued. For instance, low and high *Set* powers of -20 dBm and 0 dBm are suitable to be used with a feedback gain of 1.6 but are not suitable for a feedback gain of 1.5. While it would be difficult to control the feedback gain this precisely, gains larger than 1.6 are also suitable.

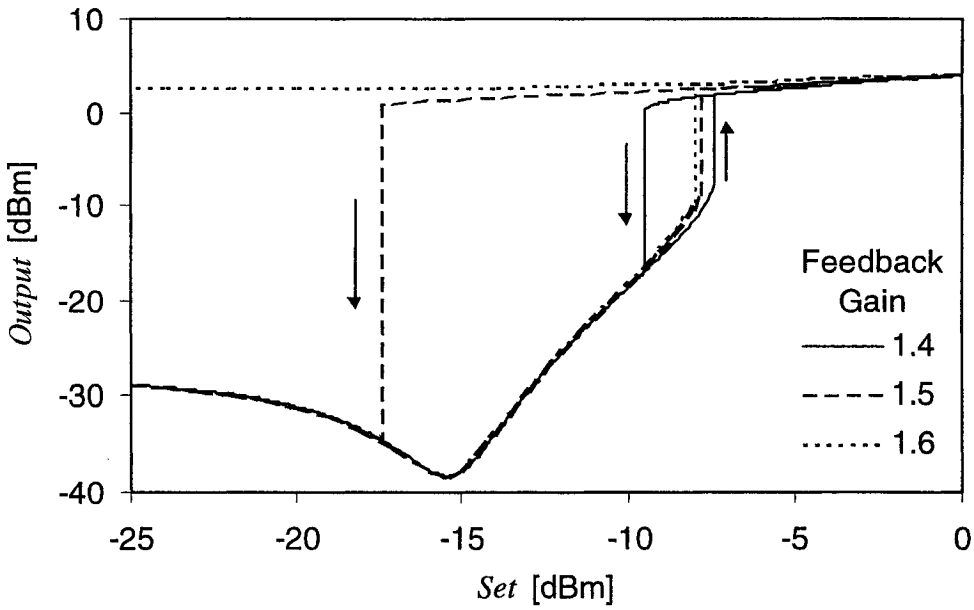

Figure 4-12 Static transfer function of patented flip-flop with respect to the *Set* input for various values of feedback gain.

In Figure 4-12, the downward transition of the curve associated with a feedback gain of 1.6, occurs at a *Set* power below -25 dBm. Each curve in the plot is considered an S-shaped bistability. Theoretically, the upper and lower parts of the transfer function are connected by an S-shaped curve, but because it represents a physically impossible operating region, it is not shown in the figure. It can, however be calculated with the model by assuming an output power and working backwards through the equations. This is a standard technique used in nonlinear systems.

To return the flip-flop to its low state, a pulse is applied to the *Reset* input. The relative phase shift between the arms returns to near zero because there is a strong optical signal in both the upper and lower arms of the interferometer. This causes the *Output* of the interferometer to go low. Ideally, at the end of the *Reset* pulse, there is no longer any optical power at either input or in the feedback arm, and the device thus returns to its initial low state.

The problem with this design is that the interferometer is acting as an XOR gate, with the *Reset* as one logical input and the sum of the *Set* and feedback signals as the second logical input. Only when the signals applied to each SOA are of the same power, will the phase shift in each arm be the same, and the *Output* power of the interferometer will be low. Assume the flip-flop has already been set. Initially, a *Reset* pulse will cause the *Output* to go low. This low will propagate around the feedback loop to SOA1. If the *Reset* pulse is still high, then the inputs into SOA1 and SOA2 are no longer the same, and the *Output* of the interferometer returns to a high state. For proper operation it becomes necessary to match the duration of the *Reset* pulse to the delay of an optical signal travelling around the feedback loop. If this is not the case, then the feedback loop will be partially filled with higher intensity light. If we consider this light to represent a pulse, the pulse circulates around the feedback loop. It appears repeatedly at the flip-flop *Output*, producing an oscillating output intensity that continues even after the *Reset* pulse has ended. The oscillations may eventually decay, or it may be necessary to once again set the flip-flop to clear the oscillations. Whatever the case, even a single oscillation is intolerable.

Even with the assumption that the duration of the *Reset* pulse is correct, there can be problems. For instance, if there are two *Reset* pulses in series, the second pulse will again cause the input powers into the two SOAs to be asymmetric, and the *Output* will go high. Thus, the flip-flop has been set by a *Reset* pulse. This design would simply not be useable in practical communication systems.

To demonstrate the behaviors discussed above, dynamic simulations of the patented flip-flop were performed, and the results are shown in Figure 4-13. The figure shows the device *Output* response to a *Set* pulse followed by a *Reset* pulse. It demonstrates the effect of the duration of the *Reset* pulse on the operation of the flip-flop by using *Reset* pulses shorter than, equal to, and longer than the feedback loop delay, respectively. In this simulation the feedback delay is

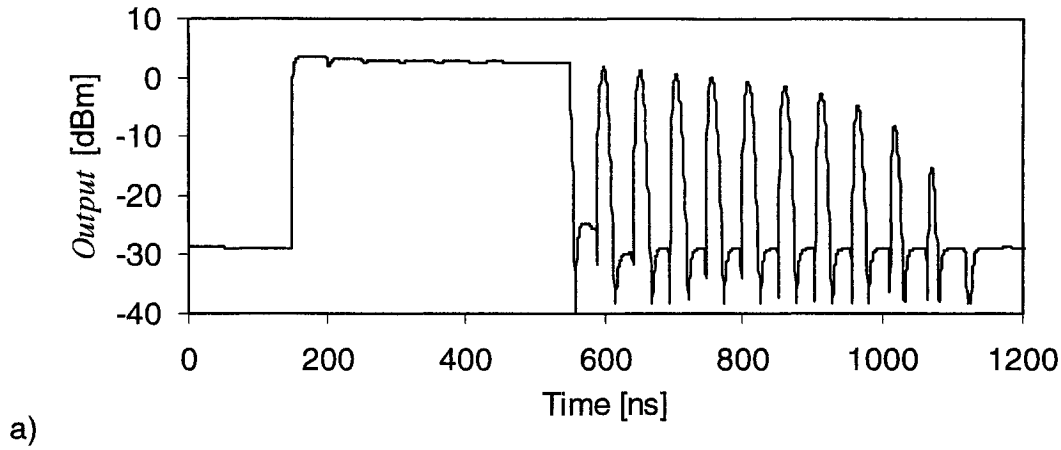

a)

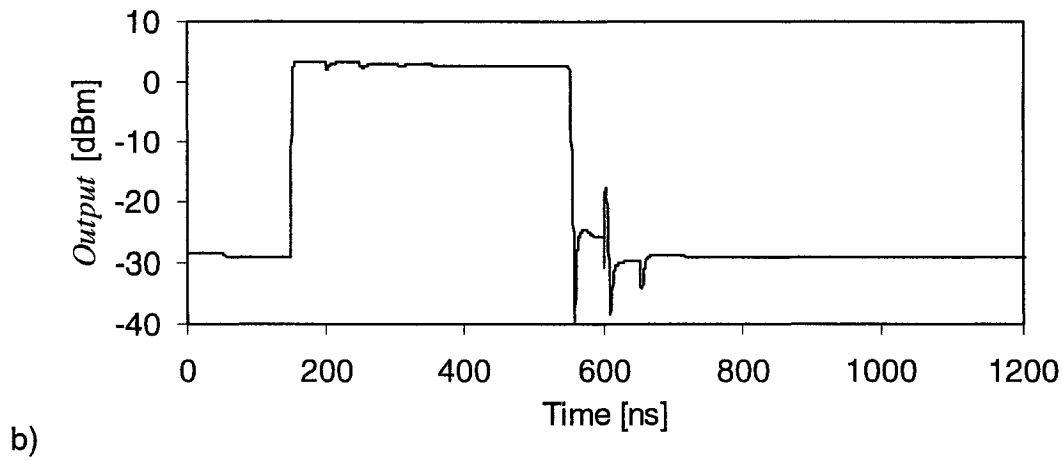

b)

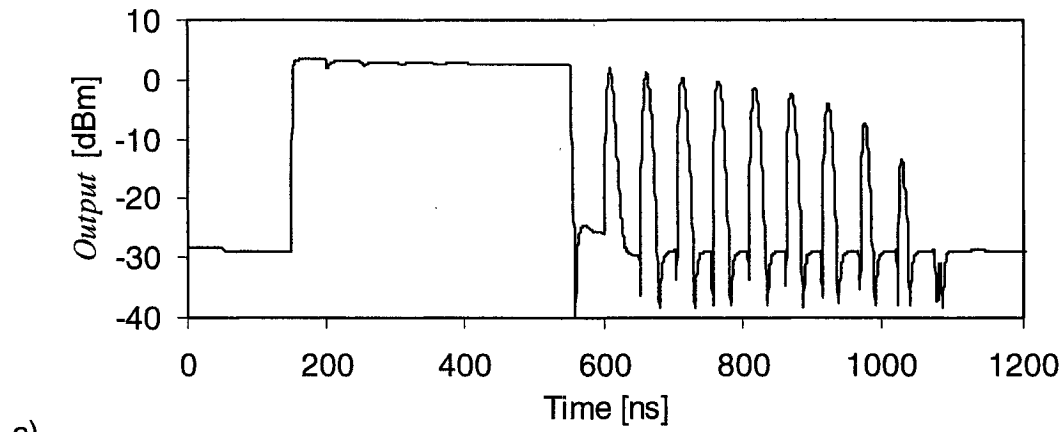

c)

Figure 4-13 Dynamic simulation highlighting the effect of the duration of the *Reset* pulse on the operation of the flip-flop. The *Reset* pulse durations used are a) 40 ns, b) 50 ns, and c) 60 ns.

assumed to be 50 ns and the three *Reset* pulse durations considered are 40 ns, 50 ns, and 60 ns, respectively.

As expected, a *Reset* that is shorter than the feedback delay results in improper behavior. This is the same type of oscillatory behavior that would occur with a *Set* pulse that is shorter than the feedback delay, and cannot be avoided. When the pulse duration is equal to the feedback delay, the device works properly, but as it will be shown, this proper behavior cannot be expected in practical situations. Finally, when the *Reset* pulse duration is greater than the feedback delay, the flip-flop is shown to oscillate as predicted.

The maximum power of the oscillations represents a measure of performance for the flip-flop. Larger oscillations reduce the extinction ratio of the output, leading to an increased chance of bit errors. Figure 4-14 plots the maximum output power of the oscillations as a function of *Reset* pulse duration. From this graph the restriction on the pulse duration is clear. In this particular case the ideal *Reset* pulse duration appears to be slightly longer than the loop

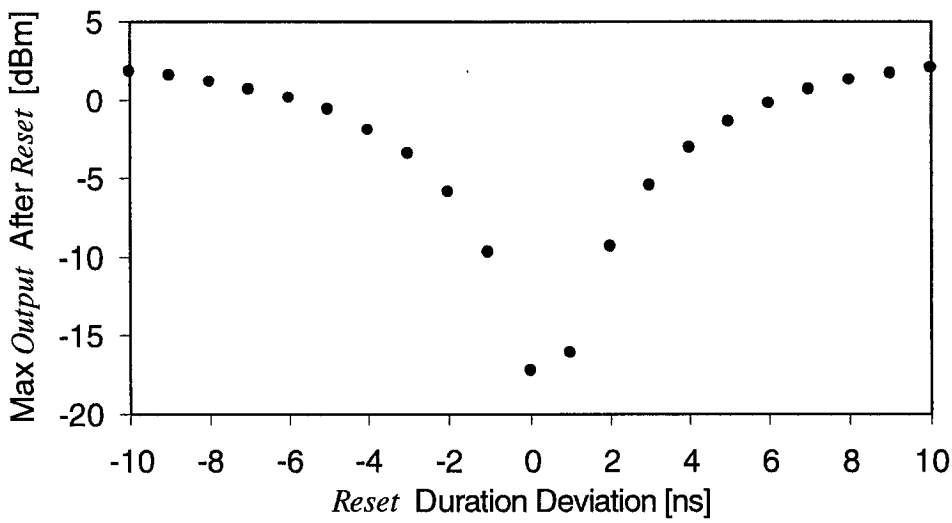

Figure 4-14 The maximum power of the *Output* oscillations, upon reset of the flip-flop, as a function of the difference between the *Reset* duration and the loop delay.

delay, due to the slow response (gain recovery) of the SOAs in the interferometer. For higher speed SOAs the ideal pulse duration would approach the loop delay.

The acceptable range of *Reset* pulse durations is also reduced when higher speed SOAs are used. A simulation was performed using 1 mm SOAs, with injection currents of 140 mA. The feedback gain was lowered to 0.5 dB because more power was available from the MZI. The maximum power of the *Output* oscillations increased from -25.7 dBm when the *Reset* pulse duration was equal to the loop delay, to -6.5 dBm when the time difference varied by only 200 ps. These results are expected, because faster SOAs are able to respond to smaller differences between the pulse duration and the loop delay.

In the simulations summarized by Figure 4-13, the maximum power of the *Output*, after being reset, is also impacted by the power of the *Reset* pulse. If the pulse power is not optimized, the destructive interference at the output of the interferometer will be incomplete. To select the *Reset* power used in the previous simulations, various simulations were performed with the reset pulse duration equal to the loop delay and with the pulse power varying in increments of 1 dBm. The selected pulse power minimized the *Output* after the flip-flop was reset. The sensitivity of the *Output* to the *Reset* power is shown in Figure 4-15. The *Output* is shown to deteriorate by more than 5 dB with variations in *Reset* power of only 1 dB.

Another problem can also occur with this flip-flop design. A *Reset* pulse applied to a flip-flop that has already been reset causes it to be set. Again, this can be understood by considering the MZI as an XOR gate. With the feedback loop initially low, a high *Reset* input causes the *Output* to go high. Results of a simulation of this behavior are shown in Figure 4-16. This is undesirable behavior in a flip-flop and input signal conditioning logic would be necessary to prevent it.

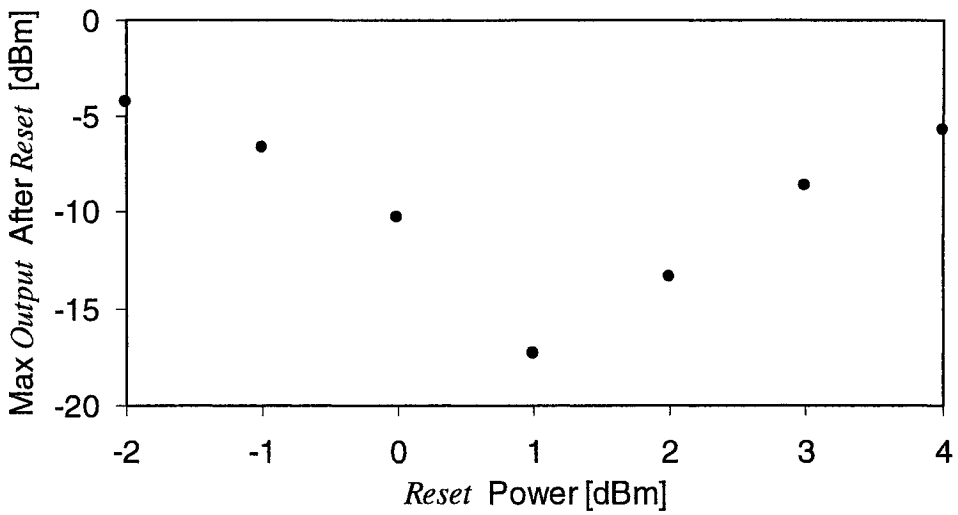

Figure 4-15 The maximum power of the *Output*, upon reset of the flip-flop, as a function of the power of the *Reset* pulse.

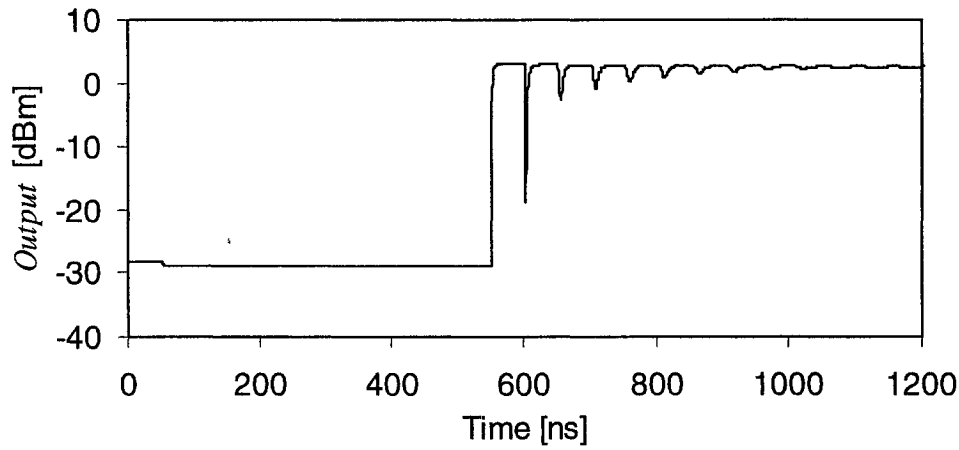

Figure 4-16 *Output* response to *Reset* pulse, while already reset.

4.3.3 Simulation of the Three-Level-Input Flip-Flop

To circumvent the problems related to the patented flip-flop design, an alternative design, proposed by the author, was explored. It uses a full hysteresis loop, and it is operated as many bistable devices are, optically biased in the middle of the

hysteresis. Pulsed increases in the input power, relative to the bias level, are used to set the flip-flop. Pulsed decreases in input power, relative to the bias power, are used to reset the flip-flop. The input signal representing the three input power levels, the *Set*, the *Reset*, and the bias, will be referred to here as the *Three-Level Input* (*TLI*) to distinguish it from the *Set* input of the patented flip-flop design. The overall flip-flop will be referred to here as the TLI flip-flop and is shown in Figure 4-17.

Reduction of the feedback gain, relative to that used in the patented flip-flop, creates a complete bistable loop in the static transfer function. An example is the curve in Figure 4-12 with a feedback gain of 1.5. The use of such hysteresis loops for the purposes of optical memory have been well studied using other optical systems [KAWA94]. The main benefit of the TLI flip-flop over the patented flip-flop is that the signals to set and to reset the flip-flop both have a direct impact on the optical power injected into SOA1 and as will be shown, this eliminates the oscillation problems associated with the patented flip-flop.

A significant disadvantage of bistable systems of this sort is that simple binary input pulses cannot be used to control the bistable element directly. However, it is possible to convert the typical binary *Set* and *Reset* signals into this composite *Three-Level-Input* used to control the flip-flop. One possible method is shown in Figure 4-18, using another Mach-Zehnder interferometer. The MZI is

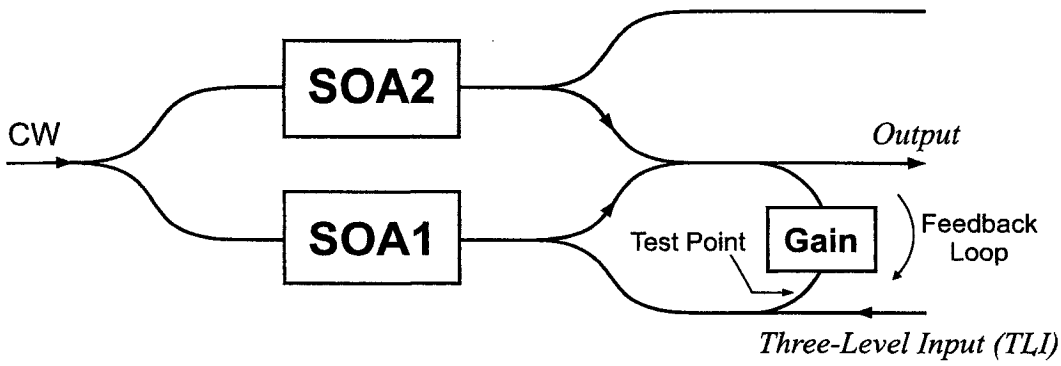

Figure 4-17 Schematic of a proposed flip-flop using a *Three-Level Input*. The test point is used later in this section.

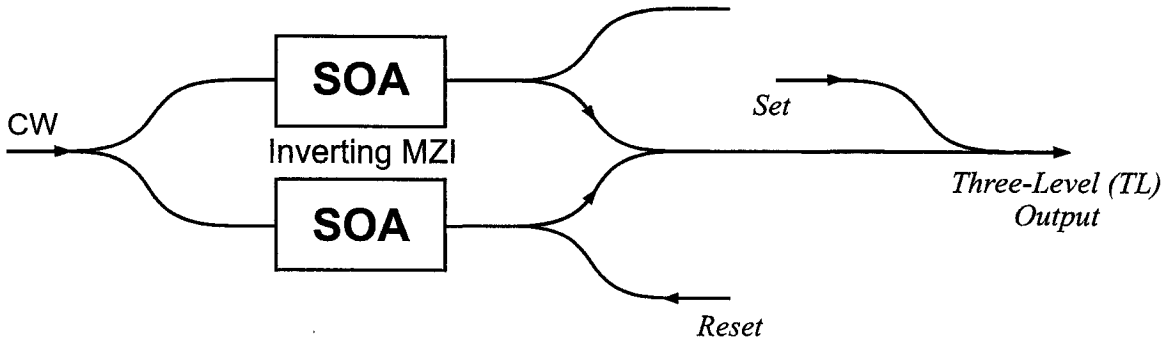

Figure 4-18 Schematic demonstrating how to convert from independent, binary *Set* and *Reset* signals to a composite *Three-Level* signal.

operated with an inverting transfer function. To prevent interference problems at the output coupler, the *Set* and the CW are assumed to be optically phase independent or assumed to operate at different wavelengths. Phase independence is realistic because the source lasers are independently controlled and the path length between each source and the coupler will change with temperature. When both the *Set* and *Reset* are low, the MZI has a mid-range output power that is designed to correspond to the bias power required by the flip-flop. When the *Reset* is high, the output of the MZI is low. When the *Set* is high, the *Three-Level Output* is also high.

The TLI flip-flop solves the problem of the oscillations associated with the reset, as will be shown later in this section. However, it will also be shown that the TLI flip-flop suffers from another problem called critical slowing down (CSD). The theory of critical slowing down is covered in detail in [WANG97], for the case of bistable laser diodes with S-shaped bistabilities. Using the nomenclature of [WANG97], the switch-up input power and switch-down input power of the hysteresis curve shown in Figure 4-12 are called critical points. Critical slowing down of the transition between bistable states occurs when the power of the switching signal remains close to the critical point. Critical slowing down is a concern for every flip-flop design in this thesis, just as it is a concern for many bistable laser-diode memories [TOMI86, UENO96]. It can be avoided in the

other flip-flop designs, and in the setting of the TLI flip-flop, but will be shown to be unavoidable in the resetting of the TLI flip-flop.

The critical slowing down associated with the setting of the flip-flop can be avoided by using a sufficiently intense *Set* pulse. In this way the switching signal quickly moves away from the critical point. Figure 4-19 demonstrates the response of the flip-flop to two input step functions. In both cases the flip-flop begins in a logic low state and is biased with a *Three-Level* power of –15 dBm. In one case the *Set* has a power of –7.5 dBm, which is just slightly larger than the critical point switching power of –7.76 dBm. The effects of critical slowing down are observed. In the second case, a *Set* power of 0 dBm is used, reducing the switching time by roughly a factor of ten.

By using step functions with small differences between power levels, the effects of critical slowing down can be more precisely investigated. Figure 4-20 shows the transient response of the flip-flop to small amplitude step functions. The starting input power in each case is –7.8 dBm, and it steps to -7.7 dBm, -7.6 dBm, -5 dBm, and +5 dBm, respectively. Again, the critical point switching

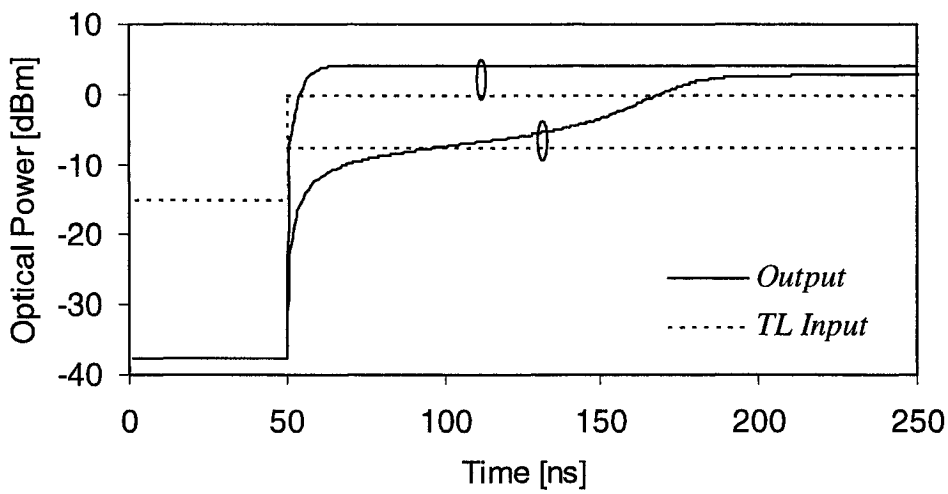

Figure 4-19 Setting the three-level flip-flop with and without the effect of critical slowing down. The loops indicate the associated *TL Input* and *Output* curves.

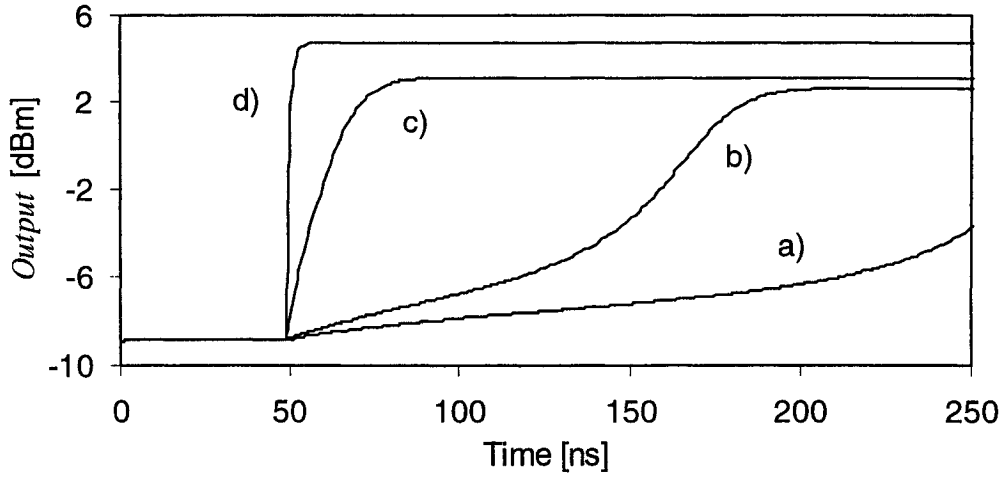

Figure 4-20 TLI flip-flop transient response to a step input from -7.8 dBm to a) –7.7 dBm, b) –7.6 dBm, c) –5 dBm and d) +5 dBm.

power is -7.76 dBm. It is clear that the effects of critical slowing down are significant when the input switching power remains close to the critical point.

In Figure 4-20, the simulated feedback delay was 1 ns, comparable to the response time of the SOAs. In Figure 4-21, the effect of a longer feedback delay is considered. An input unit step function from –7.8 dBm to –5 dBm is applied to the flip-flop with feedback delays of 1 ns and 25 ns. For the longer delay time,

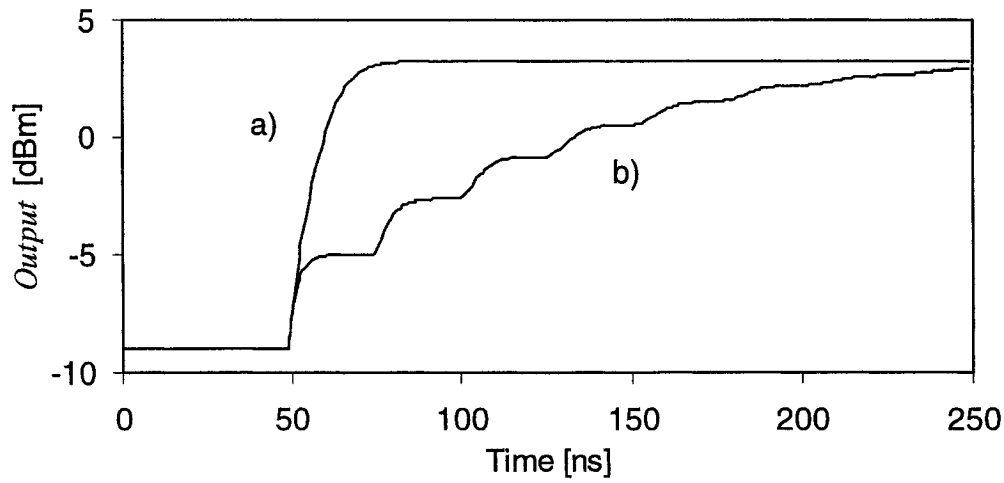

Figure 4-21 The observed transient behavior for a feedback delay of a) 1 ns and b) 25 ns.

the result is a stepped output, as the flip-flop responds to a new feedback power for each pass of the feedback loop. The transients of the SOAs are observed at each step-to-step transition, and the overall shape of the curve is controlled by the CSD and the shape of the MZI transfer function. This stepped output behavior is demonstrated experimentally in the next chapter.

This particular bistable behavior of the flip-flop is quite interesting because the properties of the MZI can be studied with or without feedback. Insight into the behavior of the flip-flop is gained when the feedback is considered separate from the MZI. As an example, certain aspects of the dynamics of critical slowing down can be studied using the static transfer function of the MZI, under special conditions. The first condition is that the dynamics of the SOAs themselves are neglected, and the second condition is that the input light into the MZI is through either the *Three-Level* input or the feedback loop but not both. As it will be shown in the following discussion, this can lead to better understanding of the operation of the entire flip-flop.

As an example, imagine that instead of a step input, a pulse is applied to the *TL* input of the flip-flop. Also assume that the pulse is just long enough in duration that it ends just as the feedback optical power reaches the waveguide coupler. In this way the second condition, described above, is satisfied. This feedback light is now the only input to the MZI, so the static transfer function of the MZI without feedback, shown in Figure 4-22, can be used to determine what the new output power will be. Care must be taken to account for gain in the feedback loop, and the losses due to the *Output* splitter and the *Three-Level Input* coupler. As the light completes a second pass of the feedback loop, it becomes the next input to the MZI. In this way the output of the flip-flop can be approximated for each cycle of the light travelling through the feedback loop.

Thus there are three contributing factors that shape a transient in this flip-flop. They are the transient behavior of the SOAs themselves, the contribution of critical slowing down, and the feedback delay time. Further, for a given input

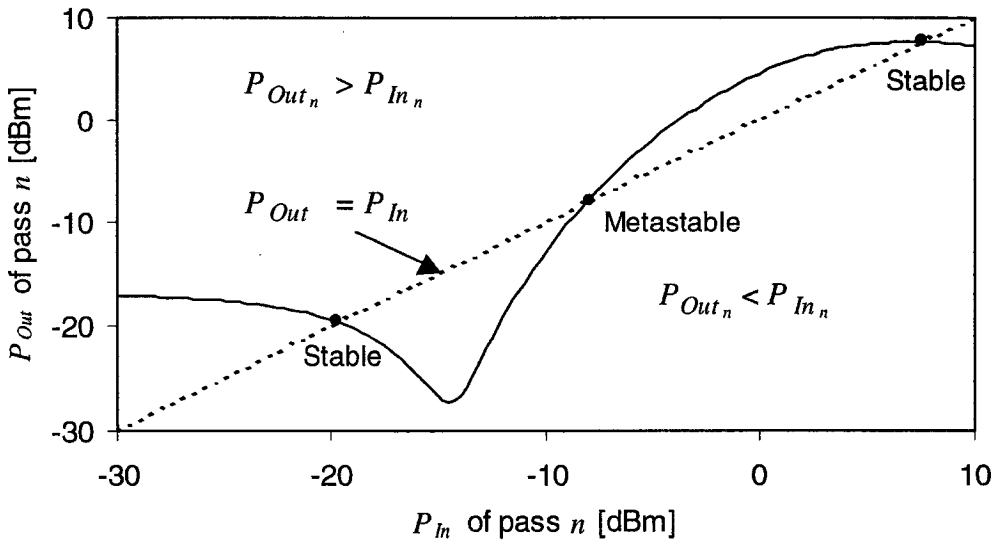

Figure 4-22 Transfer function of a noninverting MZI, along with the reference line $P_{In} = P_{Out}$.

switching pulse power, the contribution of critical slowing down is determined by the shape of the MZI transfer function. These are important results that lead to a better understanding of the flip-flop.

Next consider the static MZI transfer function shown in Figure 4-22. In this case the P_{In} and P_{Out} are both measured at an imaginary break in the feedback loop, labeled as the test point in Figure 4-17. In this way the P_{In} of pass n is identical to P_{Out} of pass n-1. The *Output* power of the device is simply P_{Out} minus the feedback gain. A reference line has been added to the transfer function to denote $P_{In} = P_{Out}$. The intersection points of the reference line and the curve represent stable or metastable points of operation, because the P_{In} of pass n results in an identical value of P_{Out} for pass $n+1$, and thus an identical value of P_{In} for pass $n+1$.

The behavior of the flip-flop near one of these operating points can be studied with a very simple linear approximation, shown in a diagram in Figure 4-23. Consider a portion of the transfer function around an intersection between the transfer function and the line $P_{In} = P_{Out}$. A Taylor series expansion can be used to

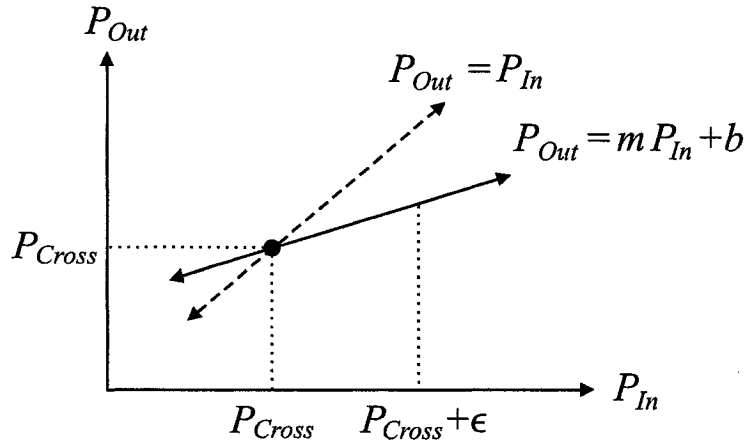

Figure 4-23 Analysis of an intersection point.

describe the transfer function about the intersection point. For simplicity, a linear approximation is assumed and thus the transfer function is described as

$$P_{Out} = m P_{In} + b, \tag{4.21}$$

where m is the slope of the transfer function and b is an offset. If the intersection point is designated as P_{Cross}, then it occurs at a power of

$$P_{Cross} = \frac{b}{1-m}. \tag{4.22}$$

Assuming an initial input close to the intersection point such that $P_{In} = P_{Cross} + \varepsilon$, the output after the first pass of the feedback loop is

$$P_{Out} = m(P_{Cross} + \varepsilon) + (1-m) P_{Cross} = P_{Cross} + m\varepsilon \tag{4.23}$$

and the output after the nth pass of the feedback loop is

$$P_{Out_n} = P_{Cross} + m^n \varepsilon. \tag{4.24}$$

Using this result we can make some useful conclusions about the behavior of the flip-flop, simply by considering the slope of the MZI transfer function. For $-1 < m < 1$, the value of P_{Out} will approach that of P_{Cross} over successive passes of

the feedback loop. Further, if m is positive the approach will be from one side of P_{Cross} only, while for negative values of m, the optical power in the feedback loop for successive passes will take on values both larger and smaller than P_{Cross}. These cases are analogous to overdamped and underdamped behavior, respectively. If $|m|>1$, the optical power in the feedback loop will diverge from that of P_{Cross} on successive passes. The value of m will determine how quickly the powers will converge or diverge from P_{Cross}. Small values of m will result in quick convergence, and large values of m will result in quick divergence. The conclusion that can be drawn from this analysis is that the shape of the MZI transfer function, which determines the values of m around the intersection points, is an important factor in the transient response of the flip-flop.

This simple analysis is very useful. As detailed above, it can be used to gain some insight into the transient behavior of the flip-flop. However, it can also be used to study a series of MZIs, with gain and/or loss elements between them. These MZIs might be used as regenerators, wavelength converters, or logic gates. The analysis was applied to the problem of a series of regenerators by [NUTT03]. It could also be used to study the noise redistribution properties of wavelength converters and regenerators [WOLF98].

Referring back to Figure 4-23, the transfer function has three intersection points. The outer two are points of convergence and are thus stable. On the other hand, the middle one, with a slope of 2.2, is a point of divergence and will be described as metastable. In practice this point of operation could not be maintained due to noise in the system. It acts as a logical threshold.

Returning now to the discussion of critical slowing down, operation close to the metastable point results in a small value of ε. Using equation (4.24), with $m=2.2$ and a small ε, it is clear that it will take many passes of the feedback loop to diverge from this point, slowing the transient response considerably. To avoid the problem, ε must be made large. When setting the flip-flop this can be accomplished using an intense pulse as demonstrated in Figure 4-19.

Unfortunately, the same is not true when resetting the flip-flop. The problem is that even if the *TL* input is eliminated completely, there is still considerable power in the feedback loop. This power could be minimized by reducing the feedback gain, but that has the effect of decreasing the width of the bistability, making the flip-flop more susceptible to noise induced switching. This critical slowing down associated with the turn-off transient is shown in Figure 4-24.

The previous analysis of points of convergence leads to an interesting alternative to resetting the flip-flop. Referring to Figure 4-22, a reduction in the feedback gain has the simple effect of moving the transfer function down with respect to the reference line. This changes the position of the various intersection points. If the gain is reduced sufficiently, it is possible to have only one intersection point located in the lower part of the transfer function. Thus, the operating point of the flip-flop is forced to converge that point. This reduction in feedback gain is easily achieved through XGM in an SOA, or XPM in a MZI. In the next subsection, such a flip-flop is proposed. Note also that with a sufficient

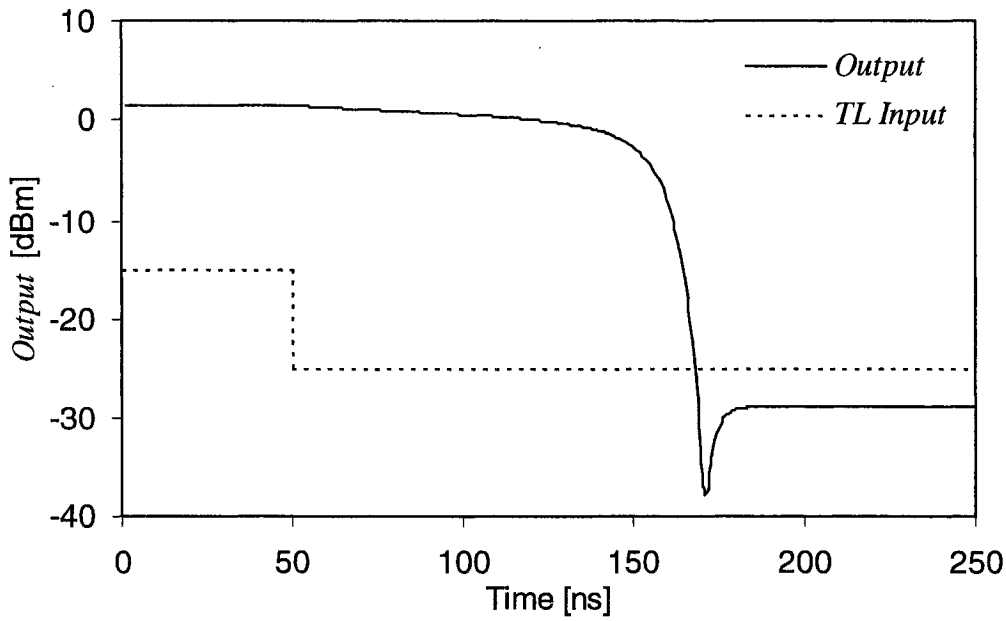

Figure 4-24 Critical slowing down associated with the turn-off transient of the TLI flip-flop.

increase in feedback gain, the flip-flop can be forced to operate at a single intersection point in the upper part of the transfer function, but this is not considered further in this thesis.

4.3.4 Simulation of the Proposed Flip-Flop

From the patented flip-flop design, it was discovered that for proper operation, it was important for the *Reset* to have a direct impact on the optical power circulating in the feedback loop. The three-level-input design accomplishes this but suffers from unavoidable critical slowing down associated with the turn-off transient. To solve that problem it becomes necessary to extinguish the light in the feedback loop, in addition to the input. The design shown in Figure 4-25 was developed to satisfy both of these requirements. It is a major contribution of this thesis. In this section, simulations are carried out on the device to show that it behaves as desired, accomplishing the goal of an all-optical flip-flop. In the next chapter its experimental verification is described and discussed.

The newly proposed flip-flop once again uses binary *Set* and *Reset* signals, simplifying the design. Also, as in the patented design, a relatively large feedback gain is used, but in this case the *Reset* modulates the feedback gain

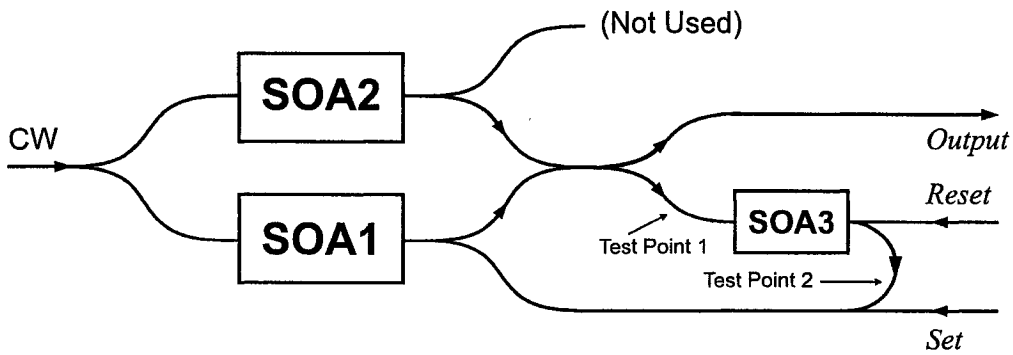

Figure 4-25 Schematic of the newly proposed flip-flop. The feedback SOA (SOA3) operates via cross-gain modulation. The *Set* and *Reset* inputs are binary. The upper output arm of the MZI is not used but is shown because it is present in commercial MZI chips.

through cross-gain modulation in a feedback SOA. Another possible design would replace the single feedback SOA with a second MZI, allowing the *Reset* to control the feedback gain through XPM.

The flip-flop was designed using the same MZI as in section 4.3.2. The *Set* and *Reset* signals were each assumed to have a wavelength of 1555 nm and a duration of 52 ns, slightly longer than the loop delay of 50 ns. The low and high power levels were –25 dBm and +5 dBm, respectively, for the *Set*, and –22 dBm and +8 dBm, respectively, for the *Reset*. In this way two identical input signals could be used to control the flip-flop, by incorporating a simple 3 dB loss element in the path of the *Set*.

An overall feedback power gain of 2 dB (equivalent to 1.6 in the linear scale) was used in the simulations. It is desirable to use a larger SOA gain, however, so that the XGM can produce a larger extinction ratio in the modulated feedback power. The simulations include lumped losses both before and after the feedback SOA to reduce the overall gain to 2 dB. To select the losses, the power before the SOA (Test Point 1) was found to be 3 dBm when the flip-flop was in a steady on-state. After the losses and gains, a power of 3 dBm + 2 dB = 5 dBm is expected at Test Point 2. For efficient XGM, it was desirable to select the operating point of the feedback SOA so that it was just slightly saturated, in this case at -14 dBm. The loss before the SOA was then calculated to be 3 dBm – (-14) dBm = 17 dB. With an injection current of 100 mA, the feedback SOA provided a gain of 25.4 dB so the output power of the SOA was -14 dBm + 25.4 dB = 11.4 dBm. The loss after the SOA was then calculated to be 11.4 dBm – 5 dBm = 6.4 dB. In a real system these losses could be included into the waveguide splitters and couplers by making them asymmetric, or included as electrically tunable optical absorption sections. The static transfer functions of the proposed flip-flop are shown in Figure 4-26 and Figure 4-27, with respect to the applied *Set* power and *Reset* power, respectively. The function shown in Figure 4-26 is somewhat different

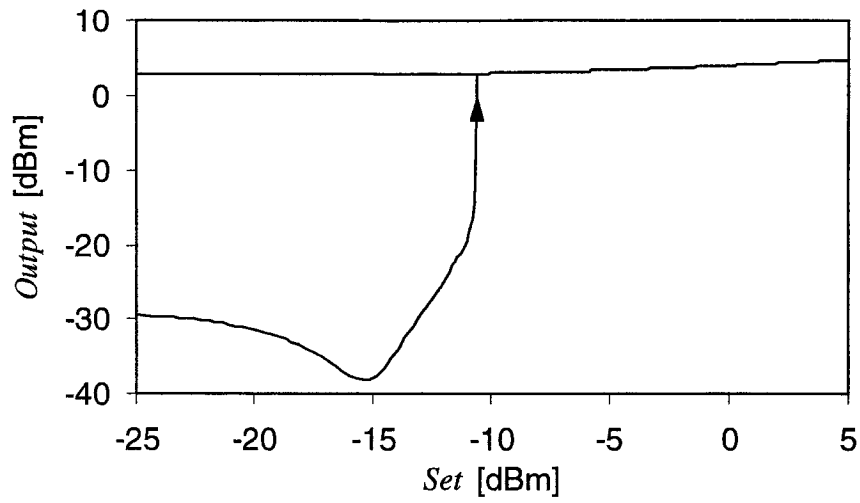

Figure 4-26 Static transfer function of the proposed flip-flop, with respect to the *Set* power.

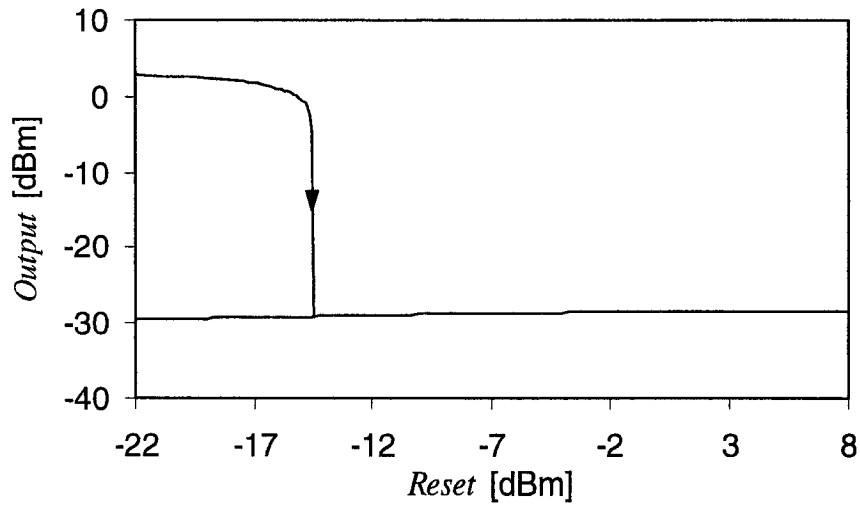

Figure 4-27 Static transfer function of the proposed flip-flop, with respect to the *Reset* power.

than the transfer function shown in Figure 4-12. This is because the linear gain has been replaced by an SOA with nonlinear, saturable gain. When operating in the upper bistable section of the transfer function, the gain of the feedback loop

is designed to be 1.6 and the gain of the feedback SOA is only slightly saturated. Smaller optical powers passing through the feedback loop will see somewhat higher gains, as the SOA is unsaturated. Thus the turn-on threshold power is lower than in Figure 4-12. Figure 4-26 is calculated with *Reset* = -22 dBm, and Figure 4-27 is calculated with *Set* = -25 dBm. Thus, the extreme left of each graph represents the same bistable operating point.

The dynamic response of the flip-flop is shown in Figure 4-28, where it is successfully set and reset. A time-step of 0.1 ns was used in this simulation and in the remainder of this section. The feedback delay is lumped after the feedback SOA, thus the *Output* responds immediately to the *Set* while a full loop delay of 50 ns occurs before it responds to the *Reset*. The dip in the plot at about 265 ns is due to the dip in the transfer function. It is not a problem because it does not adversely affect the extinction ratio of the signal.

The primary motivation for this flip-flop design was to make it tolerable to *Reset* pulse durations longer than the loop delay, as well as multiple *Reset* pulses in series. Sensitivity of the flip-flop *Output* to changes in the *Reset* duration is shown in Figure 4-29. As with the patented design, the *Reset* must have a

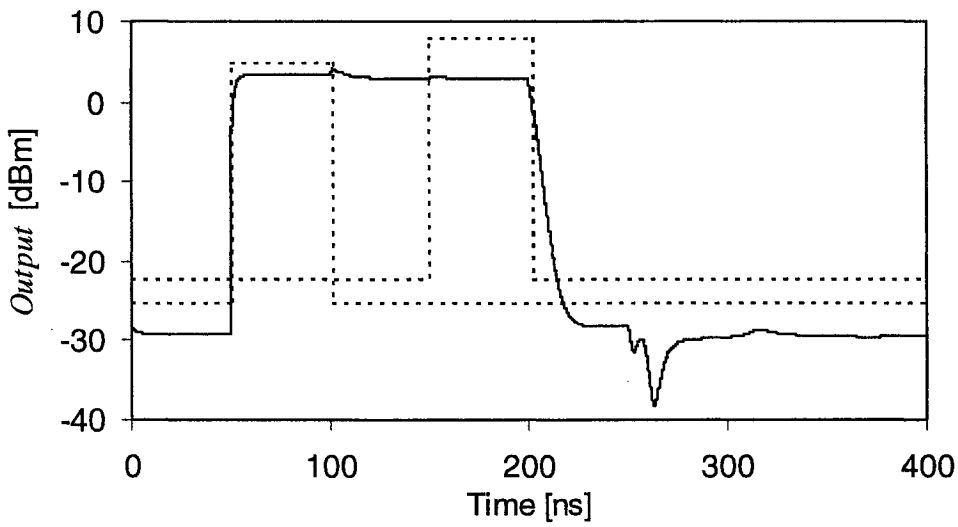

Figure 4-28 Dynamic response (solid curve) of the proposed flip-flop to *Set* and *Reset* pulses (dotted curves).

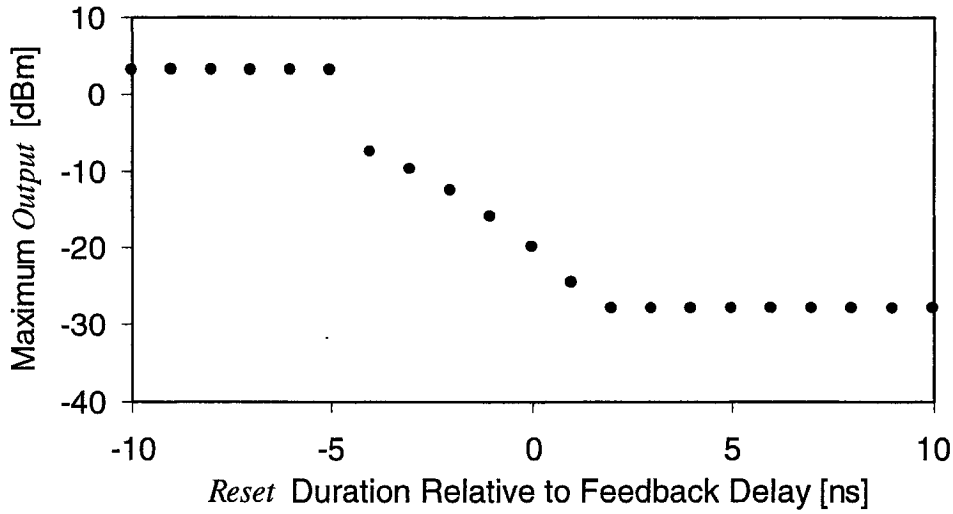

Figure 4-29 Sensitivity of the *Output* power of the flip-flop to changes in the duration of the *Reset*, relative to the feedback delay.

minimum duration in order to reduce the light intensity throughout the feedback loop. Now, however, the *Reset* may be longer in duration without the generation of unwanted oscillations. The design succeeds in its goal.

To further demonstrate the operation of the proposed flip-flop, Figure 4-30 shows the response to a *Reset* pulse when the flip-flop has previously been reset. The flip-flop operates properly.

For further insight into the operation of the flip-flop, the sensitivity to other input parameters was examined. In Figure 4-31, the power of each input power level is modified. To quantify the effect on the flip-flop, either the minimum *Output* power while in the on-state, or the maximum *Output* power while in the off-state was recorded, depending on which would be adversely affected. These maxima and mimina were recorded starting 26 ns after the beginning of a *Set* pulse and 76 ns after the beginning of the *Reset*. In this way the transients of the SOAs in the MZI and the loop delay did not affect the recorded values. For the variations in the input power levels, emphasis was paid to inputs with lower extinction ratios than in the previous simulations. The on-states of each input had the most

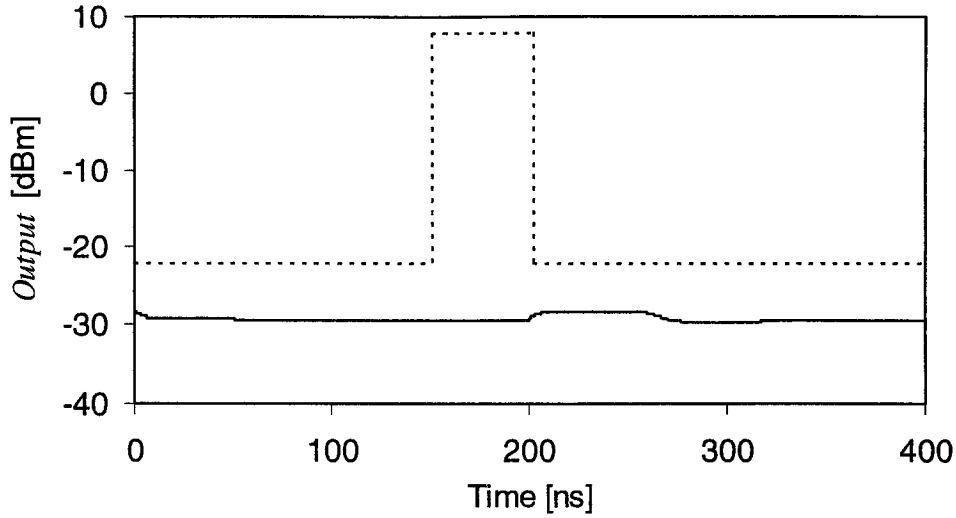

Figure 4-30 Response (solid curve) of the flip-flop to a *Reset* pulse (dotted curve), while already in the off state, demonstrating successful operation.

impact on the degradation of the output extinction ratio. This was due to critical slowing down, although much less extreme than discussed in the previous section. In each case the *Output* settled to its steady state value in only a few passes of the feedback loop.

Ideally, the flip-flop should also be tolerant to changes in the input wavelength. The sensitivity to *Set* and *Reset* wavelength is shown in Figure 4-32. Simulations were performed for wavelengths 20 nm shorter and longer than the design wavelength. The flip-flop worked properly over the entire range, and showed no signs of degradation at the long wavelength end of the range. At the short wavelength end of the range, the largest impact is due to the *Reset*. This result is identical to the case of wavelength converting from a short wavelength to a longer one which is known to reduce the efficiency of the wavelength conversion. This is because as the SOA is saturated (Figure 4-3), the peak gain moves to longer wavelengths, reducing the gain experienced by the modulating signal.

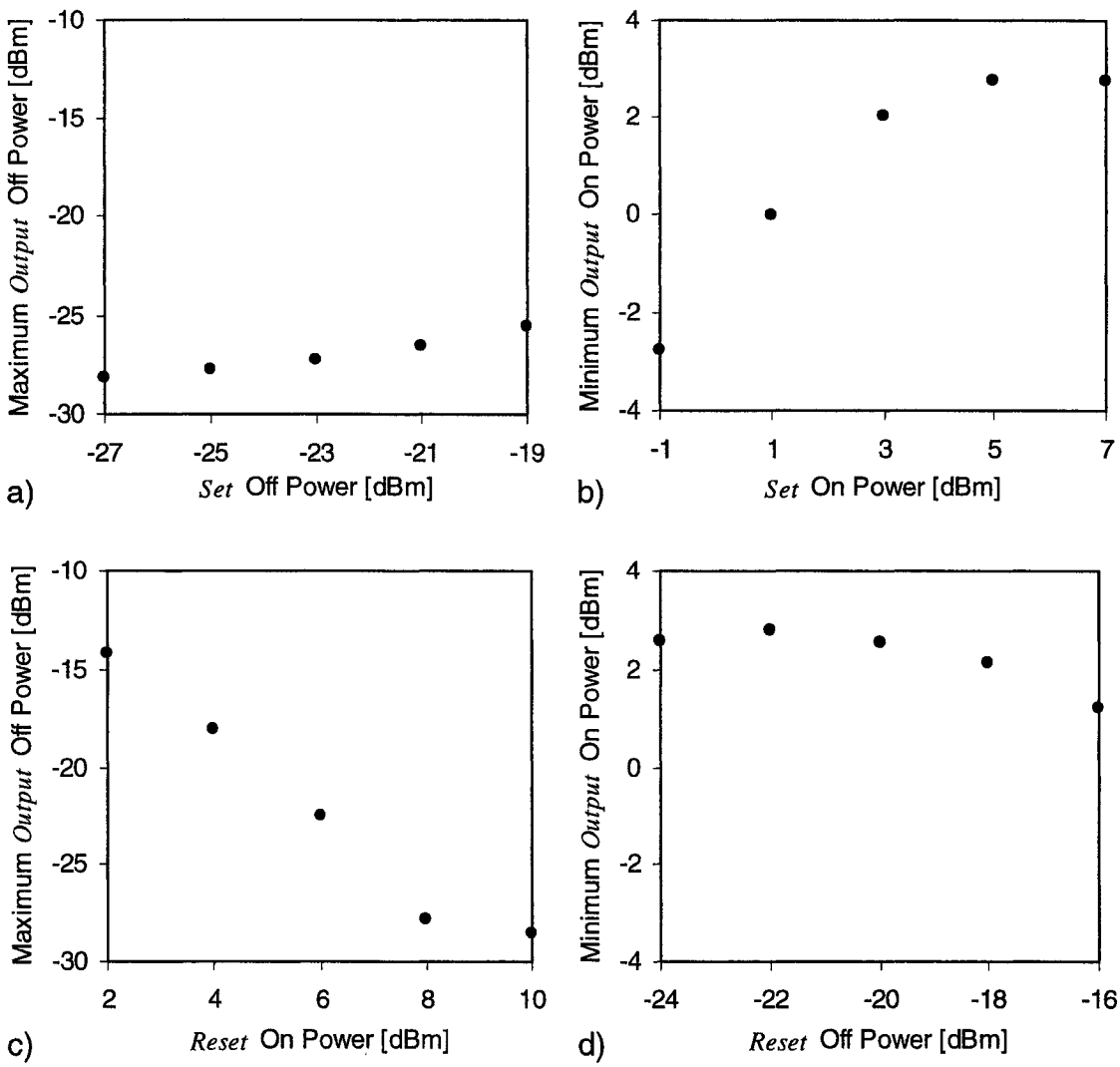

Figure 4-31 Sensitivity of the *Output* power of the flip-flop to changes in a) *Set* off power, b) *Set* on power, c) *Reset* on power, and d) *Reset* off power. The vertical scales of the graphs in each column have been matched for comparison purposes.

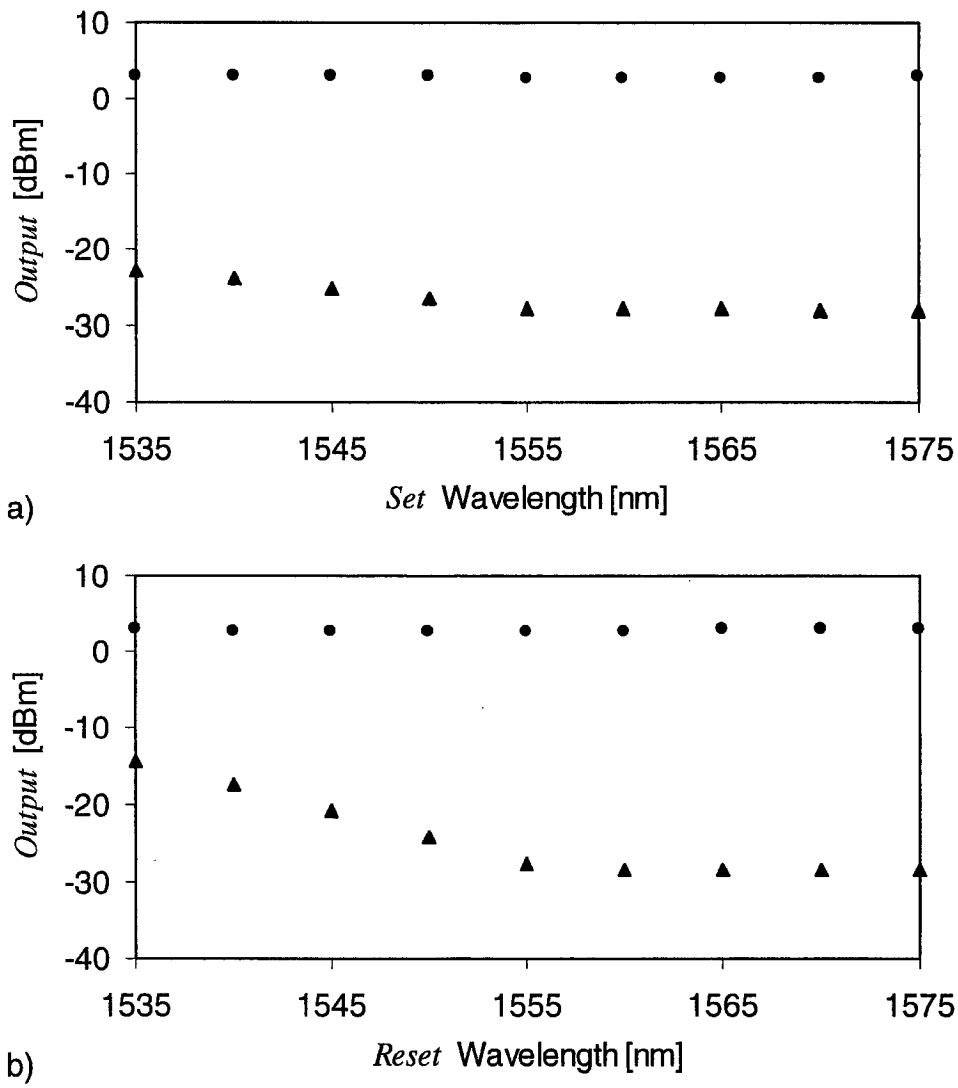

Figure 4-32 Sensitivity of the *Output* power of the flip-flop to changes in a) *Set* wavelength and b) *Reset* wavelength. Circles represent minimum *Output* on-powers and triangles represent maximum *Output* off-powers.

4.3.5 Optical Ring Oscillator

Up to this point, the MZI was operated with a non-inverting transfer function. However, the application of feedback to an inverting MZI is also interesting. In this case, the result is an optical ring oscillator, the equivalent of an electronic ring oscillator that is often built in introductory electronics classes. As in the electronic version, the device is self-starting, and produces a square wave when the transients of the gates are short compared to the fundamental frequency of the oscillator. The fundamental frequency is controlled by the feedback delay. The output produces a square wave because of the regenerative properties of the oscillator. The output power of every alternate half cycle converges to an operating point that can be determined from the transfer function of the MZI.

For the analysis, consider again an imaginary break in the feedback loop, this time immediately before the feedback gain. A power P_{In1} will be inverted after the first pass and returned to the original value after the second pass, designated P_{Out2}. Graphically, the operating points can be found by mirroring the transfer function about the reference line $P_{In} = P_{Out}$, and looking for intersection points as shown in Figure 4-33.

As with the TLI flip-flop, a Taylor series expansion of the transfer function about each of the intersection points is performed. Using a linear approximation, the powers in the feedback loop after the first and second passes are described by, respectively

$$P_{Out1} = m_1 P_{In1} + b_1 \quad \text{and} \quad P_{Out2} = m_2 P_{In2} + b_2 . \tag{4.25}$$

The output of the first pass of the feedback loop is the input to the second pass, which can be expressed as $P_{Out1} = P_{In2}$. Also, given the paired nature of the intersection points, $P_{Out2} = P_{In1}$. Using these equalities, (4.25) can be solved to

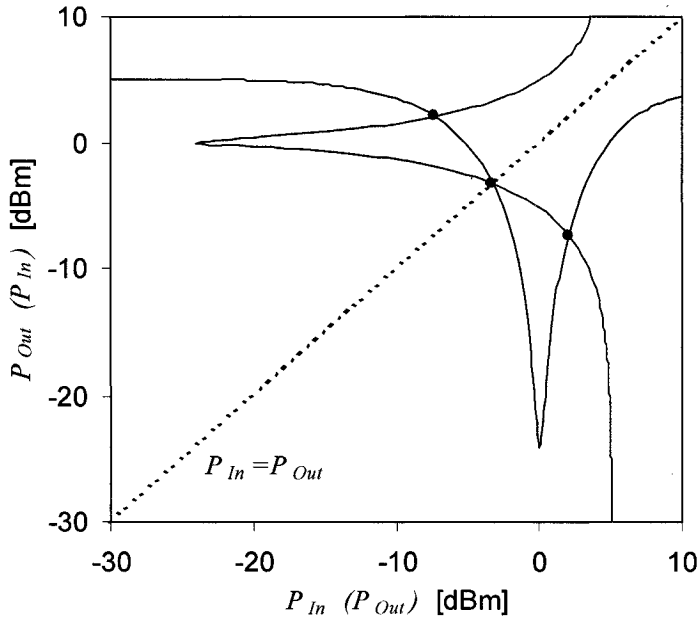

Figure 4-33 An inverting transfer function mirrored about the line $P_{In} = P_{Out}$ to find the operating points.

find one of the intersection points. Solving yields

$$P_{Cross} = \frac{m_2 b_1 + b_2}{1 - m_1 m_2}, \tag{4.26}$$

where the calculated power is the input power for an odd numbered pass of the loop. We can now consider an input value close to the intersection point such that

$$P_{In1} = P_{Cross} + \varepsilon . \tag{4.27}$$

Solving (4.25) and (4.27), the output after the second pass of the feedback loop is found to be

$$P_{Out2} = \frac{m_2 b_1 + b_2}{1 - m_1 m_2} + m_1 m_2 \varepsilon = P_{Cross} + m_1 m_2 \varepsilon . \tag{4.28}$$

The output after n (n even) passes of the feedback loop is

$$P_{Outn} = P_{Cross} + (m_1 m_2)^n \varepsilon . \tag{4.29}$$

Thus, if $0 < |m_1 m_2| < 1$ the outputs of successive passes of the feedback loop will settle to the intersection point. If $|m_1 m_2| > 1$ those outputs will diverge from the intersection point. If $|m_1 m_2| = 1$ the outputs will alternate around the intersection point on successive even (and odd) numbered passes.

As in the noninverting case, the position of the intersection points can be controlled by adjusting the feedback gain. An oscillator was simulated for various values of feedback gain, G_{fb}. For every value of G_{fb} the intersection points were calculated. From the intersection points, the extinction ratio of the *Output* oscillation was calculated using $P_{Out2} - P_{Out1}$ and is shown in Figure 4-34. Note that P_{Out} is equivalent to the *Output*, because the output splitter is assumed to have a 50:50 splitting ratio. The maximum *Output* extinction ratio is obtained for $G_{fb} = 1.7$, which occurs when one of the intersection points is at the bottom of the dip in the transfer function.

The product $m1 \cdot m2$ was also calculated to determine the stability of each pair of intersection points. The resulting graph is shown in Figure 4-35. For $G_{fb} < 2.2$ (equivalent to 3.4 dB), the product is less than one indicating that optical power levels within the feedback loop will converge to the intersection points. Thus the intersection points are stable. For $G_{fb} > 3.4\,\text{dB}$, starting optical power levels near the intersection points will diverge from those points; thus the intersection points are metastable.

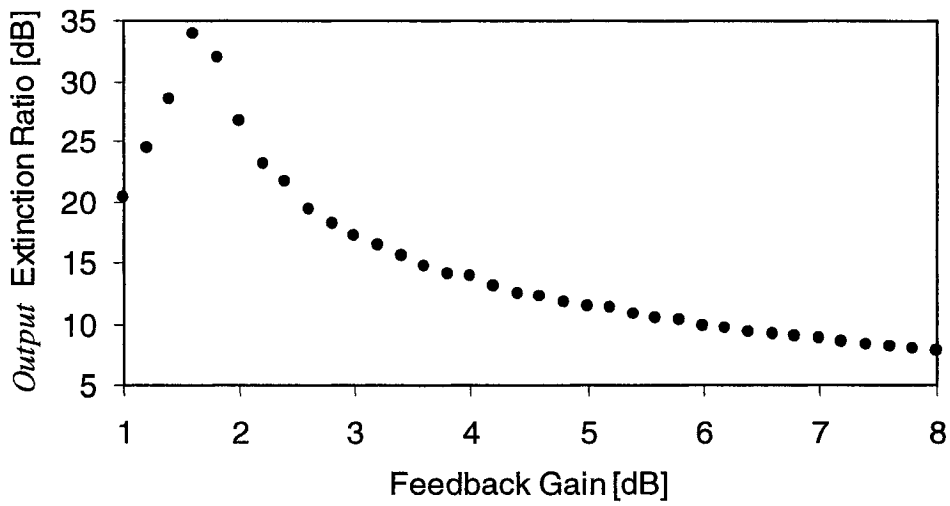

Figure 4-34 The oscillator *Output* extinction ratio as a function of feedback gain, G_{fb}.

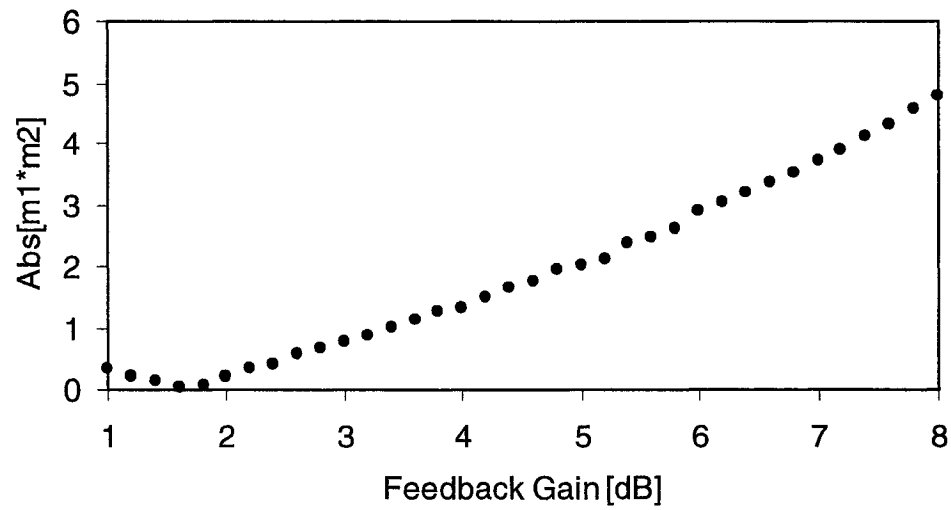

Figure 4-35 Product of the slopes of the oscillator transfer function at each intersection point, as a function of feedback gain. Product values less than one indicate that the intersection points represent stable operating points.

A simulation of an oscillator with stable intersection points was performed. A feedback gain of $G_{fb} = 1.14$ dB was used, which produces two intersection points at $P_{Out} = -20.2$ dBm and $P_{Out} = +1.3$ dBm as shown in Figure 4-36. The initial condition was $P_{In} = -6.14$ dBm, which is far from either of the intersection points. The feedback delay was 100 ns. The results of the dynamic simulation are shown in Figure 4-37. The oscillator is self-starting and the *Output* converges to the power levels indicated by the intersection points.

A simulation of an oscillator with metastable intersection points was also performed. A feedback gain of $G_{fb} = 4.8$ dB was used, which produces two intersection points at $P_{Out} = -11.657$ dBm and $P_{Out} = -0.01$ dBm as shown in Figure 4-38. The initial condition was $P_{In} = 0$ dBm, very close to one of the intersection points, and the feedback delay was 100 ns. The results of the dynamic simulation are shown in Figure 4-39. The strong dips in the *Output* power are due to the dip in the transfer function. The finite response time of the MZI causes the *Output* to follow the transfer function continuously, including the dip. Even if the transient response of the MZI is neglected, the *Output* power levels of successive passes of the feedback loop are complex in the sense that they show no discernable pattern. Simulations with small changes to the initial condition give quite different results, indicating that in this case the oscillator is chaotic.

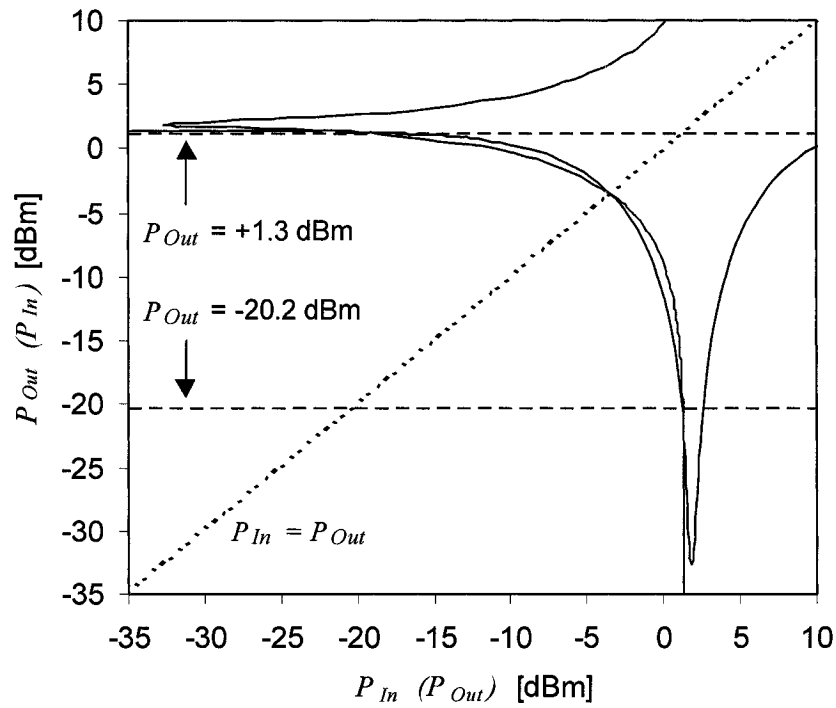

Figure 4-36 An inverting transfer function mirrored about the line $P_{In} = P_{Out}$, representing an oscillator with $G_{fb} = 1.14$ dB.

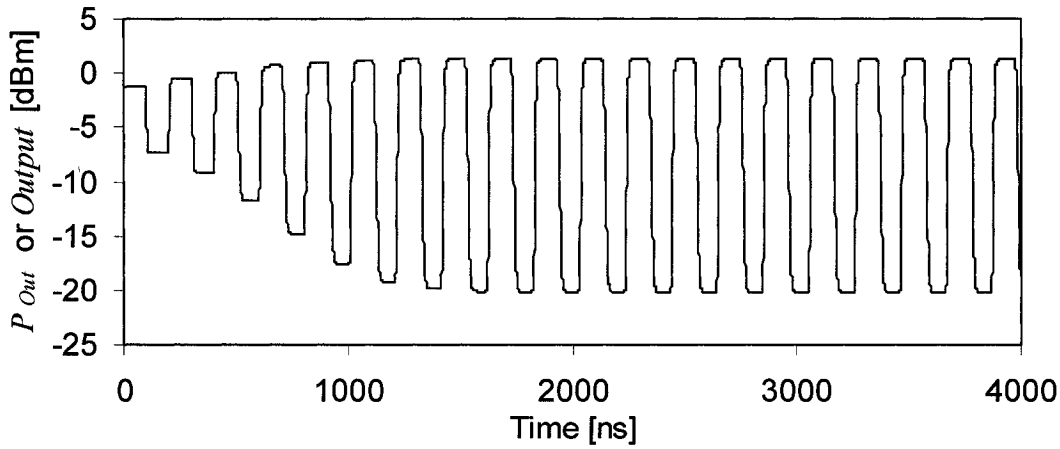

Figure 4-37 Dynamic simulation of an oscillator. The feedback gain was 1.14 dB. The resulting intersection points were stable, and the convergence of the *Output* power levels to the intersection values is clearly visible.

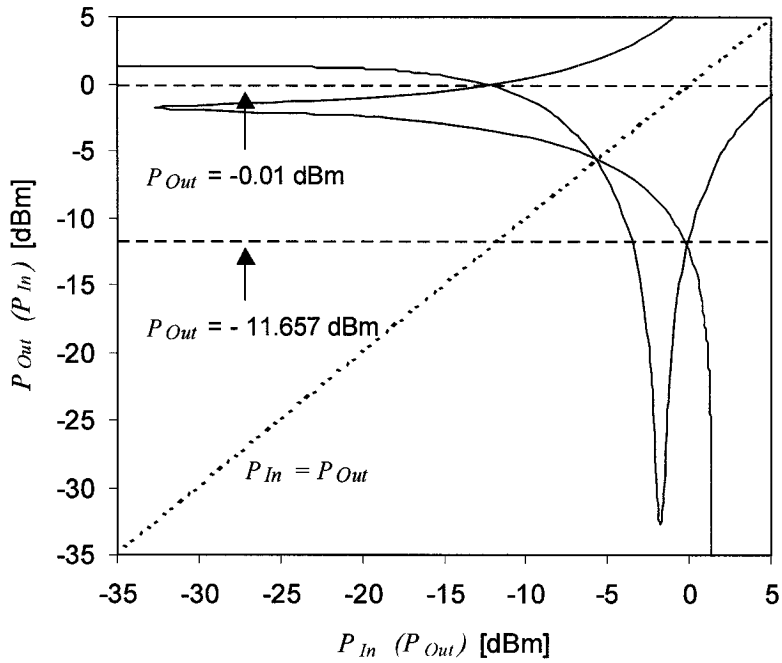

Figure 4-38 An inverting transfer function mirrored about the line $P_{In} = P_{Out}$, representing an oscillator with G_{fb} = 4.8 dB.

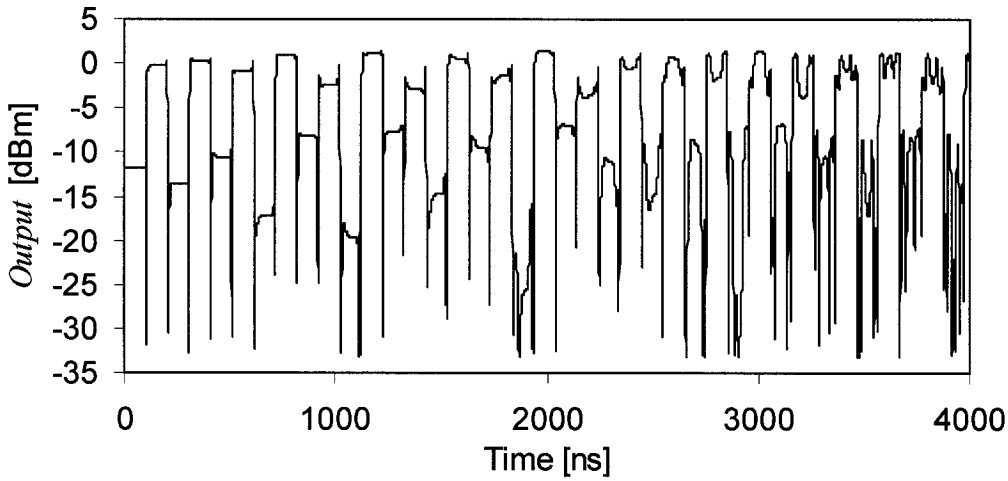

Figure 4-39 Dynamic simulation of an oscillator with a feedback gain of 4.8 dB. The initial power level in the feedback loop was 0 dBm, close to the intersection point of –0.01 dBm. The large feedback gain makes the intersection points metastable only. Divergence from the metastable intersection point causes the *Output* to become chaotic.

4.4 SUMMARY

A model of an SOA was developed based on a rate equation and a travelling wave equation. The model was then expanded to simulate XPM in an MZI-SOA. Using the model, the effects of feedback on both inverting and non-inverting MZIs were examined, for the purpose of developing optical signal processing capabilities.

A patented flip-flop design was simulated. It was shown that the design works properly when set, but when reset, an oscillating output signal can result. It was necessary to match the duration of the *Reset* pulse to the feedback loop delay to minimize the effect of the oscillations. In practical situations this may not be possible. In addition, it was shown that a *Reset* pulse that arrives while the flip-flop is already reset causes the device to be set. These limitations make the design impractical.

A second design was then considered, which used an entire hysteresis loop and a three-power-level input signal. The oscillation problem was avoided, however the design suffered from critical slowing down, because the light in the feedback loop could not be quickly reduced.

Using XGM, a third flip-flop design was proposed as a way to control the light level in the feedback loop. Cross-gain modulation was performed in an SOA that provided the gain to the feedback loop. This flip-flop was shown to work properly by avoiding the oscillation problem of the first design, and the critical slowing down of the second design. It was shown to be relatively insensitive to input pulse duration and power when compared to the patented design.

A simple linear analysis of transfer functions was used to attain a better understanding of these flip-flops. It was used to explain some of the behavior associated with the critical slowing down. It was also used to explain how the proposed flip-flop design operates.

Finally the effect of feedback on an inverting MZI was investigated. Ring oscillator behavior was observed. Again, the transfer function analysis was applied to gain insight into optimizing the oscillator. In this way a condition for stable oscillator output was obtained. It was demonstrated that when the condition is not met, the output is chaotic.

CHAPTER

5

EXPERIMENTAL RESULTS

This chapter presents the experimental verification of many of the ideas discussed in the previous chapter. The work was carried out at Queen's University, Kingston, Ontario, in the laboratory of Dr. J. Cartledge, in January and February of 2004. An integrated MZI-SOA from Alcatel was used to build the proposed flip-flop design. The static and dynamic properties of the flip-flop were investigated in detail. The same hardware design was then used as a buffer-type memory with full read/write capability. Finally, results were obtained of an optical ring oscillator.

5.1 INTRODUCTION

5.1.1 Alcatel Wavelength Converter

The primary piece of equipment around which all of the experiments were based was the Alcatel All Optical Wavelength Converter. This is an integrated Mach-Zehnder interferometer with active waveguides. A diagram of the device is shown in Figure 5-1. The electrical contacts to the waveguides are divided into several sections with separate currents supplied to each section. In this way the carrier density, and thus the refractive index and gain, can be controlled in each

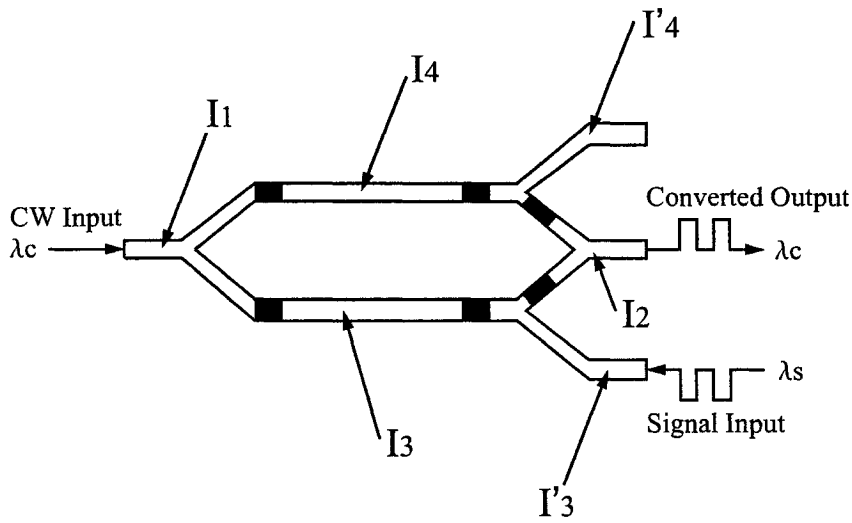

Figure 5-1 Diagram of the Alcatel All Optical Wavelength Converter showing the partitioning of the electrical contacts on the active waveguides. Redrawn from the Alcatel specification sheets.

of the arms. The whole device is temperature controlled through a single Peltier cooler. The packaged chip is pigtailed providing access to three of the waveguides. The fourth waveguide at the upper right of the drawing was not fiber coupled. This meant that some of the hardware arrangements discussed in the theory section could not be verified.

The spectrum at the output of the wavelength converter was observed on an HP 70950A optical spectrum analyzer and is shown in Figure 5-2. The large amount of spontaneous emission and amplified spontaneous emission clearly dominates the trace. The output is seen on the long wavelength side of the spontaneous emission peak. The wavelength of the CW input, which is the same as the output, is 1551.72 nm. The reference level (5.68 dBm) is represented by the second grid line from the top.

The large amount of noise can be reduced by increasing the CW input power, so that the SOAs are further saturated. However, in the case of the following experiments, the CW power cannot be varied without affecting the transfer function and thus the performance of the flip-flop. Another option to reduce ASE noise is to filter the desired output signal although it does not reduce

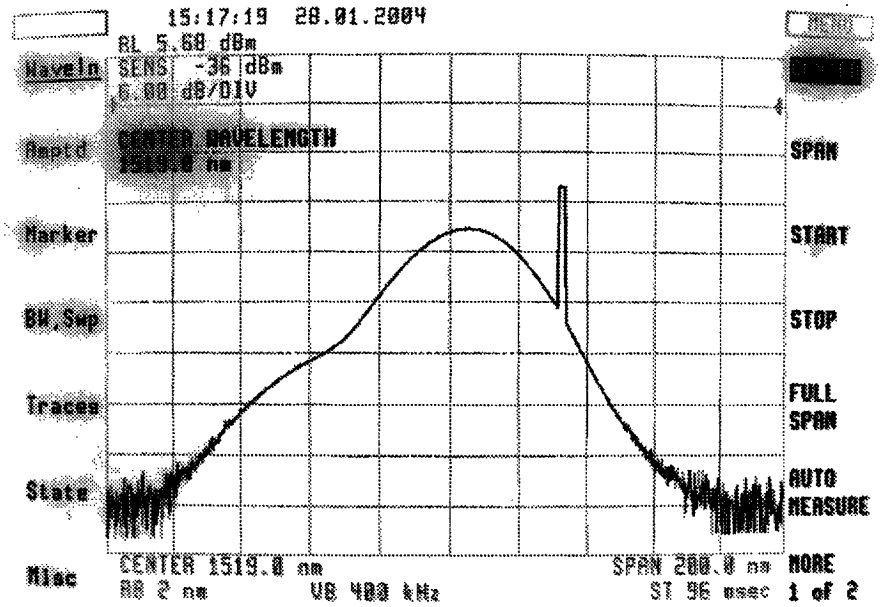

Figure 5-2 Optical spectrum at the output of the wavelength converter. The narrow peak on the right is the output at 1551.72 nm. The remainder is spontaneous emission and amplified spontaneous emission.

in-band ASE noise as would the previous technique.

There are many user controlled parameters that affect the shape of the transfer function of the wavelength converter. These include the six input currents and the CW input power. It is not intuitive how each of these affects the transfer function, and considerable time could be spent optimizing these parameters for a given application. Obtaining a suitable transfer function for the flip-flop is more challenging than that of a simple wavelength converter. In particular, it requires a noninverting function. The Alcatel wavelength converter is not optimized for this function. This is because the physical arm lengths are the same; thus to obtain a π phase shift for a low input signal power, the injection currents must be set to different values to create an effective optical path length difference. This in turn means that the gains of the arms will be different and the destructive interference at the output will not be as complete as possible.

5.1.2 Noninverting Transfer Function

Some time was spent finding a suitable transfer function for use in the flip-flop. Alcatel claims that the sections I4 and I'4 could be used for somewhat independent control of gain and phase in the upper arm, although this was found to have little useful effect. Figure 5-3 and Figure 5-4 show optical transfer functions for various values of I4 injection current. The other parameter values used to generate these curves include; I1 = 30 mA, I2 = 100 mA, I3 = 100 mA, I'3 = 50 mA, I'4 = 50 mA, T = 24° C, CW power = -5 dBm. The output of the wavelength converter was filtered with a JDS Uniphase TB1500D tunable filter to remove out-of-band spontaneous emission. The dotted line represents $P_{In} = P_{Out}$, discussed in Chapter 4, which can be used as a reference to help evaluate the suitability of each curve for use in the flip-flop. Values of 52.0 mA to 53.5 mA for I4 were found to produce the cleanest flip-flop output signal.

It should be noted that the waveguides of the wavelength converter were found to be very polarization sensitive. In the transfer functions presented, the polarizations of the optical inputs were aligned to the waveguides such that the inputs experienced a maximum gain.

5.2 ALL-OPTICAL FLIP-FLOP

A diagram of the experimental setup used for the all-optical flip-flop is shown in Figure 5-5. Hardware in the feedback loop serves several purposes. An SOA provides feedback gain, which can be reduced through gain saturation by a reset signal. Couplers provide paths for the optical inputs and outputs. Filters remove out-of-band spontaneous emission and the isolator and circulator ensure the feedback is in the clockwise direction only. To filter the output of the interferometer, a reflective fiber Bragg grating (FBG) was used. The filter

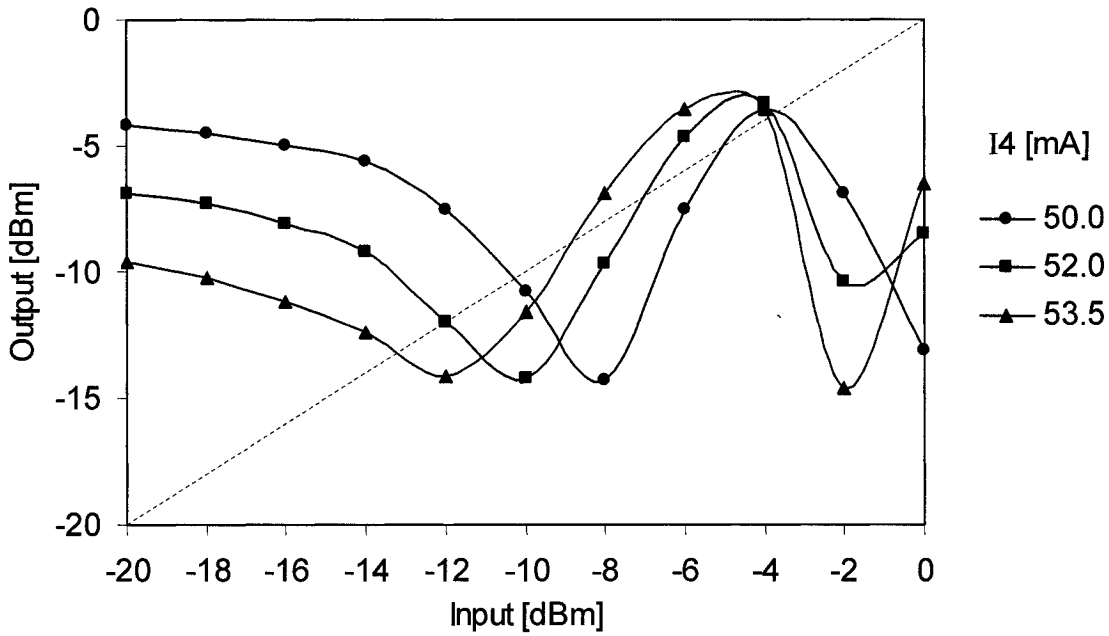

Figure 5-3 Optical transfer functions of the interferometer for various values of I4. The remaining parameter values are given in the text.

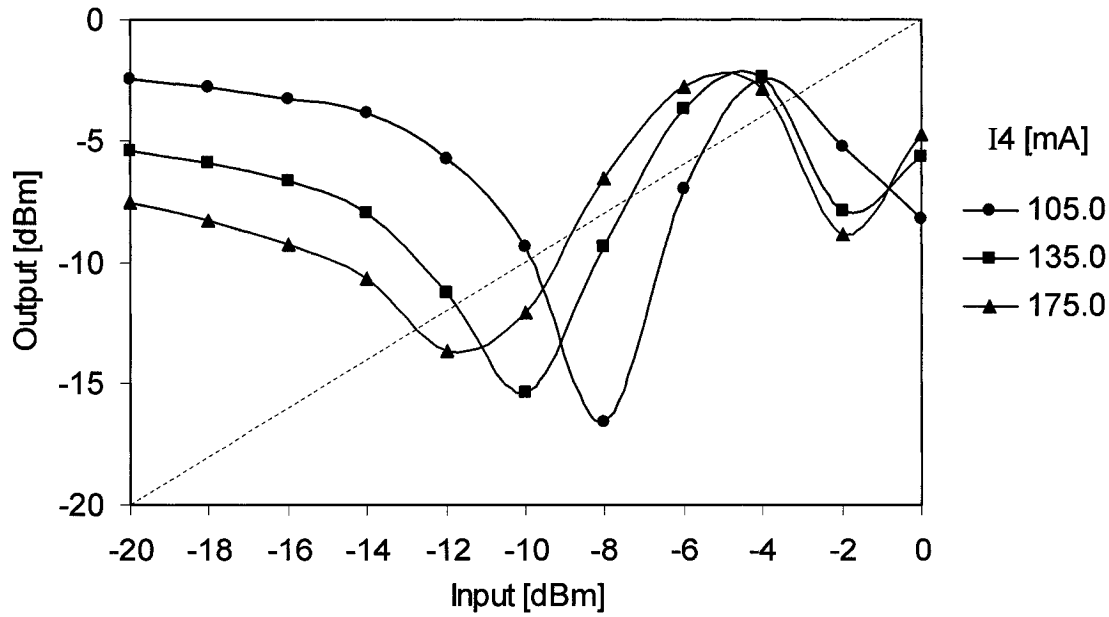

Figure 5-4 Optical transfer functions of the interferometer for various values of I4. The remaining parameter values are given in the text.

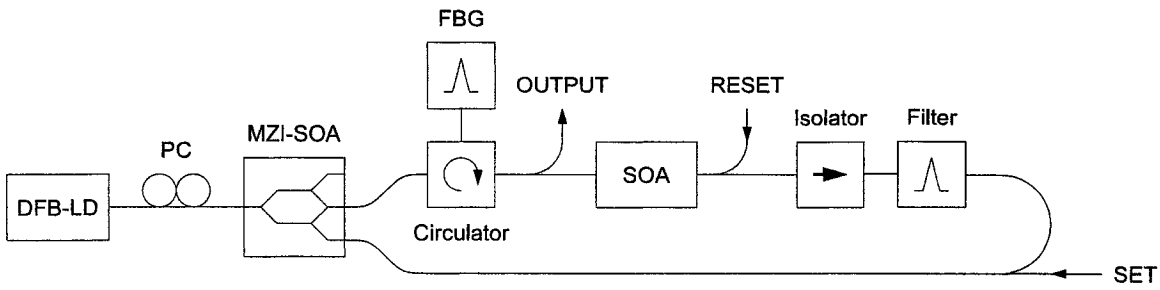

Figure 5-5 Block diagram of the experimental setup used for the flip-flop.

matched the wavelength of the CW input for the interferometer and had a narrower bandwidth (0.246 nm) than the available tunable filters. It was used in conjunction with a circulator that provided isolation (at least 55 dB per port) to the output of the interferometer. It should also be noted that port 3 was internally isolated from port 1. This prevented noise, produced by the feedback SOA, from reaching the MZI-SOA in the counterclockwise direction.

5.2.1 Static Operation

Simulations predicted that an increase in feedback gain, achieved by increasing the injection current in the feedback SOA, would increase the nonlinearity of the setup and widen the bistable section of the transfer function. This was verified experimentally with the results being shown in Figure 5-8. These curves show the output as a function of the SET input. For an SOA injection current, I_{SOA}, of 155 mA the transfer function is still single valued, though highly nonlinear. For larger currents bistability is achieved. The width of the bistability increases with increasing injection current, with the position of the downward transition of the bistability being much more sensitive to the feedback gain than the upward transition. For injection currents above 215 mA, the downward transition of the transfer function occurs at input power levels lower than the measured range. For injection currents above 235 mA, the lower bistable state is no longer

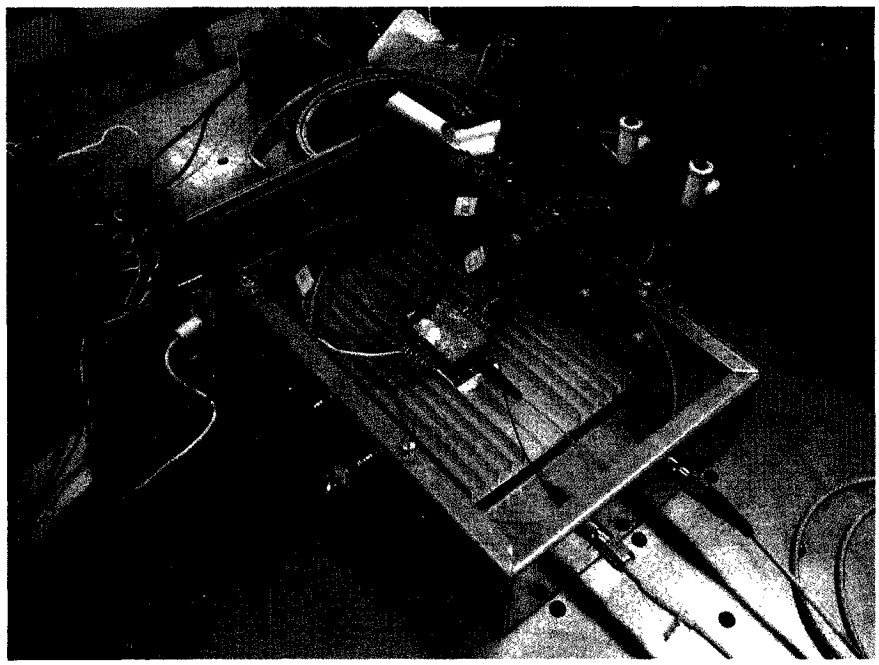

Figure 5-6 Packaged MZI housed in a protective metal box.

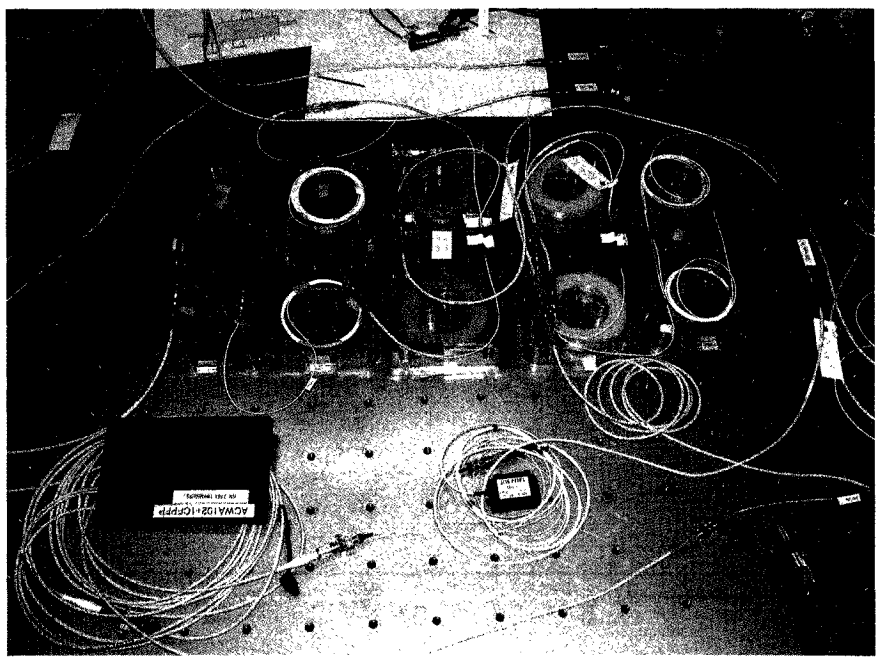

Figure 5-7 The feedback loop consisting of passive components (middle and lower) and an SOA (top).

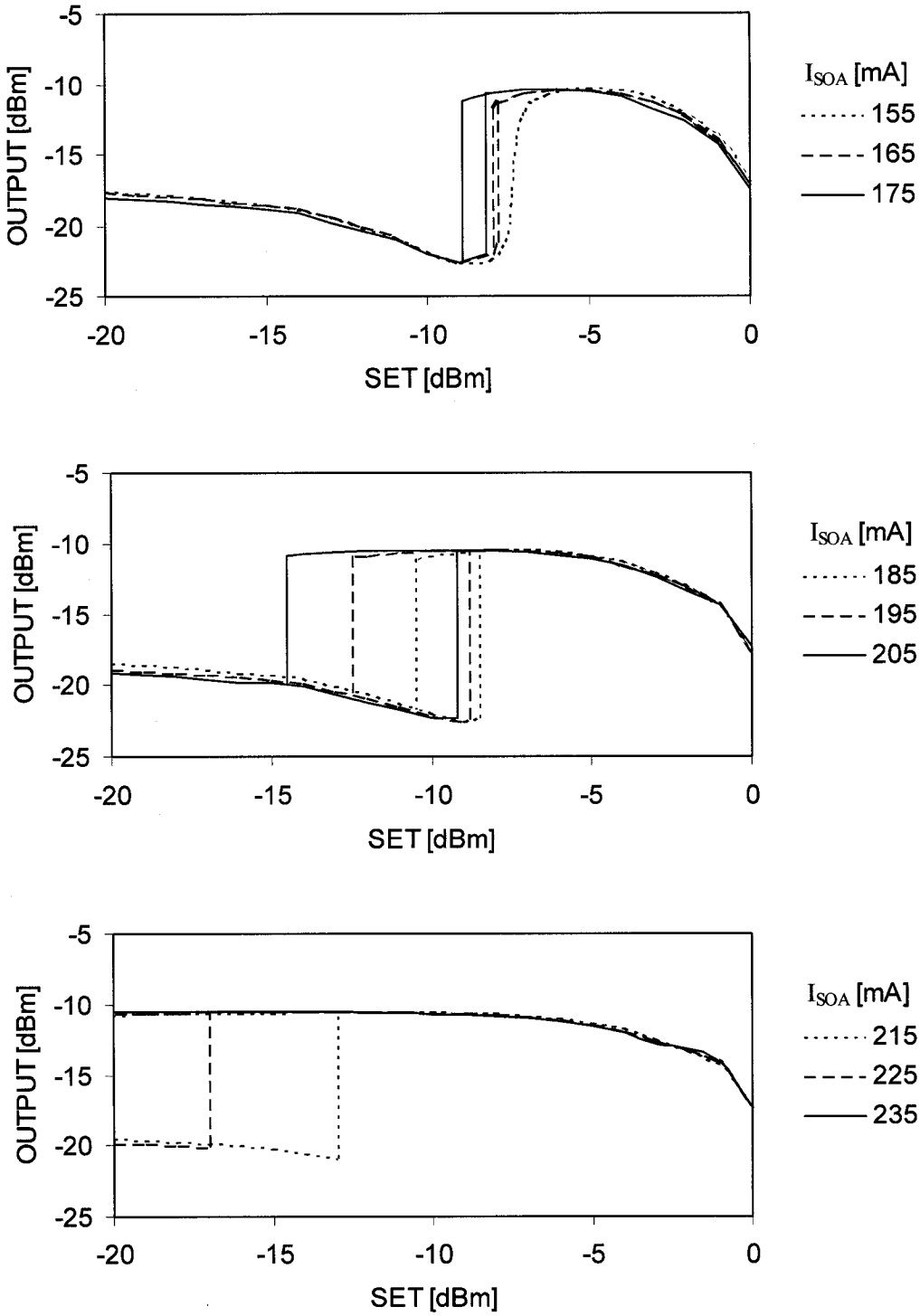

Figure 5-8 Transfer functions of the flip-flop for various values of feedback SOA injection current.

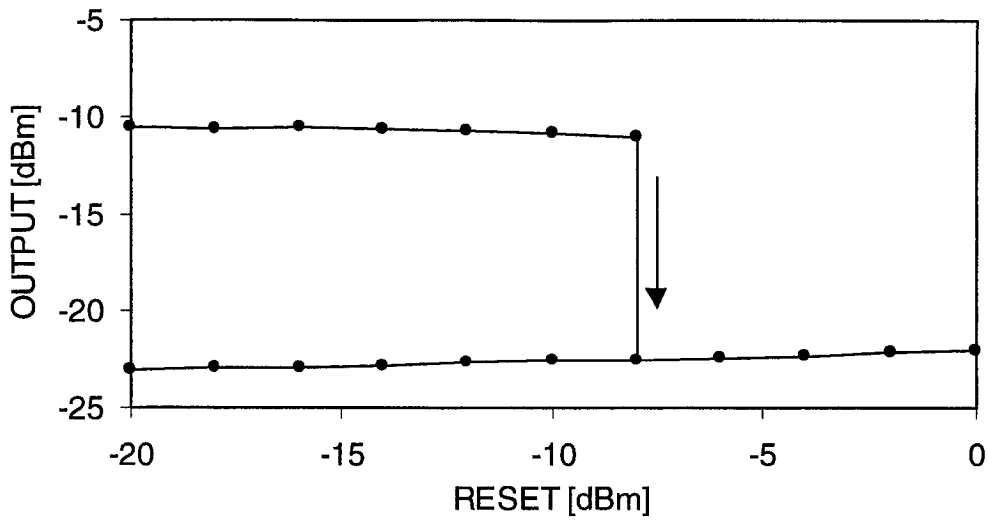

Figure 5-9 Transfer function relating the flip-flop output to the RESET input power.

observed. In this case the gain is so high that even a small initial output power from the interferometer is amplified enough to move the flip-flop output to a high steady state. As discussed in the Chapter 4, an increase in the feedback gain shifts the transfer function up relative to the reference line $P_{In} = P_{Out}$, and when sufficiently large, it is possible for there to be only one intersection point with the reference line and thus only one steady state.

The transfer function relating the OUTPUT to the RESET input was also obtained and is shown in Figure 5-9. In this case, the SET power was set to -10 dBm to represent a logic low and I_{SOA} was 191 mA.

5.2.2 Basic Dynamic Operation

To test the dynamic operation of the flip-flop, optical SET and RESET signals were prepared as shown in Figure 5-10. An Agilent 33250A 80MHz Function and Arbitrary Waveform Generator and an HP8082A Pulse Generator were used to generate the initial electrical signals. The latter was synchronized to the

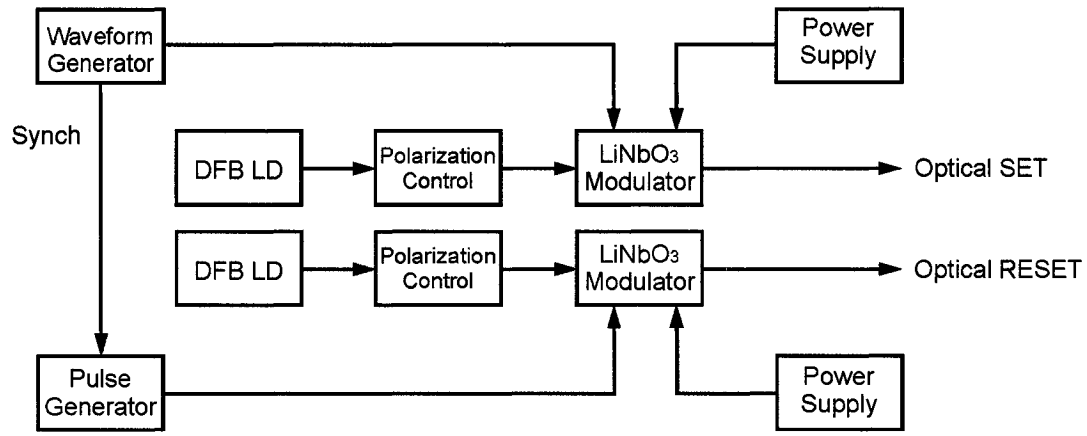

Figure 5-10 Block diagram of the hardware setup used to generate optical SET and RESET signals for testing the basic dynamic operation of the flip-flop.

former, and the electrical signals were used to drive lithium niobate optical modulators. The modulators were polarization sensitive and required the polarization of the optical inputs to be controlled. As well, it was found that the modulators were sensitive to temperature and needed a warmup time of several hours since they did not have temperature control. The electrical signal amplitudes and DC bias levels were then adjusted to optimize the extinction ratio of the modulated optical signals.

Dynamic operation of the flip-flop is shown in Figure 5-11. In this figure the bit rate has been set to 4.3 Mb/s. The input bit pattern is SET, NIL, RESET, NIL, where NIL signifies that both inputs are in the low state. In this example the flip-flop maintains the set or reset condition for one bit without any optical inputs. Of course the flip-flop can remain in a given state indefinitely, as evidenced by the steady state transfer functions shown in Figure 5-8 and Figure 5-9.

In general, temporal overlap of the SET and RESET signals should be avoided. This can be made possible through the use of conditioning logic on the incoming SET and RESET signals. However, it is instructive to observe the behavior of the flip-flop when such an overlap occurs. Figure 5-12 shows the effect of a SET pulse that arrives halfway through an existing RESET pulse.

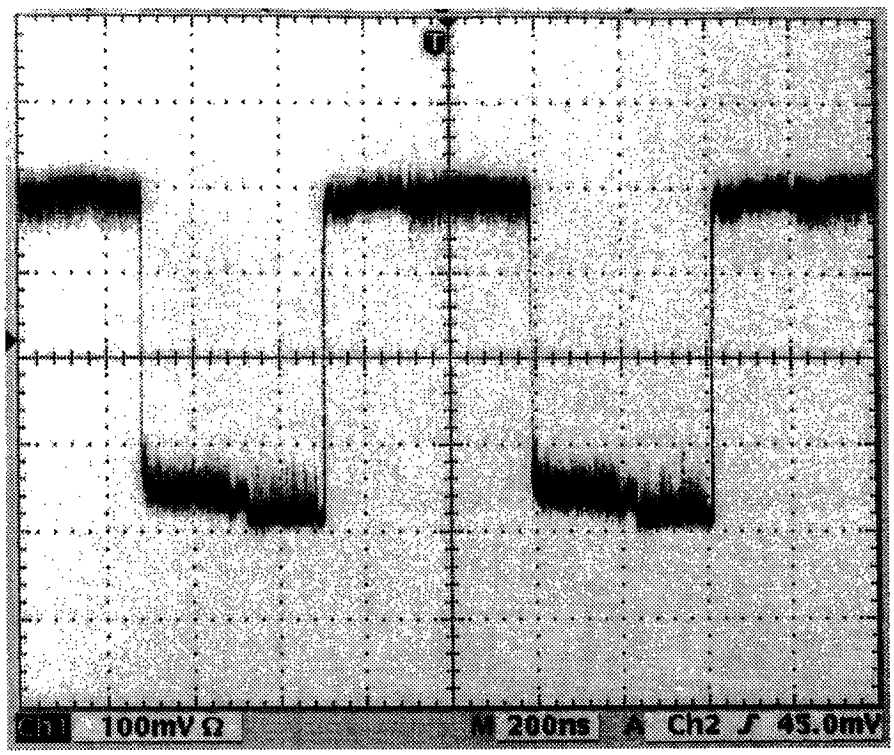

Figure 5-11 Dynamic operation of the flip-flop. The input bit pattern is SET, NIL, RESET, NIL.

Logically, the SET pulse is dominant. This is true because the output of the flip-flop, as built, is taken before the feedback SOA. If it was desirable to have a dominant RESET pulse, then the output of the flip-flop could be taken from after the feedback SOA. Importantly, the flip-flop suffers no undesirable effects from the temporal overlap of the pulses. It should be noted that the remainder of the traces in this subsection were collected early during the experimentation, and the control parameters were not optimized to reduce noise.

In Figure 5-13, the RESET pulse arrives halfway through an existing SET pulse. As the SET pulse is dominant, we see that the output remains high for the duration of the SET. However, the RESET pulse does not last long enough to extinguish the circulating light created by the trailing end of the SET pulse. Thus an undesirable condition is created where the flip-flop output oscillates. These oscillations could be stopped by applying a second RESET pulse, or by ensuring

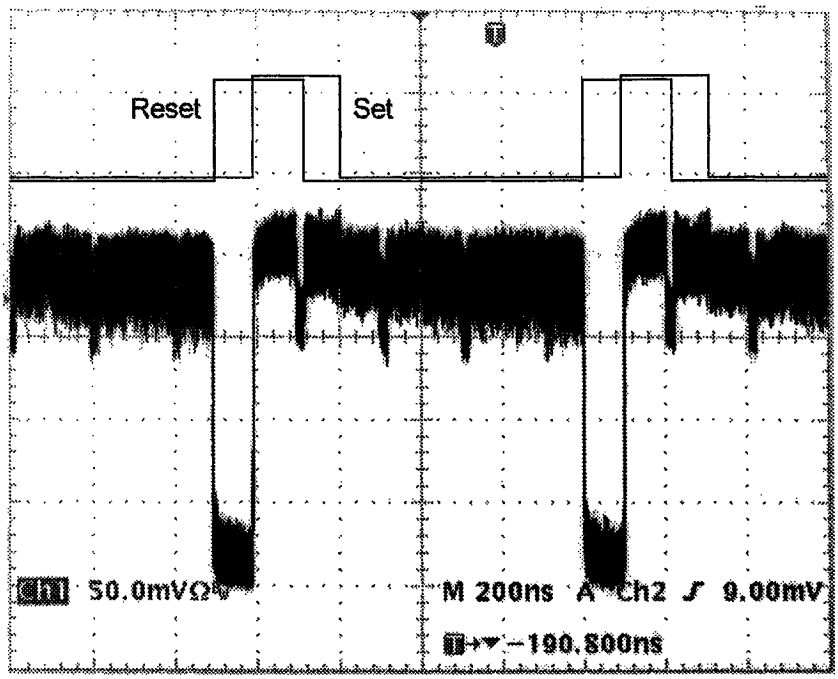

Figure 5-12 Flip-flop response to a SET pulse that arrives midway through a RESET pulse.

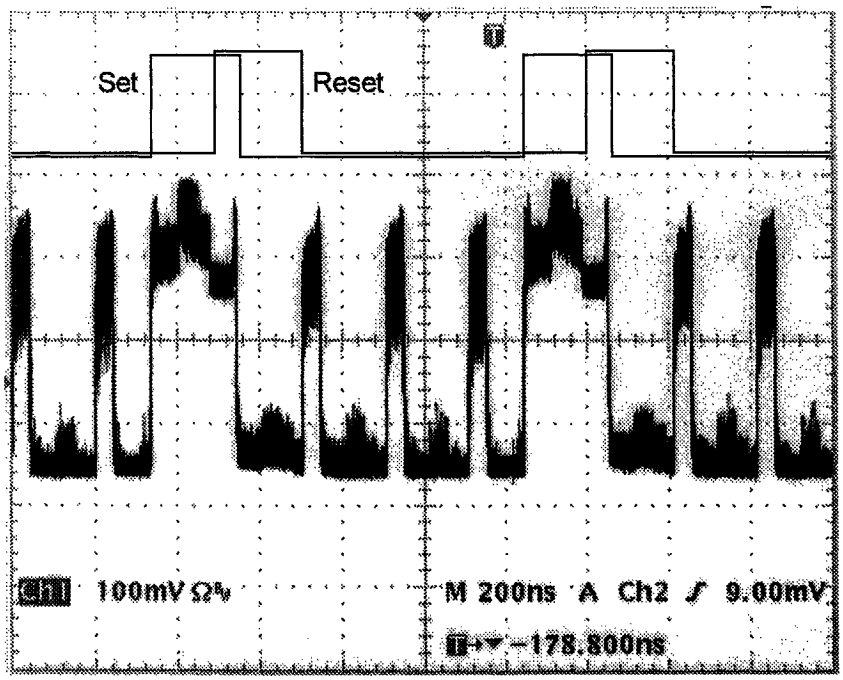

Figure 5-13 Flip-flop response to a RESET pulse that arrives midway through a SET pulse.

the RESET lasts for one full bit period after the end of a SET pulse. Of course the situation is best avoided altogether by ensuring that the SET and RESET never overlap.

The maximum operating speed of the flip-flop is controlled by three factors. The first is the speed of the SOAs in the interferometer, which will limit rise and fall times. This is explored further in the following subsection. The second factor is the effect of critical slowing down which is partly determined by the shape of the transfer function. This is also discussed later. The third factor is the optical delay of the feedback loop.

The minimum bit period of the optical inputs cannot be shorter than the loop delay. If the RESET pulse duration is slightly shorter than the loop delay, then a pulse is created in the feedback loop and cycles around the loop as illustrated in Figure 5-14a. If the SET pulse duration is shorter than the loop delay, a brief duration of low optical intensity will cycle around the loop as illustrated in Figure 5-14b. This figure shows the effect of a RESET pulse and a SET pulse that are of insufficient duration. The oscillations can be removed from the flip-flop by applying an input pulse that is longer than the loop delay.

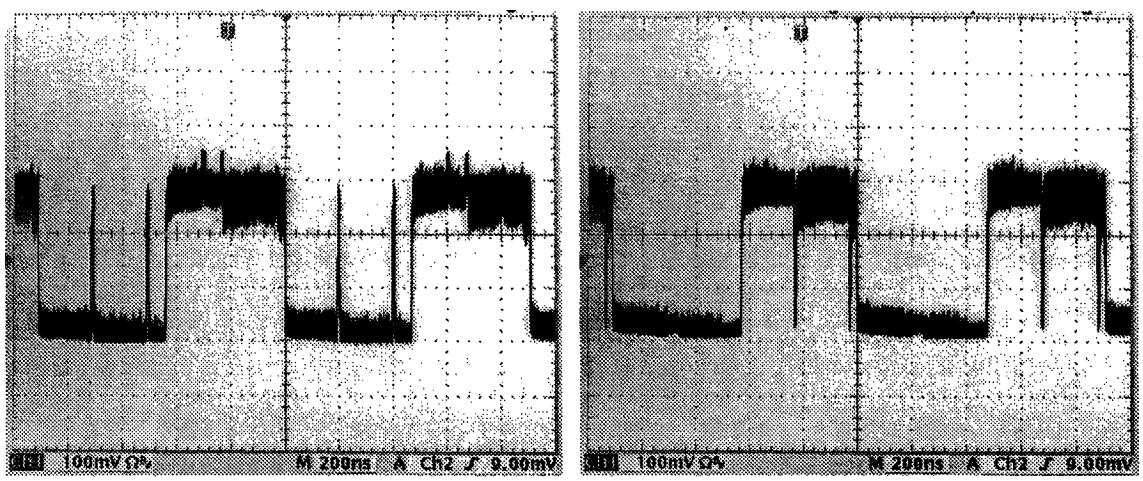

a) b)

Figure 5-14 Effect of a) a RESET pulse slightly shorter than the loop delay and b) a SET pulse slightly shorter than the loop delay.

The period of the circulating pulse is seen to be 200 ns. This corresponds to a maximum operating bit rate of 5 MHz. This limiting factor is the length of the feedback loop. If it is assumed that the feedback loop consists only of fiber, with a mode index of 1.47, then the length of the feedback loop would be expected to be 40.8 m. The fiber pigtails of the various components were measured and gave a total length of only 35.8 m. There was one coupler in a large sealed plastic case that could not be opened, which would have contained an additional length of fiber. The input pulse energy required to switch the flip-flop was approximately 0.2 nJ, again limited by the feedback loop length. With a shorter loop, shorter control pulses duration could be reduced and switching energies of a few hundred femtojoules would be possible.

5.2.3 Rise and Fall Times

Knowledge of the rise and fall times is important in determining the maximum operating bit-rate of the flip-flop. To measure the rise and fall times, it was necessary to supply the flip-flop with short rise time SET and RESET pulses. An Anristu pattern generator and an HP pulse generator were used as shown in Figure 5-15 to modulate the lithium niobate modulators. The minimum clock frequency of the pattern generator was 100 MHz and, as previously discussed, the maximum bit-rate of the flip-flop was approximately 5 Mb/s. Therefore it was necessary to program the pattern generator to produce strings of ones and zeros such that the apparent bit-rate was low, while retaining short pulse rise times. The electrical output of the pattern generator was sent through a fixed gain amplifier and a variable attenuator. The resulting signal was used to control a lithium niobate modulator. A RESET pulse was produced using a separate pulse generator that was triggered by a synchronization pulse from the pattern generator.

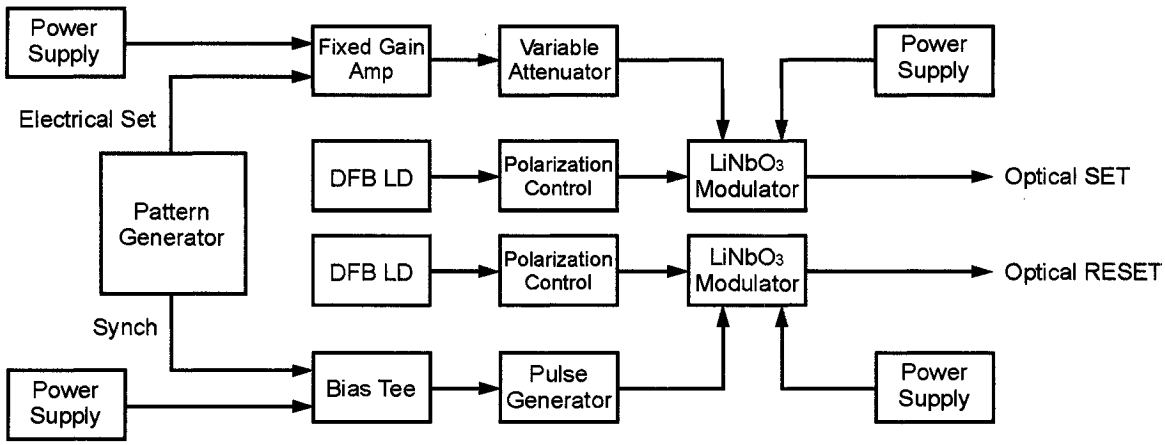

Figure 5-15 Block diagram of the hardware setup used to generate a short rise time optical pulse for the measurement of the flip-flop response time.

The setup just described was used to measure the rise time of the flip-flop only, because the rise time of the pattern generator was much shorter than that of the pulse generator. To measure the fall time of the flip-flop, the electrical signals to the lithium niobate modulators were exchanged.

The rise time of the SET pulse is now calculated. The pattern generator rise time (20% to 80%) is specified as 30 ps maximum. The amplifier rise time (10% to 90%) is specified as 40 ps maximum. The attenuator rise time is assumed to be negligible. The modulator bandwidth is 15 GHz, corresponding to a rise time of 23 ps. The maximum total rise time of the optical SET pulse is then

$$TotalRiseTime_{Max} = \sqrt{(30\,\mathrm{ps})^2 + (40\,\mathrm{ps})^2 + (23\,\mathrm{ps})^2} = 55\,\mathrm{ps}. \qquad (5.1)$$

The optical SET pulse is shown in Figure 5-16. The analyzer averaged traces in groups of ten to allow the transitions to be seen more clearly; the screen persistence was set to one second. The measured rise time of the detected optical SET pulse was 38 ps (10% to 90%), which is below the maximum rise time calculated above.

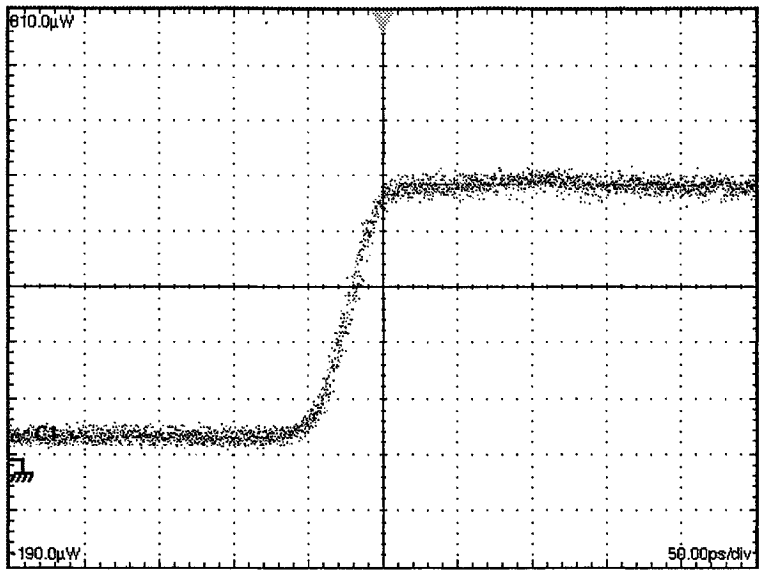

Figure 5-16 Turn on transient of the optical SET pulse. The horizontal scale is 50 ps/div, and the vertical scale is 80 µW/div.

The optical SET pulse in Figure 5-16 was used for some measurements detailed later in this section. For the measurement of the rise and fall times of the flip-flop, an electrical cable with a bandwidth of about 4 GHz was used to connect the variable attenuator to the lithium niobate modulator. The resulting SET pulse, which was used to measure the rise and fall times of the flip-flop, is shown in Figure 5-17. From the figure the rise time is approximately 60 ps (10% to 90% measured with respect to the final settling value). As will be shown, the use of this SET pulse does not affect the rise and fall time measurements of the flip-flop as those times are significantly longer than the rise time of the SET pulse.

Using the optical SET pulse of Figure 5-17, the response of the flip-flop was measured and is shown in Figure 5-18. The rise time is approximately 280 ps (10% to 90% measured with respect to the final settling value). This long transition time was not anticipated. For a better understanding, it is useful to consider the optical components in the flip-flop. In the experimental setup, the SET pulse was fed through a coupler directly into the interferometer. The output

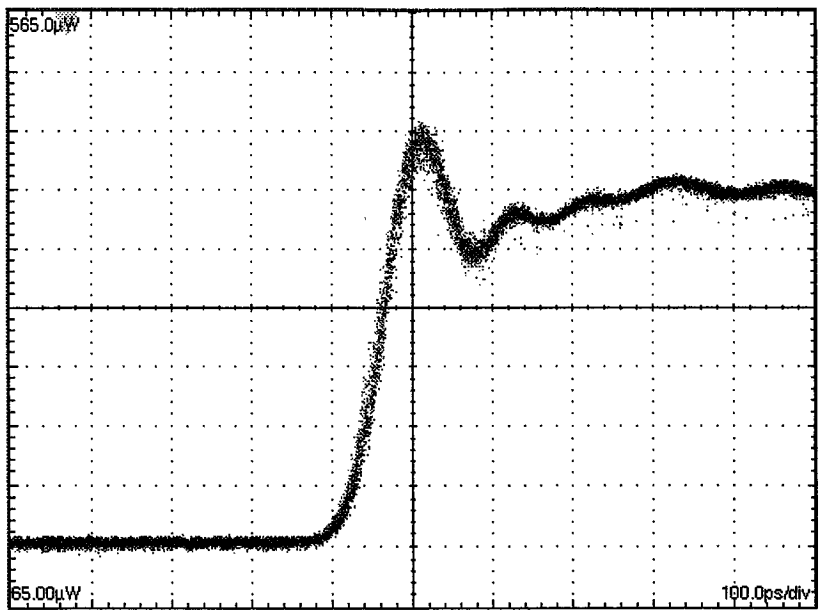

Figure 5-17 Optical SET pulse generated with lower bandwidth electrical cable. The horizontal scale is 100 ps/div, and the vertical scale is 50 µW/div.

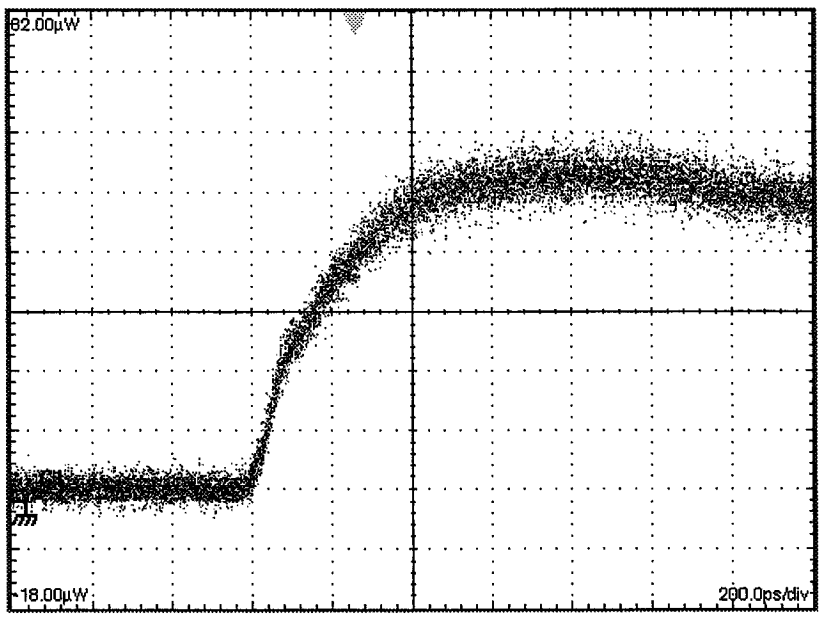

Figure 5-18 Transient response of the flip-flop to a SET pulse.

of the interferometer passed through a circulator, fiber Bragg filter, and splitter. One output of the splitter was fed directly into the analyzer. None of the passive

components play a part in the rise time because there is no energy storage as in an active device and because any dispersion, when considered over the time scales and physical lengths involved, is negligible. The input pulse and the analyzer are not limiting the observed rise time either. Therefore the rise time must have been limited by the interferometer.

The fall time of the flip-flop was also measured. In this case the electrical signals to the lithium niobate modulators shown in Figure 5-15 were exchanged. Thus the RESET pulse had the rising edge transients of Figure 5-17 and a rise time of 60 ps. The response is shown in Figure 5-19. The fall time is approximately 320 ps. In this case, the response is due to both the feedback SOA and the SOAs in the interferometer.

Rise and fall times in the range of 280 ps to 320 ps are considered quite slow for an MZI-SOA, and some time was spent trying to determine the cause of the slowing. The author feels that the causes of the slowing were the relatively low CW power and the low injection currents supplied to the MZI-SOA. These have two effects on the overall performance. The first effect is poor light-carrier

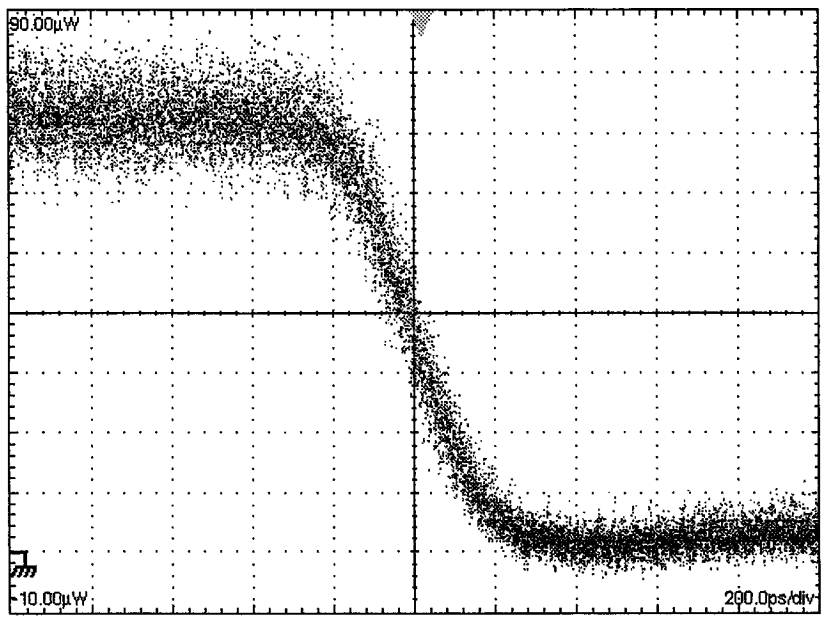

Figure 5-19 Transient response of the flip-flop to a RESET pulse.

interaction. High optical powers and current densities improve the speed of an NZI-SOA [ASGH97], as shown numerically in the previous chapter. To solve this problem, some time was spent looking for a suitable transfer function at an alternate operating point. Unfortunately, a suitable transfer function was not found for a higher CW power. This does not mean that one does not exist, or could not be produced with an MZI with asymmetric arm lengths, but they can be difficult to find.

A second effect of the low CW input power is that the ASE noise produced by the SOAs in the MZI contributes more to the feedback power. Even with excellent filtering, the in-band ASE noise will remain. It has been shown that residual ASE noise in the detected signal plays an important part in the measured response time of an MZI-SOA [CAO03 Section 3.5]. The measured response time depends in a complex way on the amount of ASE noise present, on the type of a transfer function used, and on whether co-propagating or counter-propagating XPM is employed.

To support these arguments and to verify that the slow rise and fall times could, in principle, be improved with the experimental equipment used in this thesis, the rise time of the interferometer was measured for a different operating point. Specifically, the operating parameters were I1 = 20 mA, I2 = 120 mA, I3 = 200 mA, I'3 = 59 mA, I4 = 170 mA, I'4 = 10 mA, and CW power = 4.24 dBm. This was the operating point used by Cao [CAO03 pg. 51]. In particular, note that his CW power and I3 were considerably higher than those used in this thesis, which were –5 dBm and 100 mA, respectively. While this new operating point did not produce a transfer function suitable for building a flip-flop, it did demonstrate a significantly improved response as shown in Figure 5-20. The rise time of the trace is approximately 100 ps. Deconvolving the effects of the rise time of the input pulse (38 ps), the interferometer response in this case is 92 ps. That is a considerable improvement over the operating point that was necessary for the work in this thesis.

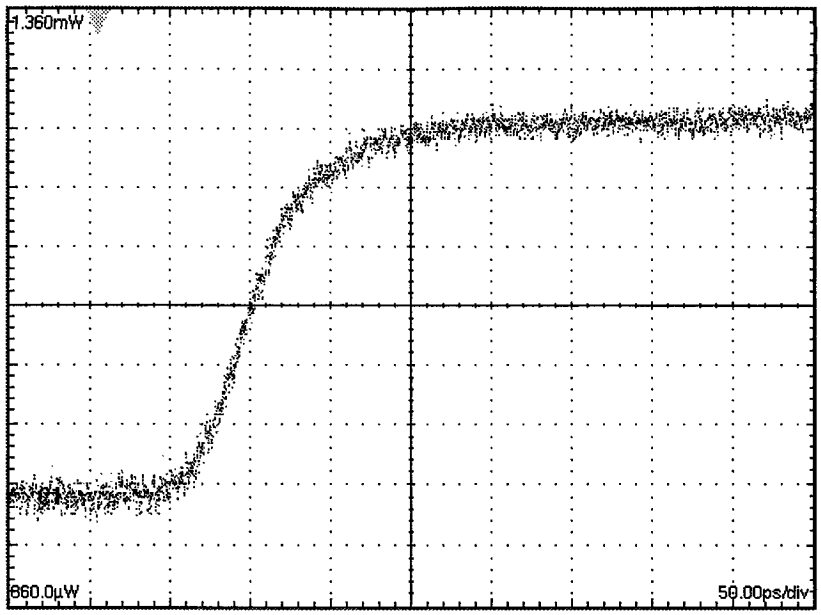

Figure 5-20 Transient response of the interferometer using the operating point of [CAO03]. The rise time is about 95 ps.

5.2.4 Critical Slowing Down

To this point, we have considered the rise times of the flip-flop in response to the SET pulse. It has been assumed that the SET pulse was of the proper intensity to force the output of the flip-flop to its steady state logical high value within a single bit period, as would normally be the case. However, the flip-flop may also be used to demonstrate critical slowing down. This effect dominates the behavior of the flip-flop when switching occurs near the turn-on threshold of the bistability. It is an effect that is only observed through multiple cycles of the optical signal through the feedback loop, corresponding to multiple bit periods.

It was found that for the purposes of understanding the behavior, a long SET pulse was beneficial. In the results described below, a 2.3 µs SET pulse was used at a repetition rate of 250 kHz. The low repetition rate was necessary to observe the long transient responses associated with the critical slowing down. In addition, the RESET pulse was delayed for the same purpose.

To begin, Figure 5-21a shows a reference waveform in which the SET power was optimized to produce a rapid response from the flip-flop. Point 1 is where the flip-flop first responded to the SET. The only input into the interferometer was the SET pulse. At point 2, the feedback light completed its first pass of the

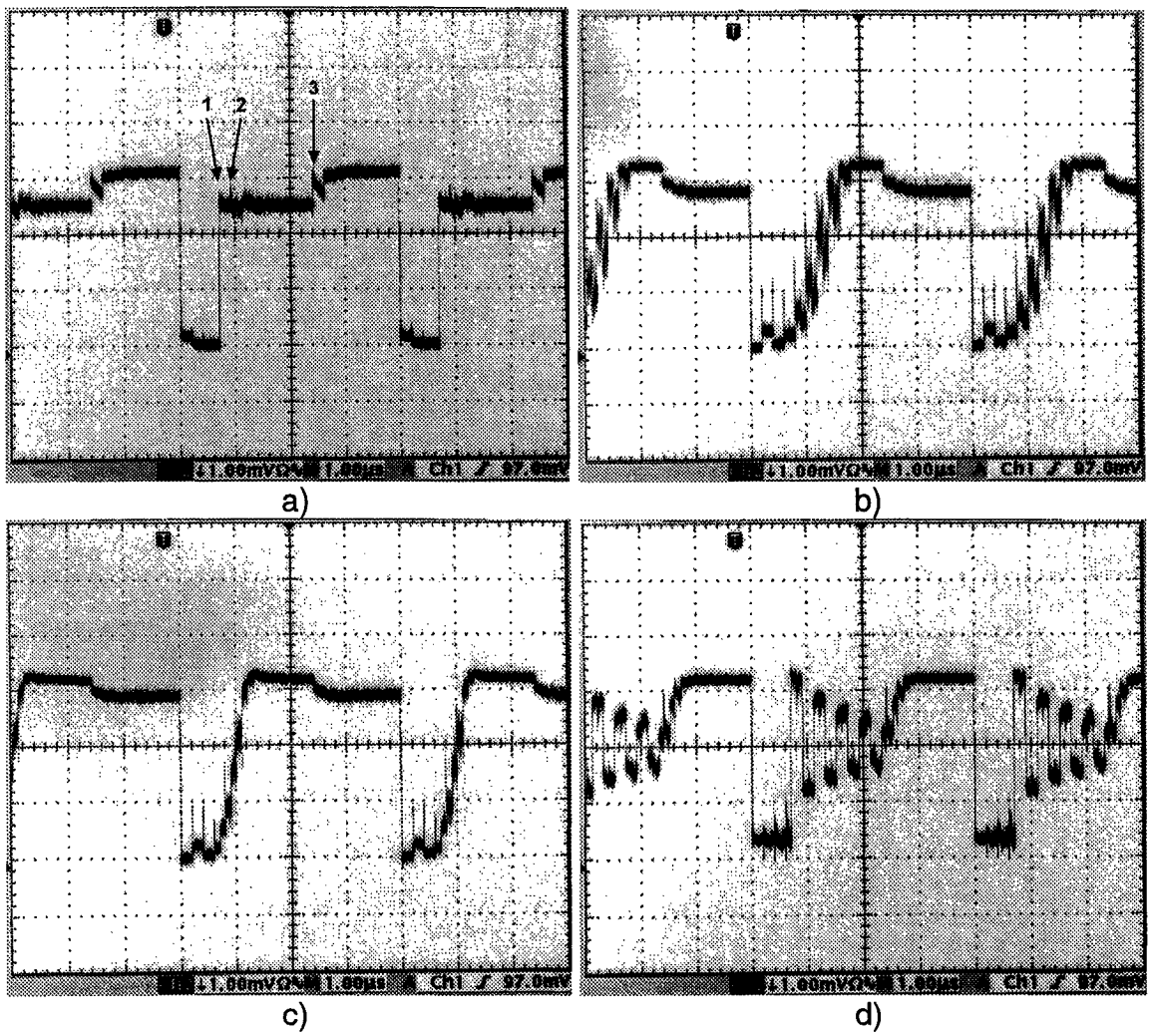

Figure 5-21 Flip-flop response to a 2.3 μs SET pulse and a standard (but delayed) RESET pulse, at a repetition rate of 250 kHz. a) SET power of -4 dBm used as reference trace. The SET power has been optimized to produce a sharp transition at the front end of the flip-flop response. b) SET power of -7.8 dBm showing critical slowing down and overdamped settling. c) SET power of -6 dBm showing reduced critical slowing down and shorter settling time. d) SET power of –3 dBm showing underdamped settling.

feedback loop, with a feedback delay of 200 ns. Thus the input to the interferometer at point 2 was the sum of the SET power and the feedback power. The SET pulse power was adjusted such that the flip-flop output power was the same when a) the SET alone was present and b) when the SET and the feedback power were both present. This was possible due to the hump in the upper part of the open loop transfer function which indicates that a single output power level can be produced at two different input powers (see Figure 5-3). At point 3 the SET pulse ended, thus the only power into the interferometer was the feedback power. The flip-flop then settled to its upper static operating point.

When a much smaller SET power was used, critical slowing down was observed. Figure 5-21b and Figure 5-21c show critical slowing down for two low SET powers. In these cases, the SET power, when combined with the light that had completed the first pass of the feedback loop, was larger than the decision point given by the intersection of the open loop transfer function and the line $P_{In} = P_{Out}$. The flip-flop output power slowly increased with each pass of the loop.

In Figure 5-21d, a large SET power was used such that the operating point was at the very right of the transfer function where there is a negative slope. The negative slope is associated with underdamped oscillation, as seen in the trace.

Clearly these sorts of transients must not occur for proper flip-flop operation. They can be avoided by choosing input powers that quickly settle to the final power level. However, the best solution, when possible, is to choose a starting transfer function that is as close as possible to a step function: steep in the region of the logical threshold point and flat in the upper and lower regions.

5.2.5 Noise

As evidenced by many of the preceding graphs, the amount of noise in the flip-flop can be undesirably high. Attempts were made to understand the cause of the noise but were met with limited success. Suggested causes for the high noise levels are discussed below.

Considering the spectral output of the interferometer, shown in Figure 5-2, it is clear that the device produces considerable noise due to spontaneous emission and amplified spontaneous emission. Most of this was removed with the fiber Bragg grating at the output of the device, however, in-band noise cannot be removed. This in-band noise is then amplified by the feedback SOA and fed back into the interferometer. From analysis of the movement of operating points along the transfer function given in Section 4.3.3, it can be shown that such noise amplitudes will converge to a settling point. However, this may take several passes of the feedback loop, while new ASE noise is being added to the signal at every pass.

The situation can be improved in three ways. The first is to reduce the amount of noise produced by the MZI-SOA. In practice, the in-band noise can be reduced by increasing the input CW power into the interferometer. Some effort was spent finding a suitable transfer function for a larger CW power, but due to time constraints none was found.

The second method involves improving the transfer function of the interferometer such that the noise converges to the desired logic level in as few passes of the feedback loop as possible. The solution is to make the transfer function shaped more like a step. Improvement of the transfer function could be accomplished through the use of asymmetric arm lengths. With independent control of the gain and phase, an optimized design should provide some improvement in the area of the transfer function around the point of destructive interference.

Another possibility for reshaping the transfer function is through external means. For instance, a nonlinear coupler [DEME02] could be used in the feedback loop to combine the set and feedback powers. If coupling was reduced for larger optical powers, the transfer function would effectively be stretched out at higher powers, flattening the upper part of the curve. A nonlinear multimode interference coupler can be made using the same structure as the SOAs. It

might even be possible to combine the function of the feedback SOA and the nonlinear coupler.

The third method of reducing noise in the system involves operating the MZI-SOA in a co-propagating mode. It has been shown that co-propagating XPM adds less ASE noise to the converted signal than counter-propagating XPM [OBER97]. This difference, up to 5 dB, is attributed to the inhomogeneous longitudinal carrier distribution within the saturated SOA. Co-propagation cannot be used in the proposed flip-flop design because the feedback wavelength is the same as the CW wavelength and could not be separated by a filter. For proper operation the polarization of the feedback signal would have to be made orthogonal to the input CW light, so that they could be separated with a polarizer. The polarization of the SET would also have to be controlled so that it too was blocked by the polarizer.

Finally, the use of an MZI-SOA in the feedback loop in place of the single SOA would also be beneficial. This design would benefit from improved reset characteristics due to the improved extinction ratio provided by XPM over XGM.

5.3 ALL-OPTICAL BUFFER

The optical buffer operates on the same basic principles as the flip-flop. The major difference is that the flip-flop remembers a single bit of information which can be read at any time, while the buffer remembers several bits of information which can only be read at regular intervals. In the flip-flop, a SET must be longer than the optical delay of the feedback loop such that the loop becomes 'filled' with light. Conversely, the buffer replaces the SET with an intensity modulated bit stream. The total duration of the bit stream must be less than the optical delay of the feedback loop. The data bits then circulate around the feedback loop, being re-amplified and reshaped by the interferometer during every pass.

When the buffer is ready to be cleared, a RESET pulse is applied in exactly the same manner as the flip-flop.

In the experiment, the pattern generator was programmed to supply the buffer with the data sequence, 11011000110, to replace the SET pulse used for the flip-flop. The data was allowed to circulate through the buffer three times before being cleared. The buffer then remained empty for three passes of the loop. The results, illustrating the entire write and clear cycle, are shown in Figure 5-22. In addition, a second trace is shown in Figure 5-23 to show the detail of the data. As with the flip-flop, there remains considerable noise; however, the regenerative nature of the flip-flop can be observed, especially by comparing the zeros of the first pass to those of the third pass. Another interesting observation is that the RESET pulse does not completely remove the data sequence. This is because of the limited extinction ratio of the cross gain modulation in the

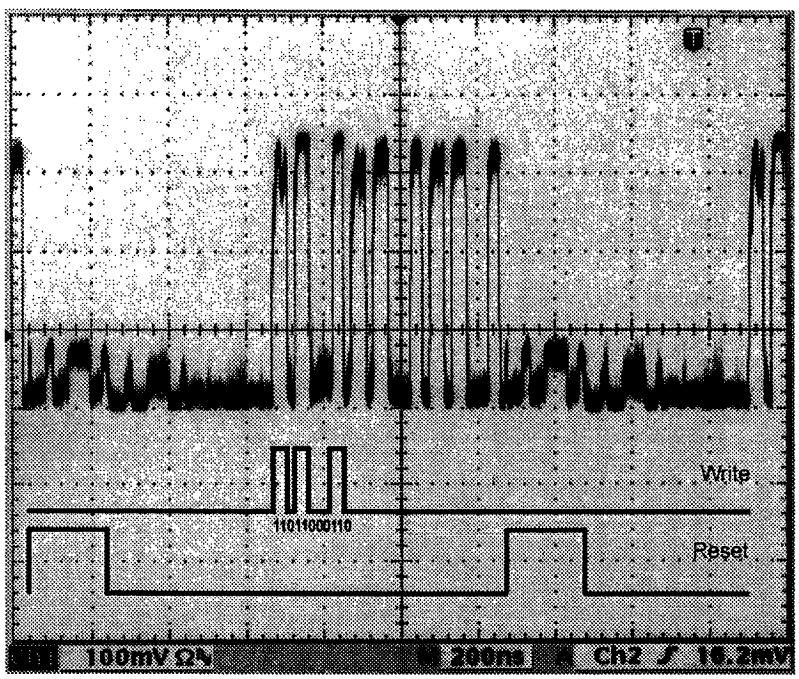

Figure 5-22 Buffer response to the input data sequence 11011000110. The entire write and clear cycle is shown at a time scale of 200 ns/div.

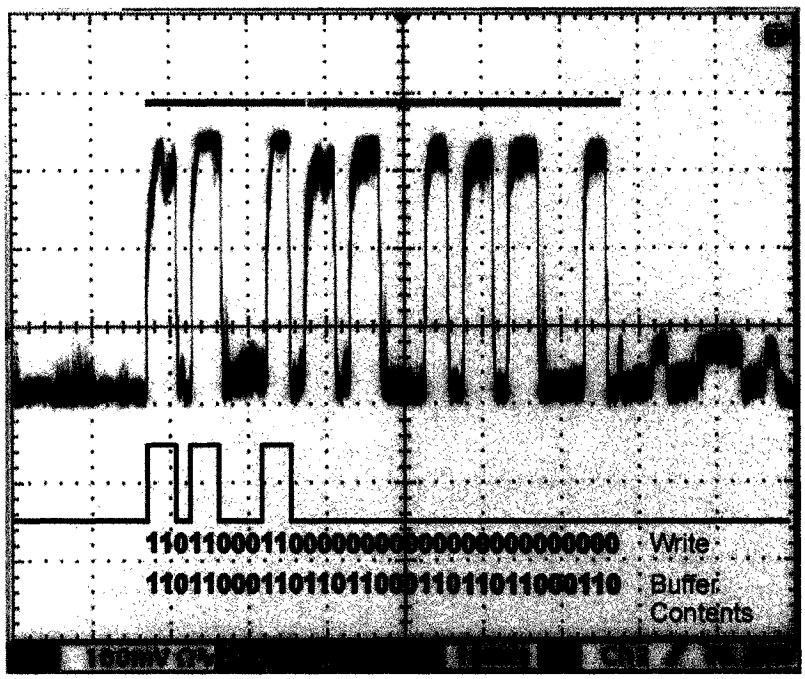

Figure 5-23 Buffer response to the input data sequence 11011000110, at an expanded time scale of 100 ns/div, to show the details of the data sequence as it completes three passes of the optical loop. The three passes are denoted by the red, green, and blue bars above the trace.

feedback SOA. In principle the extinction ratio would improve if the cross gain saturation was optimized or if XPM in an MZI-SOA was used instead of XGM in an SOA. Optimization would involve selecting the RESET wavelength to match the gain peak of the feedback SOA. Such measures would be necessary to minimize crosstalk between two different stored data sequences.

The hardware configuration also allows individual bits to be manipulated while circulating in the buffer. A low bit may be made high through what was previously designated the SET port of the flip-flop. A high bit may be made low through what was designated the RESET port. With only one programmable data source available, it was only possible to show the rewriting of bits from zeros to ones. The results are shown in Figure 5-24. In this example, the data sequence 11011000110 was written to the buffer, as before. On the second pass of the data, the input to the SET port was 00000011000, which had the

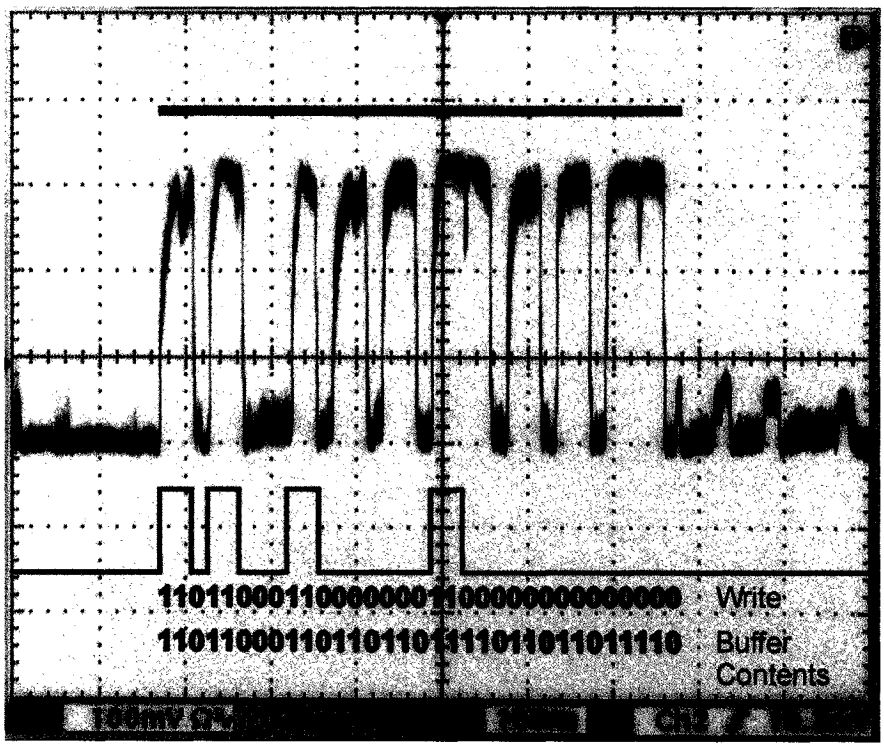

Figure 5-24 An example of modifying data in the optical buffer. The data sequence 11011000110 is changed to 11011011110 by applying 00000011000 to the write input on the second pass of the data in the loop.

effect of rewriting two of the zeros in the initial data sequence with ones. The new data sequence was again observed circulating the buffer on the third pass.

The dip in the output power immediately following the rewritten bits is due to an imperfect match between the data rate of the pattern generator and the optical loop delay. This demonstrates the need for very precise loop delay control if the buffer were to be used in practice. Such control could possibly be achieved using a variable refractive index material in the feedback loop, such as lithium niobate. A control system could then be used to continuously vary the refractive index of the material, to maintain a constant optical loop delay. Another option would be to use temperature control on the feedback loop.

5.4 ALL-OPTICAL OSCILLATOR

In electronics a simple ring oscillator can be constructed using an inverting logic gate and connecting the output to the input. The same principle can be applied to an MZI-SOA with an inverting transfer function. An oscillating output is produced, with a fundamental frequency determined by the optical delay of the feedback loop. Assuming the stability condition discussed in section 4.3.5 is met, the signal is continuously regenerated. When the rise and fall times of the MZI-SOA are much less than the period of oscillation, the output approaches the shape of a square wave.

To obtain an oscillating output, I4 was set to 80 mA. The MZI-SOA then operated with an inverting transfer function. I_{SOA} was adjusted to optimize the output so that it had the largest extinction ratio and lowest noise. In this case the current was 178 mA. The output is illustrated in Figure 5-25. With these injection current settings, the static transfer function of the MZI was measured and is shown in Figure 5-26 as a solid line. To indicate the operating points of the oscillator, the transfer function, shown as a dotted line, is mirrored about the line Input = Output (not shown). The outer two intersection points of the curves represent the operating points of the oscillator. As can be seen, the optimized operating point occurs when one of the operating points is in the lowest part of the dip of the transfer function.

The optical delay of the feedback loop linearly controls the oscillation period. Lengths of fiber were inserted into the feedback loop to increase its length. For each loop length the half-period of the oscillating waveform was measured. The data, confirming the linearity of the oscillation-period control, are plotted in Figure 5-27.

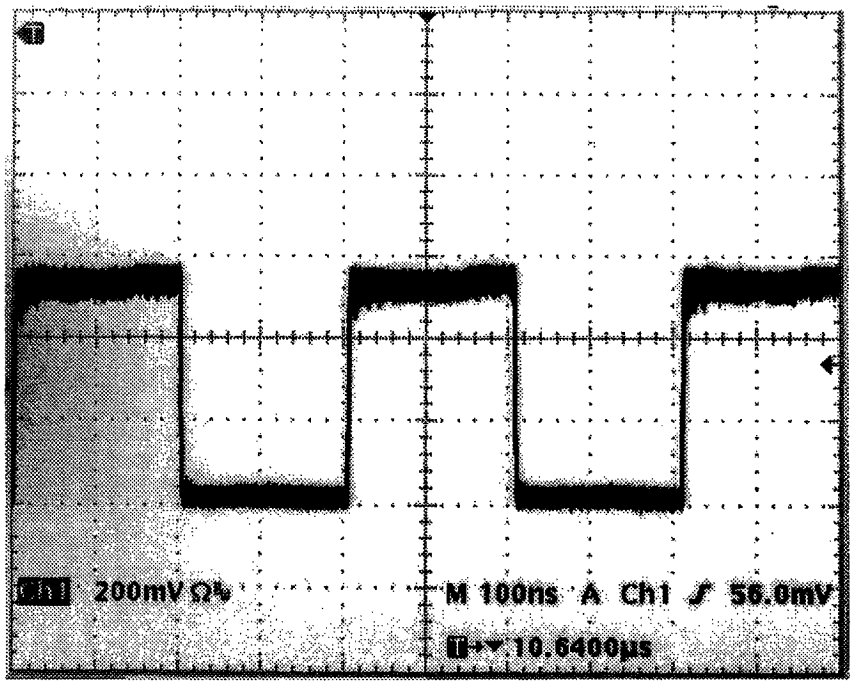

Figure 5-25 Output signal from the all-optical ring oscillator.

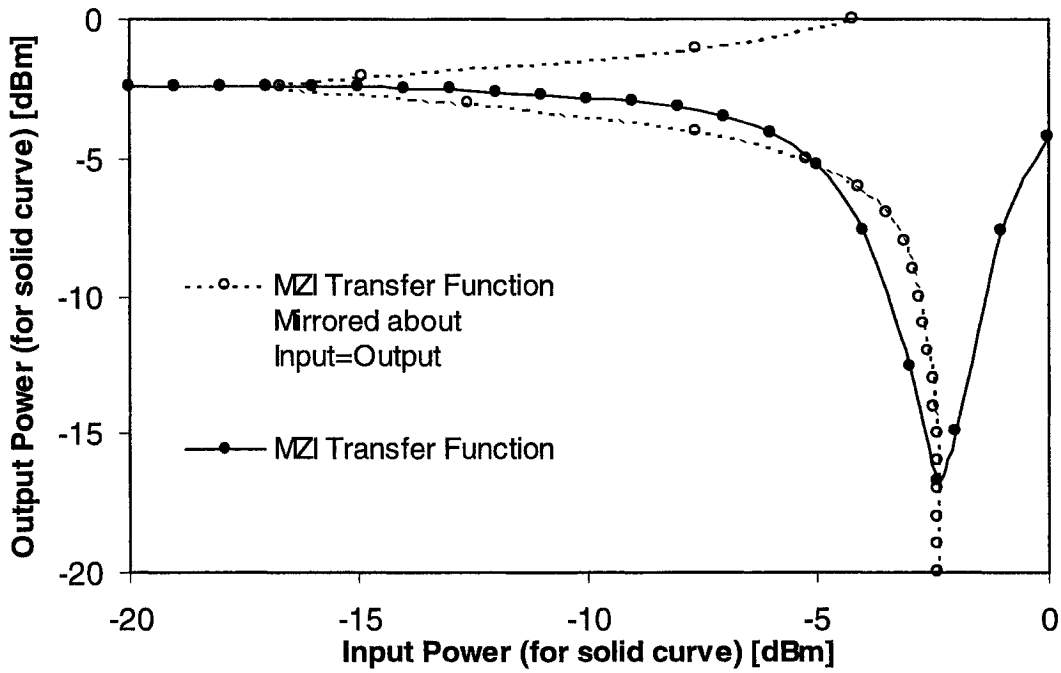

Figure 5-26 Inverting transfer function of the interferometer (solid) and a copy (dotted) mirrored about the line Input = Output (not shown). The outer intersection points represent the oscillator operating points.

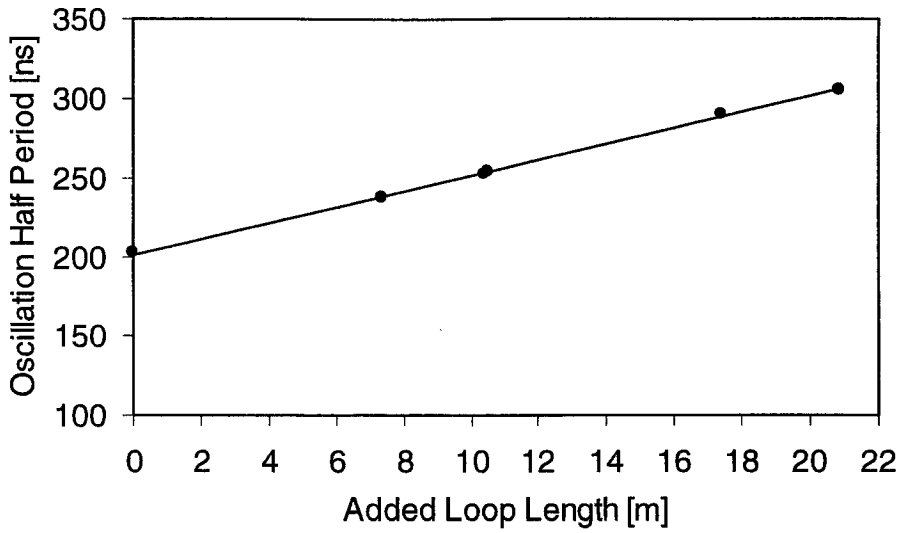

Figure 5-27 The effect of added fiber to the feedback loop as a way to control oscillation period.

Details of the rise and fall times of the oscillator output are shown in Figure 5-28. These traces were obtained on a Tektronix CSA800 Communications Signal Analyzer, with the bandwidth set at 12.5 GHz. The output was averaged over ten traces to reduce the noise level, allowing the transition to be shown more clearly. The rise time (10% to 90%) is 300 ps and the fall time is 280 ps. As with the flip-flop, these times are much longer than those corresponding to the maximum operating speed of the interferometer.

The maximum operating frequency of the oscillator is determined by both the rise and fall times, as well as the loop delay. As an example, consider an oscillator suitable for OC-48 (i.e. 2.5 GHz). If it is assumed that the average refractive index of the feedback loop is between 1.5 and 3, corresponding to mostly glass and mostly semiconductor, respectively, the required loop length would be 8 cm and 4 cm, respectively. Unlike the flip-flop, optical inputs are not needed for the oscillator, simplifying the design. With discrete micro optical components, those loop lengths are feasible.

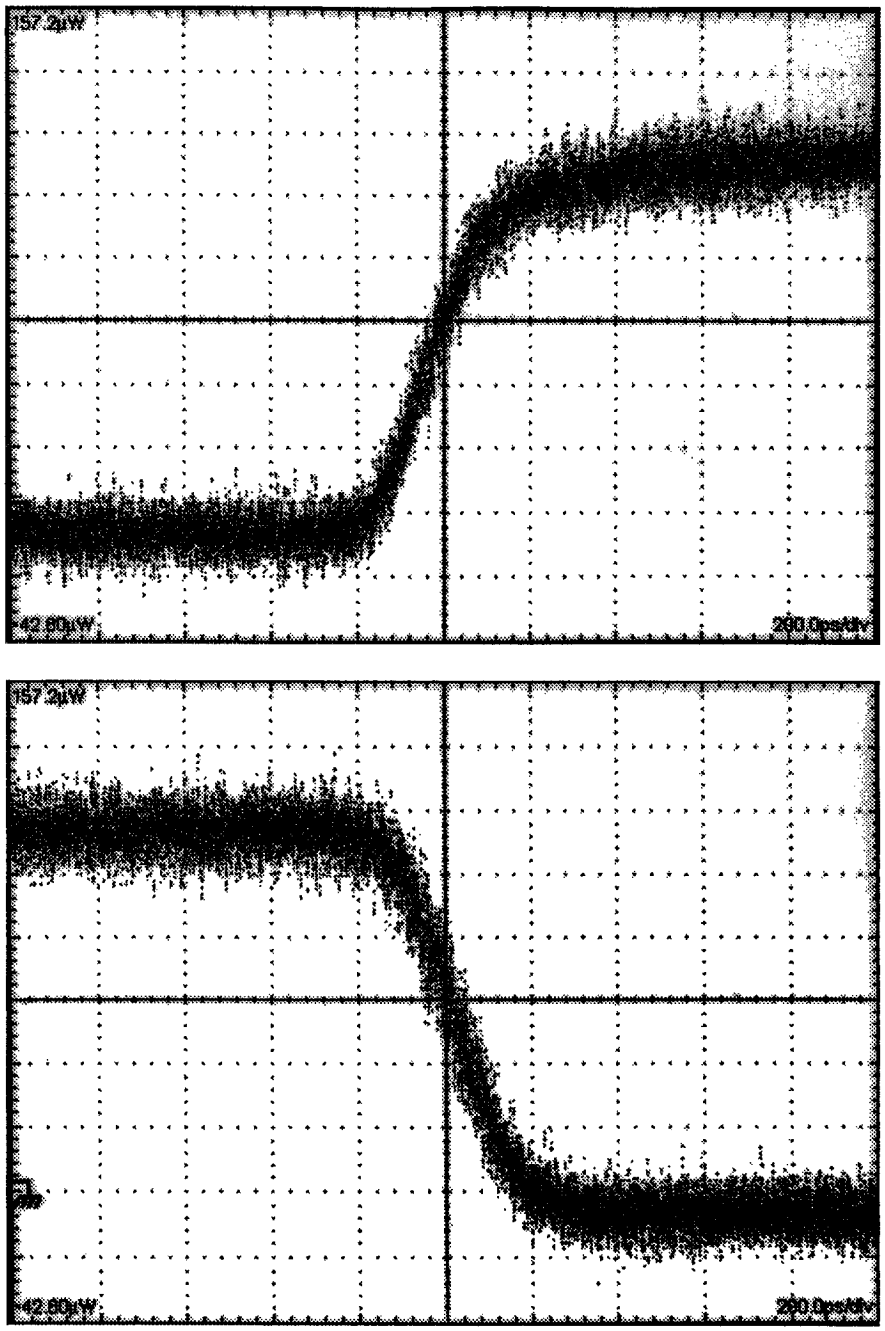

Figure 5-28 Rising and falling edges of the oscillator output. The time scale is 200 ps/div.

5.5 ELECTRICAL FUNCTIONALLY-EQUIVALENT CIRCUITS

It was not possible to build the patented flip-flop with the optical hardware available. While the Alcatel integrated MZI contained all of the necessary waveguides, the one biased by I'4 in Figure 5-1 was not fiber pigtailed in the packaged unit. To demonstrate the oscillatory behavior, a functionally-equivalent electrical circuit was built and tested, using simple digital logic chips to emulate the optical circuits. For comparison purposes another functionally-equivalent circuit was tested that represented the proposed flip-flop.

Figure 5-29 shows the schematic of an electrical logic circuit that is functionally-equivalent to the patented optical flip-flop shown in Figure 4-11. As discussed in Chapter 4, the MZI in the patented flip-flop is functionally-equivalent to an XOR gate. In addition the optical coupler that combines the Set and the feedback signal is functionally-equivalent to an electric OR gate. The assumption is that either of those optical signals, or the sum of those signals, is treated as a logic 'high' by the MZI. This is necessary for the proper operation of the flip-flop, so the assumption is valid.

The circuit shown in Figure 5-29 was built and tested using a length of coaxial cable to increase the feedback loop delay to 150 ns so that the resulting

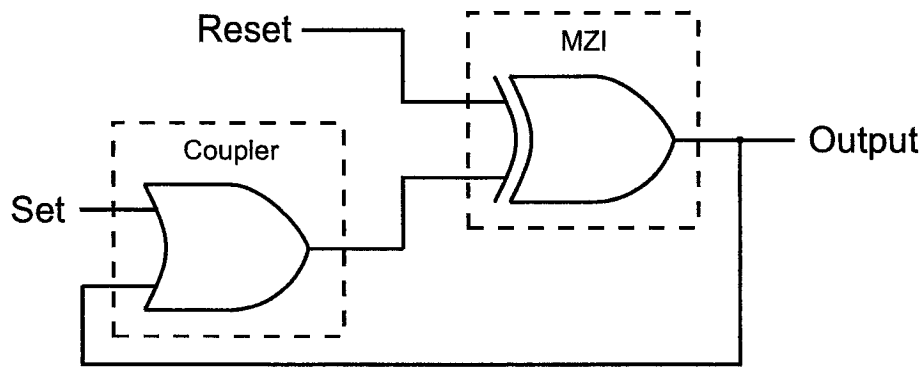

Figure 5-29 Schematic of the electrical circuit that is the functional-equivalent of the patented flip-flop.

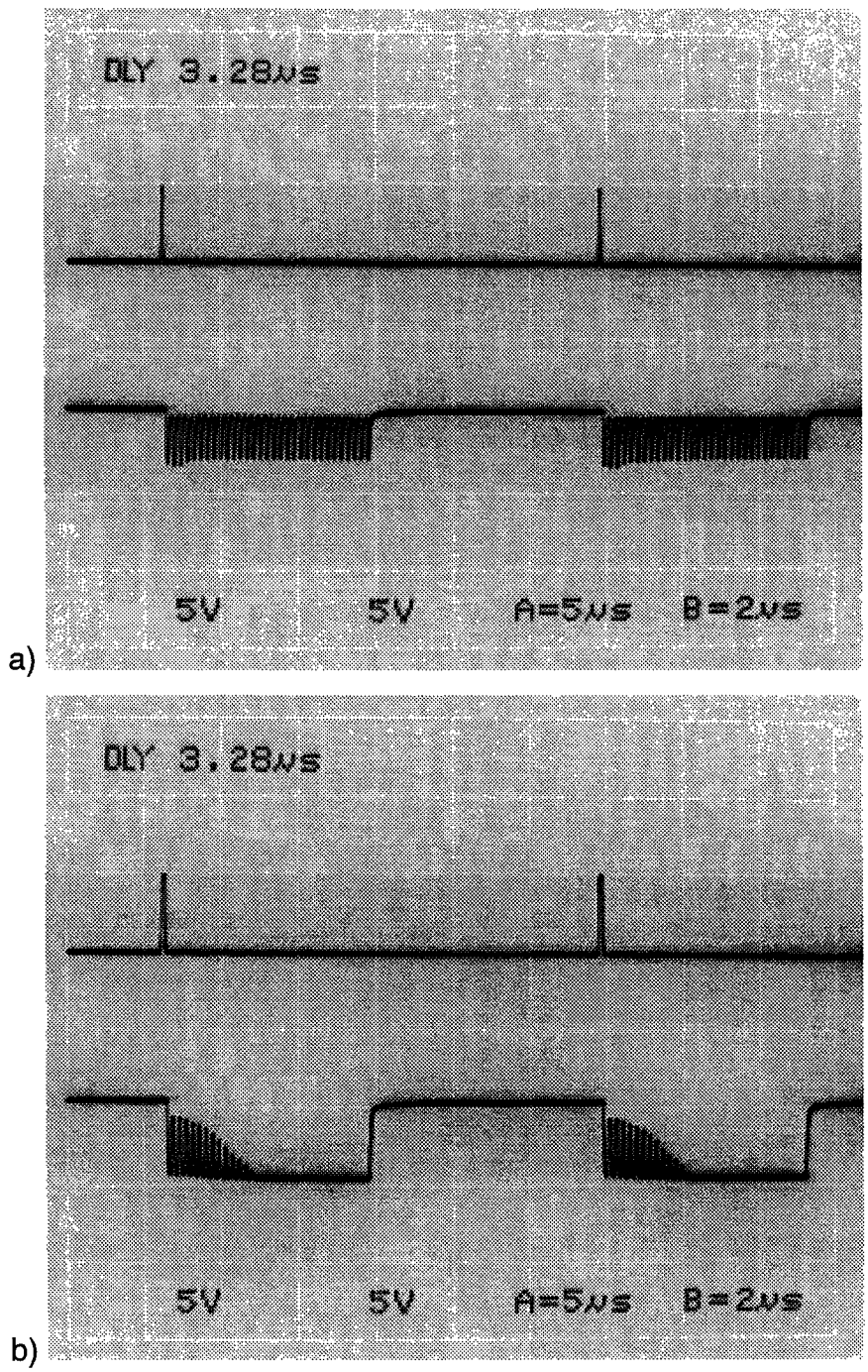

Figure 5-30 Response of the patented flip-flop functionally-equivalent electric circuit to a Reset pulse width of a) 44 ns and b) 96 ns. The feedback loop delay in each case was 150 ns.

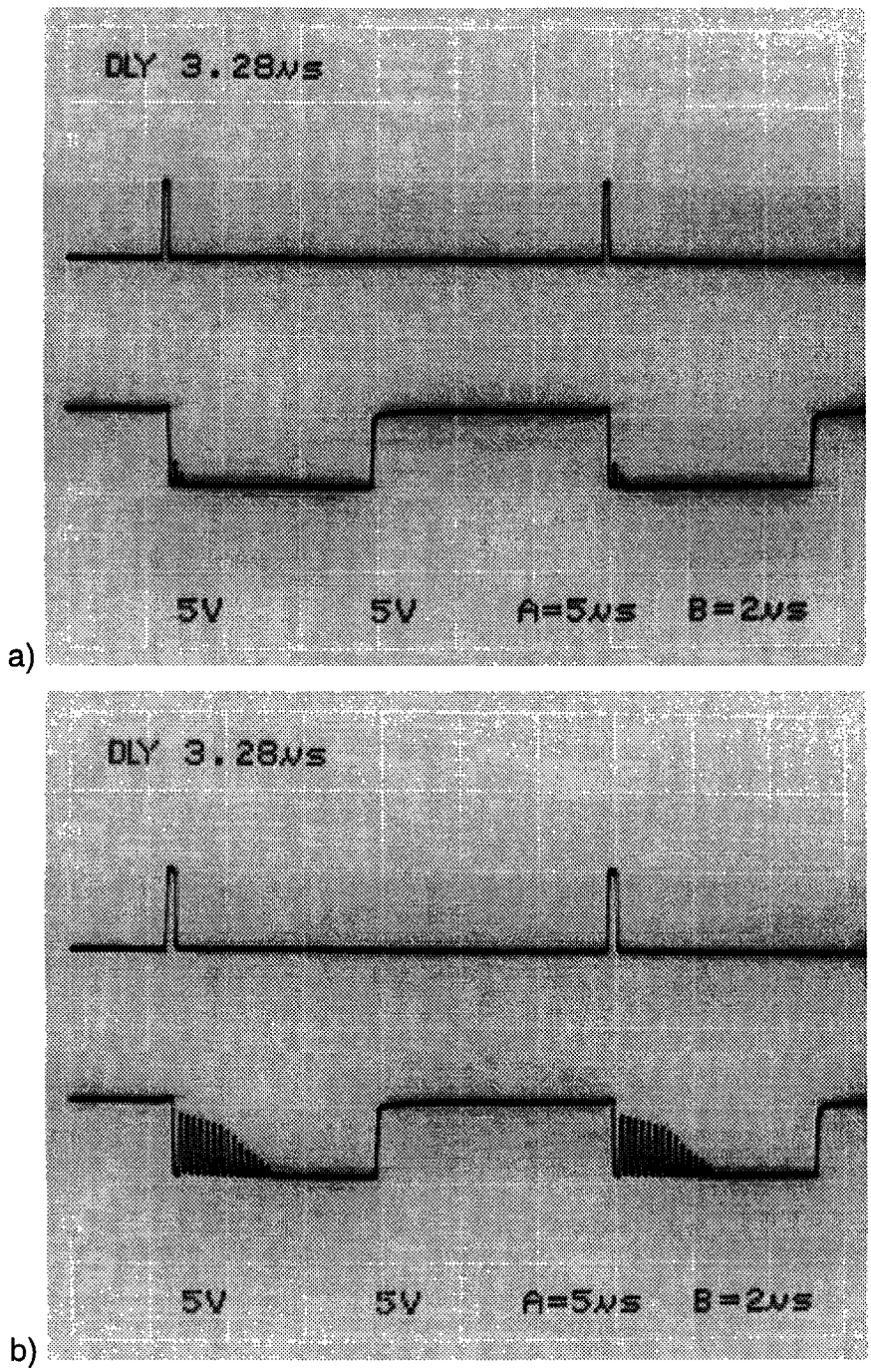

Figure 5-31 Response of the patented flip-flop functionally-equivalent electric circuit to a Reset pulse width of a) 150 ns and b) 210 ns. The feedback loop delay in each case was 150 ns.

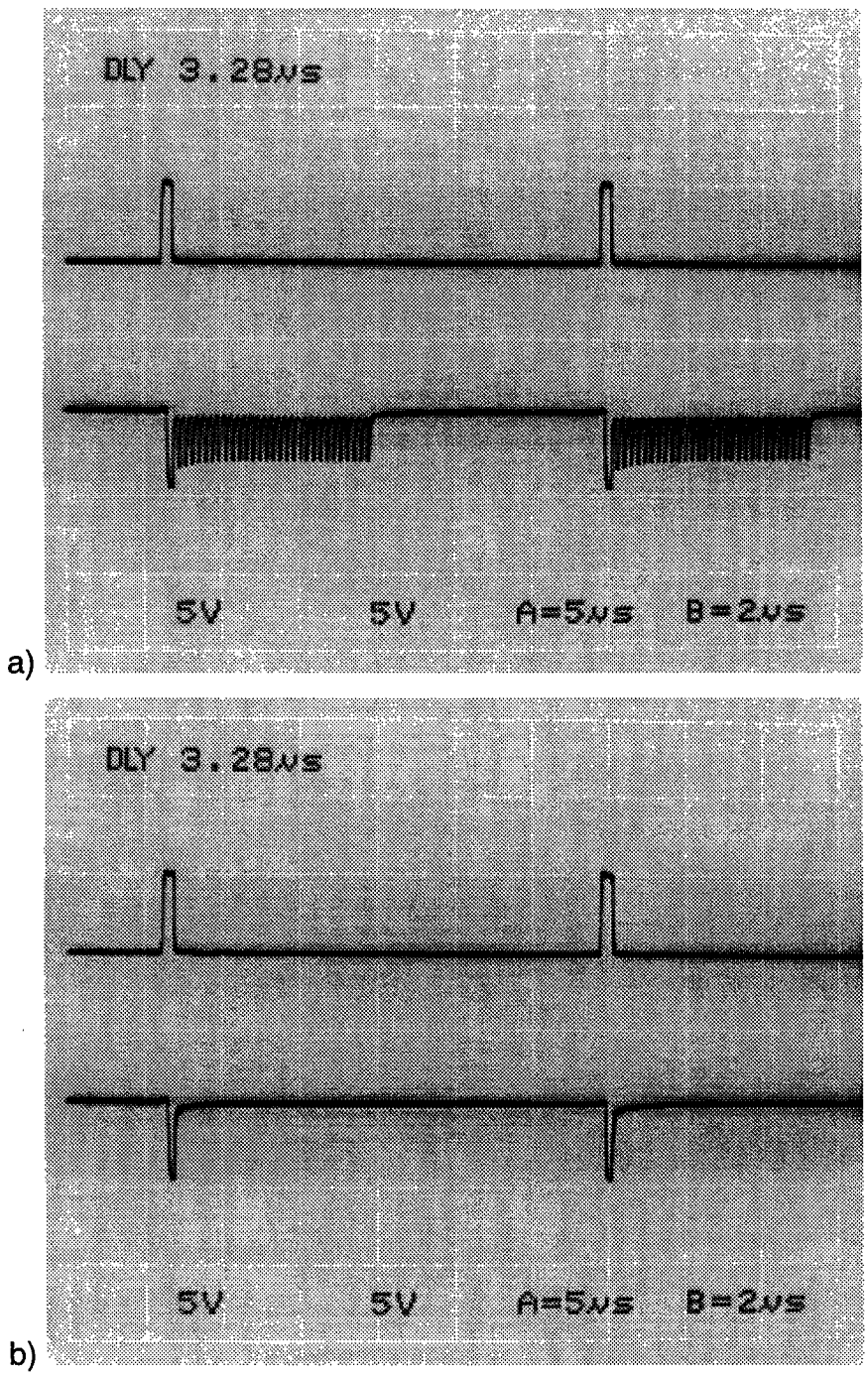

Figure 5-32 Response of the patented flip-flop functionally-equivalent electric circuit to a Reset pulse width of a) 275 ns and b) 311 ns. The feedback loop delay in each case was 150 ns.

waveforms could be easily observed. Figure 5-30 through Figure 5-32 summarize the behavior of the circuit for various durations of the Reset pulse. In each photo of the oscilloscope screen, the upper trace is the Reset; the Set is not shown. The photos summarize the behavior for the case when the Reset is much shorter than the loop delay, to the case when the Reset is double the loop delay.

For a Reset duration much shorter than the loop delay, sustained oscillations are observed (Figure 5-30a). When the Reset is closer to the loop delay, the amplitude of the oscillations decays (Figure 5-30b). The oscillations are a minimum when the Reset pulse duration is equal to the loop delay (Figure 5-31a) and again appear when the Reset duration is increased (Figure 5-31b and Figure 5-32a). When the Reset duration is approximately double the loop delay, it has the effect of resetting the flip-flop and then setting it again (Figure 5-32b). The results here compare well with the simulations of the optical flip-flop shown in Figure 4-13.

Even small deviations of the Reset pulse duration from the loop delay had a significant negative impact on the Output. A deviation of only 17 ns from the ideal value of 150 ns was sufficient for the first oscillation to reach an amplitude of 2.5 V, which was the logic threshold voltage of the circuit. Deviations larger than 17 ns produced oscillation amplitudes greater than 2.5 V, therefore a logic high, meaning that the circuit was no longer functioning as a useful flip-flop. The 17 ns deviation was much shorter than the rise time (10% to 90%) of the digital circuit, which was 45 ns, limited by the protoboard on which the circuit was built. As with the optical circuit, it is expected that a faster response time would increase the required tolerance on the Reset duration.

For comparison to the patented flip-flop, the electrical functionally-equivalent circuit of the proposed flip-flop was built. The schematic is shown in Figure 5-33. In this case the MZI is equivalent to a buffer because only one input is used to control it. The feedback SOA, operated using XGM, is represented by an AND

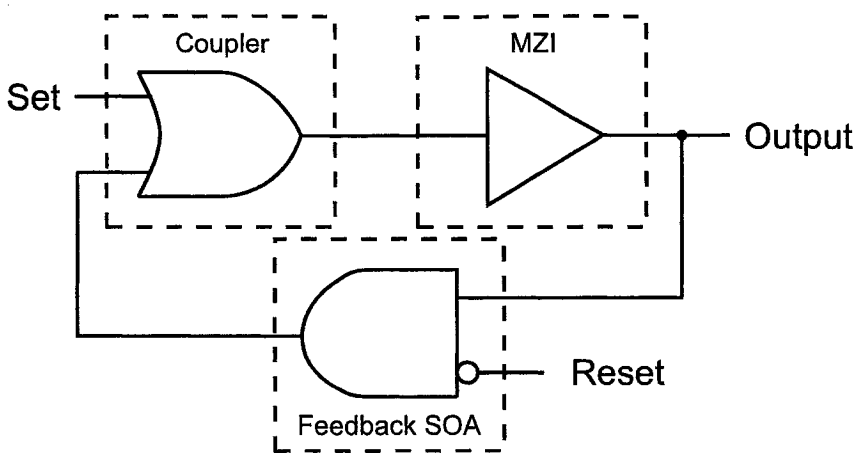

Figure 5-33 Schematic of the electrical circuit that is the functional-equivalent of the proposed flip-flop.

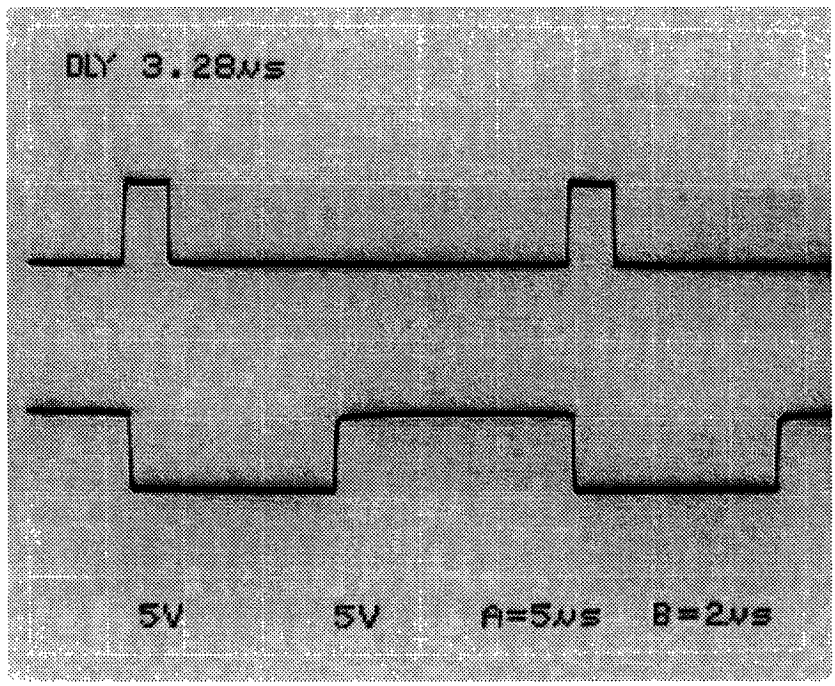

Figure 5-34 Response of the proposed flip-flop functionally-equivalent electric circuit to a Reset pulse width greater than the feedback loop delay.

gate, with the Reset input inverted. Thus, when the Reset is low, the state of the feedback signal passes through to the coupler and when the Reset is high, the coupler sees only a low signal from the feedback loop. The Output of this circuit is shown in Figure 5-34 for a Reset longer than the loop delay. It is clear that the circuit functions properly.

5.6 SUMMARY

This chapter presented experimental verification of the ideas discussed in previous chapters. An all-optical flip-flop was constructed, and its static and dynamic operation was examined. It was shown to operate properly at bit rates of approximately 5 Mb/s, limited by the physical length of the feedback loop in the experimental setup. The rise and fall times of the flip-flop were measured to be approximately 300 ps. It is presumed that the long transition times were due to the low SOA injection currents and the low CW power. By optimizing those parameters and minimizing the length of the feedback loop, operation at bit rates up to a few gigabits per second should be possible. As an example, operation at 2.5 Gb/s (OC-48) would require a feedback loop length of less than 3.5 cm or 8 cm, depending on whether the feedback loop was constructed of indium phosphide or glass, respectively. That bitrate would also require SOA injection currents of approximately 200 mA which is reasonable given that it is within the range of the Altcatel device, specified to be a maximum of 250 mA. The behavior of the flip-flop setup was further explored by investigating critical slowing down.

An all-optical buffer was demonstrated using the same hardware setup as the flip-flop. All-optical writing and clearing of data sequences was shown. The ability to optically rewrite individual data bits, while they circulated in the buffer, was also demonstrated.

Using the MZI-SOA as an inverting amplifier, an all-optical ring oscillator was built and tested. It was shown that the fundamental frequency of the output was determined by the optical delay of the feedback loop, and that the output is a square wave when the rise time of the interferometer is negligible.

Finally, electrical circuits were constructed that were functionally equivalent to the patented and proposed flip-flops. The circuit representing the patented flip-flop exhibited oscillations when the duration of the Reset did not equal the feedback delay, as predicted. The circuit representing the proposed flip-flop did not produce any oscillations when the Reset was longer than the loop delay, also as predicted.

All of these results, including the operation of an all-optical flip-flop, an all-optical buffer, and an all-optical ring oscillator, each using a cross-phase modulated Mach-Zehnder interferometer, are new and have not been reported in the literature by other groups. The electrical-equivalent circuit approach is also original.

CHAPTER

6

CONCLUSIONS

This chapter summarizes the important results of this thesis and the major contributions that were made. Several suggestions for future work are also discussed.

6.1 CONCLUSIONS AND CONTRIBUTIONS

Mach-Zehnder interferometers with semiconductor optical amplifiers in each arm (MZI-SOAs) have enormous potential in the area of digital signal processing in optical communication systems. They offer many potential benefits including gain, good output extinction ratio, high speed, and operate over a wide range of input wavelengths. Considerable experimental work has demonstrated that MZI-SOAs can be used for performing wavelength conversion, logical operations, and demultiplexing. The purpose is to reduce the number of optical and electrical conversions within a network.

The focus of this thesis was to investigate the effect of optical feedback on MZI-SOAs with the goal of providing additional signal processing capabilities. Previous work in this area was limited to a United States patent for a flip-flop [ROBE99b], a design which was recently re-proposed by a second research group [CLAV04]. Those reports provided descriptions of how the flip-flop should

work, however, detailed simulation work or experimental verifications have never been published.

In this thesis, a detailed investigation of the patented flip-flop was performed. Through the use of numerical simulations, it was shown that the design suffered from serious problems that made the device impractical. If the signal to reset the flip-flop was either longer or shorter than the feedback loop delay, oscillations were observed at the output. The problem was that the MZI was being operated in the same manner as an XOR logic gate, with one input being the feedback loop and the other being the reset signal. As in an XOR, both inputs must be at the same logical level to produce a low output. When the reset signal was applied to the flip-flop, the output power of the MZI dropped to a low level. However, to maintain the low output, the reset pulse into the MZI must end at the same time as the low output reaches the other input of the MZI, after having propagated around the feedback loop. It was shown that as the speed of the MZI-SOA increases, so too does the required precision of the reset pulse duration to match the loop delay. Given that input bit periods vary, operation of this flip-flop would be unsuccessful. Another consequence was that a signal to reset, when the device was already reset, caused the device to set itself. While the flip-flop was not built, a functionally-equivalent electric circuit was tested and shown to exhibit the predicted oscillatory behavior. Demonstration of the inoperability of this flip-flop design was the first major contribution of this thesis.

To solve the problem associated with the reset, a second flip-flop was considered. It used a complete hysteresis loop and an optical bias to maintain steady state operation within the range of the hysteresis. Temporary increases and decreases in input power were used to set and reset the flip-flop. It was found to eliminate the oscillating output; however, it was found to suffer from unavoidable critical slowing down when reset. Critical slowing down is of general interest to nonlinear systems, and must be understood for proper operation of any of the feedback designs considered in this thesis. The critical slowing down

was investigated using a simple analysis of the transfer function of the MZI. It was shown mathematically that an MZI with feedback can reach a steady-state operating point in a smooth or oscillating manner, similar to overdamped and underdamped systems. It was also shown that for high speed operation it was necessary to quickly move the dynamic operating point of the flip-flop away from the logic threshold. Experimentally, overdamped and underdamped critical slowing down were demonstrated. As well, it was shown that the severity of the critical slowing down was dependent upon the intensity of the input switching signal. The study of critical slowing down and the dynamic behavior of MZI-SOAs with feedback was a second major contribution to this thesis.

Using the results of the critical slowing down study, it was found that for fast flip-flop operation it was necessary to minimize the feedback optical power when the flip-flop was reset. A third flip-flop design was then introduced and proposed as a practical all-optical flip-flop. It worked by modulating the gain of the feedback loop with the reset signal. Simulations were performed using cross gain modulation in an SOA located in the feedback loop. The design was shown to avoid the problem of critical slowing down, while at the same time eliminating output oscillations. It was demonstrated that restrictions on the reset pulse duration were relaxed, so that any pulse duration greater than the loop delay was acceptable. Further simulations showed that the flip-flop worked properly under a wide range of input signal wavelengths and powers.

A prototype of the flip-flop was constructed and tested. The maximum bitrate of the device was 5 Mbit/s, limited by the long length of the feedback loop. It was suggested that operation to at least 2.5 Gbit/s could be achieved through proper packaging and integration which would reduce the feedback loop length to a few centimeters. The rise and fall times of the flip-flop were measured to be 280 ps and 320 ps, respectively. These times were longer than expected, and assumed to be limited by the low injection currents and the low CW input power into the SOAs of the MZI. It was demonstrated that by increasing both of those

parameters, rise and fall times below 100 ps could be achieved. Unfortunately, a suitable MZI-SOA transfer function could not be found for larger SOA injection currents and a larger CW input powers. Nonetheless, it was suggested that optimization of an MZI should allow high speed operation with a good transfer function. The flip-flop was also found to be noisy, likely another consequence of the low CW input power used. The design of this flip-flop, and its experimental verification, are considered important contributions.

Using the same hardware setup as the flip-flop, a buffer-type memory was experimentally demonstrated. A packet-like sequence of bits was written into the memory and allowed to circulate three times. As with the flip-flop, the data was regenerated with every pass of the feedback loop, and therefore could potentially be stored indefinitely. Data was available to be read from the output once every pass of the feedback loop. Rewriting of certain data bits within the stored data packet was also demonstrated.

This type of buffer memory could potentially be more important than the flip-flop because of the higher potential operating speeds. Unlike the flip-flop, the feedback loop length does not limit the bitrate. Instead the loop length determines how many bits can be stored, with a long loop length capable of storing many bits. The bitrate is determined by the speed of the SOAs. As MZI-SOAs have been demonstrated to work at 10 Gbit/s, the same bitrate could also be expected from the buffer memory. Demonstration of the buffer memory is perhaps the most important contribution of this thesis. It is one of only a few optical memory designs that provide regenerative packet based memory with full optical read/write capabilities. In addition, the fact that it can be used with the NRZ data format is an advantage over existing TOAD memory designs that only work with the RZ data format.

The final major contribution of this thesis dealt with optical-ring oscillators. An inverting MZI-SOA, when combined with optical feedback was shown to produce an oscillating output. Using numerical simulations, and verified through

experimental results, the oscillator was shown to be self-starting, with a oscillation half-period equal to the loop delay. When the response time of the SOAs was small compared to the loop delay, a square wave was observed. The design is interesting because it is capable of producing a high speed optical signal with only DC electrical inputs. The output powers of the two oscillation states (operating points) were determined graphically using the transfer function of the MZI. The stability of the oscillator was investigated using a linear analysis of the transfer function at those operating points. It was shown numerically that when the stability condition was not met, the oscillator output became chaotic.

To summarize, several configurations of MZI-SOAs with feedback were investigated. Both numerical simulations and experimental verification were performed. When the MZI is operated with a noninverting transfer function, optical memory can be constructed, although care must be taken to avoid unwanted behavior. If the MZI produces an inverting transfer function, then self-starting oscillations are possible, provided stability conditions are met.

6.2 FUTURE WORK

There was very little previous work in the area of MZI-SOAs with feedback, so this thesis can be considered only a starting point in this area of study. The flip-flop and especially the buffer memory have potential to be developed into practical devices. The suggestions in this section will focus mostly on the development of those two devices.

An integrated interferometer, such as the Alcatel device used in this thesis is critical for device stability. Further advantages could be obtained by integrating some or all of the feedback loop with the interferometer. This additional integration would be beneficial in terms of performance and manufacturing cost. For instance, in standard single mode fiber the polarization of the light is very

sensitive to fiber motion, but in non-birefringent planar waveguides the polarization of the light does not change, eliminating the need for polarization controllers.

In the case of the flip-flop where a short feedback loop is desirable for high speed operation, integration becomes a necessity. One research group is working on a fully integrated flip-flop based on the patented design, but their work is still in the early stages [pers. comm. Raquel Clavero]. Integration of optical isolators is not possible using standard manufacturing techniques, but this group makes an interesting compromise. They plan to use a non-symmetric coupler at the input to the lower arm of the interferometer. Thus most of the CW light Is guided to the output of the interferometer and clockwise through the feedback loop, with very little light guided counterclockwise through the feedback loop. The isolation is not complete but might be sufficient. If this method was used in the proposed flip-flop, isolation would still be required to prevent the Reset from reaching the interferometer. This could be achieved by simply dictating that the Reset not be at the same wavelength as the CW input and using a filter to separate the two wavelengths.

It would be beneficial to reduce the noise and increase the speed of the MZI. As discussed in previous chapters, having greater flexibility to generate step-like MZI transfer functions will help in this regard. The next few suggestions are ways to achieve those goals.

The Alcatel MZI used in this thesis was an all-active device with simple segmented electrodes used to define the various independently controllable regions. It is generally believed that a hybrid active-passive MZI, with discrete SOAs in each arm and otherwise passive waveguides, would be superior to an all-active MZI. For instance, unwanted gain saturation effects in the waveguides would be avoided, and noise due to spontaneous emission and ASE would be reduced. These improvements would benefit all of the designs in this thesis. There are research groups developing these hybrid MZIs. It would be interesting

to compare experimental results of a flip-flop or a buffer memory using a hybrid MZI with results using an all-active MZI.

Another limitation of the Alcatel MZI was its equal arm lengths. An initial π phase difference between the arms was created by electrically biasing the arms differently. Unfortunately, this also had the effect of making the optical powers unequal at the output coupler, limiting the output extinction ratio of the MZI transfer function. Technically, it is no more difficult to make the arm lengths unequal, however, this would allow, in the design stage, the power and phase of each arm to be optimized independently. Improved transfer functions would be possible, and for noninverting transfer functions, increased extinction ratios could be obtained. An improved extinction ratio would permit a smaller gain in the feedback loop to be used. This, in turn, would reduce ASE produced by the feedback SOA, thus reducing the overall noise level in the flip-flop or buffer memory.

Commercial MZI-SOAs are designed for use as wavelength converters and must make certain assumptions. As examples, the input signal polarizations are assumed to be unknown and the CW wavelength is assumed to be variable depending on what wavelength the signal is being converted to. If the MZI is used as part of a memory element in a router, these assumptions may no longer apply. For example, the input signals may be locally generated and their polarizations known. In this way a polarization insensitive MZI is not required, simplifying the design and reducing the cost. As another example, in most optical router designs, there is wavelength conversion at the output stage. Thus, for operation inside the router, the CW wavelength can be fixed, and the transfer function of the MZI can be optimized for that wavelength.

Another way to improve the transfer function would be to add an optical limiter in the feedback loop. If treated as a part of the MZI black-box, this would have the effect of stretching out the upper part of the transfer function, making it flatter. This would improve the noise performance and allow the memory to

operate over a larger input extinction ratio. Such a limiter can be constructed using an SOA structure inside a multimode interference coupler [DEME02], and could possibly be combined with the feedback SOA.

In addition to improving the proposed flip-flop and buffer memory designs, experimental testing of the patented flip-flop would be interesting. Packaging of the Alcatel MZI used in this thesis allowed only one arm of the interferometer to be accessed with an input signal. Because of this, the patented design could not be tested to verify the true sensitivity of the design to the duration of the feedback pulse. However, MZIs with access to both input waveguides exist, as they are necessary to perform differential XPM experiments, so one of these could be used to carry out this experiment.

All of the designs in this thesis consider only a single MZI with a single feedback loop to one of the input ports. Other designs may offer additional functionality. One example would be to use differential XPM and two feedback loops to build an improved ring oscillator. Differential XPM can create very short pulses. The duration of an output pulse is dictated by the delay between two input pulses. By using two feedback loops, with slightly different lengths, a short-pulse generator may be possible. Thus the pulse repetition rate, but not the pulse duration, is limited by the length of the feedback loop. For higher pulse repetition rates, the output pulse train can be interleaved. A similar design was recently reported [HILL03], but it used a passive MZI and required an initial input square wave to seed to pulse generator. Pulses as short as 1 ps were obtained. Similar pulsewidths should be possible from this proposed design. Similar use of differential XPM might also benefit the buffer memory design.

REFERENCES

[ADAM95] M.J. Adams, D.A.O. Davies, M.C. Tatham, M.A. Fisher, "Nonlinearities in Semiconductor Laser Amplifiers", *Optical and Quantum Electronics*, vol. 27, pp. 1-13, 1995.

[AGRA86] G.P. Agrawal and N.K. Dutta, *Long Wavelength Semiconductor Lasers*, Van Nostrand Reinhold, New York, 1986.

[AGRA88] G. Agrawal, "Population Pulsations and Nondegenerate Four-Wave Mixing in Semiconductor Lasers and Amplifiers", *J. Opt. Soc. Am. B.*, vol. 5, no. 1, pp. 147-159, Jan. 1988.

[AGRA89] G.P. Agrawal and N.A. Olsson, "Self-Phase Modulation and Spectral Broadening of Optical Pulses in Semiconductor Laser Amplifiers", *IEEE J. of Quantum Electron.*, vol. 25, no. 11, pp. 2297-2306, Nov. 1989.

[AGRA92] G. Agrawal, *Fiber-Optic Communications Systems*, John Wiley & Sons, Toronto, 1992.

[AGRA95] G. Agrawal, *Semiconductor Lasers: Past, Present, and Future*, AIP Press, American Institute of Physics, Woodbury, New York, 1995.

[AMD01] AMD Announces World's Fastest CMOS Transistors [online]. http://www.amd.com/us-en/Corporate/VirtualPressRoom/0,,51_104_543_4493~13001,00.html [2001, 3 December].

[ASGH97] M. Asghari, I.H. White, and R.V. Plenty, "Wavelength Conversion Using Semiconductor Optical Amplifiers", *IEEE J. Light. Tech.*, vol. 15, no. 7, pp. 1181-1190, Jul. 1997.

[BARE02] E.L.G. Barefoot, *A Proposal for All-Optical Packet Routing*, Master's of Applied Science Thesis, Dalhousie University, Halifax, Nova Scotia, Canada, 2002.

[BARE03] E. Barefoot, M. Cada, and L. Hughes, "Novel Approach to All-Optical Packet Routing", *Proceedings of SPIE Vol. 5445*, Microwave and Optical Technology 2003, Ostrava, Czech Republic, pp. 14-19, 2003.

[BLUM00] D.J. Blumenthal, B-E. Olsson, G. Rossi, T.E. Dimmick, L. Rau, M. Mašanović, O. Lavrova, R. Doshi, O. Jerphagnon, J.E Bowers, V. Kaman, L.A. Coldren, and J. Barton, "All-Optical Label Swapping Networks and Technologies", *IEEE J. Light. Tech.*, vol. 18, no. 12, pp. 2058-2075, Dec. 2000.

[CAO03] S.-C. Cao, *Wavelength Converters Based on Semiconductor Optical Amplifiers*, Doctor of Philosophy Thesis, Queen's University, Kingston, Ontario, Canada, 2003.

[CLAV04] R. Clavero, J.M. Martínez, F. Ramos, and J. Martí, "All-Optical Packet Routing Scheme for Optical Label-Swapping Networks", *Optics Express*, OSA, vol. 12, no. 18, pp. 4326-4332, Sept. 2004.

[CNN03] CNN-Reuters (2003) New Processor Computes at Light Speed, [online]. Available: http://www.cnn.com/2003/TECH/ptech/10/31/israel.lenslet.reut/ [2005, 11 July].

[CONN02] M.J. Connelly, *Semiconductor Optical Amplifiers*, Kluwer Academic Publishers, Boston, 2002.

[DANI98] S.L. Danielsen, P.B. Hansen, and K.E. Stubkjaer, "Wavelength Conversion in Optical Packet Switching", *IEEE J. Light. Tech.*, vol. 16, no. 12, pp. 2095-2108, Dec. 1998.

[DAVI95] D.A.O. Davies "Small-Signal Analysis of Wavelength Conversion in Semiconductor Laser Amplifiers via Gain Saturation", *IEEE Photon. Tech. Lett.*, vol. 7, no. 6, pp. 617-619, June 1995.

[DEME02] J. De Merlier, G. Morthier, S. Verstuyft, T. Van Caenegem, I. Moerman, P. Van Daele, R. Baets, "Experimental Demonstration of All-Optical Regeneration Using an MMI-SOA", *IEEE Photon. Tech. Lett.*, vol. 14, no. 5, pp. 660-662, May 2002.

[DURH94] T. Durhuus, C. Joergensen, B. Mikkelsen, R.J.S. Pedersen, and K.E. Stubkjaer, "All Optical Wavelength Conversion by SOA's in a Mach-Zehnder Configuration", *IEEE Photon. Tech. Lett.*, vol. 6, no. 1, pp. 53-55, Jan. 1994.

[DURH96] T. Durhuus, B. Mikkelsen, C. Joergensen, S.L. Danielsen, and K.E. Stubkjaer, "All-Optical Wavelength Conversion by Semiconductor Optical Amplifiers", *IEEE J. Light. Tech.*, vol. 14, no. 6, pp. 942-954, Jun. 1996.

[EISE92] M. Eiselt, "Optical Loop Mirror with Semiconductor Laser Amplifier", *IEEE Electron. Lett.*, vol. 28, no. 16, pp. 1505-1507, Jul. 1992.

[EISE95] M. Eiselt, W. Pieper, and H.G. Weber, "SLALOM: Semiconductor Laser Amplifier in a Loop Mirror", *IEEE J. Light. Tech.*, vol. 13, no. 10, pp. 2099-2112, Oct. 1995.

[FISC00] S. Fischer, M. Dülk, E. Gamper, W. Vogt, W. Hunziker, E. Gini, H. Melchoir, A. Buxens, H.N. Poulsen, and A.T. Clausen, "All-Optical Regenerative OTDM Add-Drop Multiplexing at 40 Gb/s Using Monolithic InP Mach-Zehnder Interferometer", *IEEE Photon. Tech. Lett.*, vol. 12, no. 3, pp. 335-338, Mar. 2000.

[FAN98] R. Fan, and R.B. Hooker, "Hybrid Optical Switch Using Polymer Waveguides and Semiconductor Optical Amplifiers (SOAs)", *IEEE Electronic Components and Technology Conference*, pp. 1006-1011, May 1998.

[FJEL00a] T. Fjelde, D. Wolfson, A. Kloch, B. Dagens, A. Coquelin, I. Guillemot, F. Gaborit, F. Poingt, M. Renaud, "Demonstration of 20 Gbit/s All-Optical Logic XOR in Integrated SOA-Based Interferometric Wavelength Converter", *IEEE Electron. Lett.*, vol. 36, no. 22, pp. 1863-1864, Oct. 2000.

[FJEL00b] T. Fjelde, D. Wolfson, A. Kloch, C. Janz, A. Coquelin, I. Guillemot, F. Gaborit, F. Poingt, B. Dagens, M. Renaud, "10 Gbit/s All-Optical Logic OR in Monolithically Integrated Interferometric Wavelength Converter", *IEEE Electron. Lett.*, vol. 36, no. 9, pp. 813-815, Apr. 2000.

[HAMI02] A. Hamié, A. Sharaiha, M. Guégan, and B. Pucel, "All-Optical Logic NOR Gate Using Two-Cascaded Semiconductor Optical Amplifiers", *IEEE Photon. Tech. Lett.*, vol. 14, no. 10, pp. 1439-1441, Oct. 2002.

[HILL01] M.T. Hill, H. de Waardt, G.D. Khoe, and H.J.S. Dorren, "Fast Optical Flip-Flop by use of Mach-Zehnder Interferometers", *Micro. and Optical Tech. Lett.*, vol. 31, no. 6, pp. 411-415, Dec. 2001.

[HILL03] M.T. Hill, H. de Waardt, G.D. Khoe, and H.J.S. Dorren, "Short-Pulse Generation in Interferometers Employing Semiconductor Optical Amplifiers", *IEEE J. Quantum Electron.*, vol. 39, no. 7, pp. 886-896, Jul. 2003.

[HOFF99] M. Hoffmann, P. Kopka, and E. Voges, "All-Silicon Bistable Micromechanical Fiber Switch Based on Advanced Bulk Micromachining", *IEEE J. Sel. Topics in Quantum Electron.*, vol. 5, no. 1, pp. 46-51, Jan./Feb. 1999.

[HONG99] X. Hong, Y. Chen, J. Lin, "Erasable Fiber Loop Optical Buffer", Fifth Asia-Pacific Conference on Communications and Fourth Optoelectronics and Communications Conference (APCC/OECC '99), vol. 2, pp. 1406-1409, Oct. 1999.

[HORO89] P. Horowitz, and W. Hill, *The Art of Electronics*, Cambridge University Press, Cambridge, 1989.

[HUNT98] D.K. Hunter, M.C. Chia, and I. Andonovic, "Buffering in Optical Packet Switches", *IEEE J. Light. Tech.*, vol. 16, no. 12, pp. 2081-2094, Dec. 1998.

[ISLA02] M.N. Islam, "Raman Amplifiers for Telecommunications", *IEEE J. Sel. Topics in Quantum Electron.*, vol. 8 no. 3, pp. 548-559, May 2002.

[JOER97] C. Joergensen, S.L. Danielsen, K.E. Stubkjaer, M. Schilling, K. Daub, P. Doussiere, F. Pommereau, P.B. Hansen, H.N. Poulsen, A. Kloch, M. Vaa, B. Mikkelsen, E. Lach, G. Laube, W. Idler, and K. Wunstel, "All-Optical Wavelength Conversion at Bit Rates Above 10 Gb/s Using Semiconductor Amplifiers", *IEEE J. Sel. Topics in Quantum Electron.*, vol. 3, no. 5, pp. 1168-1180, Oct. 1997.

[JOUR01] A. Jourdan, D. Chiaroni, E. Dotaro, G.J. Eilenberger, F. Masetti, M. Renaud, "The Perspective of Optical Packet Switching in IP-Dominant Backbone and Metropolitan Networks", *IEEE Comm. Mag.*, vol. 39, no. 3, pp. 136-141, Mar. 2001.

[KANG00] B.K. Kang, J.H. Kim, Y.H. Park, S. Lee, Y.M. Jhon, D.H. Woo, S.H. Kim, and S.H. Park, "All-Optical Logic AND in a SOA-Based Mach-Zehnder All-Optical Wavelength Converter", *Lasers and Electro-Optics Society 2000 Annual Meeting*, IEEE LEOS 13th Annual Meeting, vol. 1, pp. 117-118, Nov. 2000.

[KAWA94] H. Kawaguchi, *Bistabilities and Nonlinearities in Laser Diodes*, Artech House, Boston, 1994.

[KAWA97] H. Kawaguchi, "Bistable Laser Diodes and Their Applications: State of the Art", *IEEE J. Sel. Topics in Quantum Electron.*, vol. 3, no. 5, pp. 1254-1270, Oct. 1997.

[KAWA98] H. Kawaguchi and Y. Yamayoshi, "Ultrafast polarization bistable switching in a vertical-cavity surface-emitting laser and its applications", Conference on Lasers and Electro-Optics 1998 (CLEO 98), pp. 439-440, May 1998.

[LACE97] J.P.R. Lacey, M.A. Summerfield, and S.J. Madden, "Tunability of Polarization-Insensitive Wavelength Converters Based on Four-Wave Mixing in Semiconductor Optical Amplifiers", *IEEE J. Light. Tech.*, vol. 16, no. 12, pp. 2419-2427, Dec. 1998.

[LANE00] P. Lane and M. Cada, "Interferometric Optical Fourier-Transform Processor for Calculation of Selected Spatial Frequencies", *Applied Optics*, vol. 39, no.35, pp. 6573-6586, Dec. 2000.

[LAVI98] B. Lavigne, D. Chiaroni, L. Hamon, C. Janz, and A. Jourdan, "Experimental Analysis of SOA-Based 2R and 3R Optical Regeneration for Future WDM Networks", *Optical Fiber Communication Conference and Exhibit*, pp. 324-325, Feb. 1998.

[LEE02] S. Lee, J. Park, K. Lee, D. Eom, S. Lee, and J.H. Kim, "All-Optical Exclusive NOR Logic Gate Using Mach-Zehnder Interferometer", *Jpn. J. Appl. Phys.*, vol. 41, pt. 2, no. 10B, pp. L1155-L1157, Oct. 2002.

[LEUT98] J. Leuthold, P. Besse, J. Eckner, E. Gamper, M. Dulk, and H. Melchior, "All-Optical Space Switches with Gain and Principally Ideal Extinction Ratios", *IEEE J. Quantum Electron.*, vol. 34, no. 4, pp. 622-633, Apr. 1998.

[MANN99] R.J. Manning, I.D. Phillips, A.D. Ellis, A.E. Kelly, A.J. Poustie, and K.J. Blow, "10 Gbit/s All-Optical Regenerative Memory Using Single SOA-Based Logic Gate", *IEEE Electron. Lett.*, vol. 35, no. 2, pp. 158-159, Jan. 1999.

[MARC96] D.D. Marcenac, A.E. Kelly, D. Nesset and D.A.O. Davies, "Bandwidth Enhancement of Wavelength Conversion via Cross-Gain Modulation by Semiconductor Optical Amplifier Cascade", *IEEE Electron. Lett.*, vol. 31, no. 17, pp. 1442-1443, Aug. 1995.

[MARC97] D. Marcenac and A. Mecozzi, "Switches and Frequency Converters Based on Cross-Gain Modulation in Semiconductor Optical Amplifiers", *IEEE Photon. Tech. Lett.*, vol. 9, no. 6, pp. 749-751, Jun. 1997.

[MASE93] F. Masetti, P. Gavignet-Morin, D. Chiaroni, G. Da Loura, "Fiber Delay Lines Optical Buffer for ATM Photonic Switching Applications", IEEE INFOCOM '93, Proceedings of the Twelfth Annual Joint Conference of the IEEE Computer and Communications Societies, vol. 3, pp. 935-942, Mar. 1993.

[MECO96] A. Mecozzi, "Small-Signal Theory of Wavelength Converters Based on Cross-Gain Modulation in Semiconductor Optical Amplifiers", *IEEE Photon. Tech. Lett.*, vol. 8, no. 11, pp. 1471-1473, Nov. 1996.

[MIDW93] J.E. Midwinter, *Photonics in Switching, Volume 1, Background and Components*, Academic Press Inc., Toronto, 1993.

[MIKK94] B. Mikkelsen, T. Durhuus, C. Joergensen, R.J.S. Pedersen, C. Braagaard, and K.E. Stubjaer, "Polarization Insensitive Wavelength Conversion of 10 Gbit/s Signals with SOAs in a Michelson Interferometer", *IEEE Electron. Lett.*, vol. 30, no. 3, pp. 260-261, Feb. 1994.

[MIKK97] B. Mikkelsen, K.S. Jepsen, M. Vaa, H.N. Poulsen, K.E. Stubkjaer, R. Hess, M. Duelk, W. Vogt, E. Gamper, E. Gini, P.A.Besse, H. Melchoir, S. Bouchoule, and F. Devaux, "All-Optical Wavelength Converter Scheme for High Speed RZ Signal Formats", *IEEE Electron. Lett.*, vol. 33, no. 25, pp. 2137-2139, Dec. 1997.

[MORI96] T. Morioka, H. Takara, S. Kawanishi, K. Uchiyama, and M. Saruwatari, "Polarization-Independent All-Optical Demultiplexing up to 200 Gbit/s Using Four-Wave Mixing in a Semiconductor Laser Amplifier", *IEEE Electron. Lett.*, vol. 32, no. 9, pp. 840-842, Apr. 1996

[MWAR92] E. Mwarania and J. Wilinson, "Modleing of Y-Junction Waveguide Resonators", *IEEE J. Light. Tech.*, vol. 10, no. 11, pp. 1700-1707, Nov. 1992.

[NAKA94] S. Nakamura, K. Tajima, and Y. Sugimoto, "Experimental Investigation on High-Speed Switching Characteristics of a Novel Symmetric Mach-Zehnder All-Optical Switch", *Appl. Phys. Lett.*, vol. 65, no. 3, pp. 283-285, Jul. 1994.

[NESS94] D. Nesset, M.C. Tatham, L.D. Westbrook, and D. Cotter, "Degenerate Wavelength Operation of an Ultrafast All-Optical AND Gate using Four Wave Mixing in a Semiconductor Laser Amplifier", *IEEE Electron. Lett.*, vol. 30, no. 23, pp. 1938-1940, Nov. 1994.

[NISH85] H. Nishihara, M Haruna, and T. Suhara, *Optical Integrated Circuits*, McGraw-Hill Book Company, Montreal, 1985.

[NUTT03] S. Nutter, *Signal Processing Applications of Semiconductor Optical Amplifiers*, Master's of Applied Science Thesis, Dalhousie University, Halifax, Nova Scotia, Canada, 2003.

[OBER97] K. Obermann, S. Kindt, D. Breuer, K. Petermann, C. Schmidt, S. Diez, and H.G. Weber, "Noise Characteristics of Semiconductor-Optical Amplifiers Used for Wavelength Conversion via Cross-Gain and Cross-Phase Modulation", *IEEE Photon. Tech. Lett.*, vol. 9, no. 3, pp. 312-314, Mar. 1997.

[ODAG89] T. Odagawa and S. Yamakoshi, "Optical Set-Reset Operations of Bistable Laser Diode with Single-Wavelength Light," *IEEE Electron. Lett.*, vol. 25, no. 21, pp. 1428-1429, Sept. 1989.

[OLSS92] N.A. Olsson, "Semiconductor Optical Amplifiers", *Proc. IEEE*, vol. 80, no. 3, pp. 375-382, Mar. 1992.

[OMAH88] M.J. O'Mahony, "Semiconductor Laser Amplifiers for Use in Future Fiber Systems", *IEEE J. Light. Tech.*, vol. 6, no. 4, pp. 531-544, Apr. 1988.

[OSIN87] M. Osiński and J. Buus, "Linewidth Broadening Factor in Semiconductor Lasers – An Overview", *IEEE J. Quantum Electron.*, vol. 23, no. 1, pp. 9-29, Jan. 1987.

[PAN95] X. Pan, J.M. Wiesenfeld, J.S. Perino, T.L. Koch, G. Raybon, U. Koren, M. Chien, M. Young, B.I. Miller, and C.A. Burrus, "Dynamic Operation of a Three-Port, Integrated Mach-Zehnder Wavelength Converter", *IEEE Photon. Tech. Lett.*, vol. 7, no. 9, pp. 995-997, Sep. 1995.

[POUS96] A. Poustie, R.J. Manning, and K.J. Blow, "All-Optical Circulating Shift Register Using a Semiconductor Optical Amplifier in a Fiber Loop Mirror", *IEEE Electron. Lett.*, vol. 32, no. 13, pp. 1215-1216, Jun. 1996.

[POUS97] A.J. Poustie, K.J. Blow, and R.J. Manning, "All-Optical Regenerative Memory for Long Term Data Storage", *Optics Communications*, vol. 140, pp. 184-186, Aug. 1997.

[POUS98a] A.J. Poustie, A.E. Kelly, R.J. Manning, and K.J. Blow, "All-Optical Regenerative Memory with Full Write/Read Capability", *Optics Communications*, vol. 154, pp. 277-281, Sept. 1998.

[POUS98b] A. Poustie, K.J. Blow, A.E. Kelly, and R.J. Manning, "All-Optical Binary Half-Adder", *Optics Communications*, vol. 156, pp. 22-26, Nov. 1998.

[POUS00] A. Poustie, R.J. Manning, A.E. Kelly, and K.J. Blow, "All-Optical Binary Counter", *Optics Express*, vol. 6, no. 3, pp. 69-74, Jan. 2000.

[RATO95] F. Ratovelomanana, N. Vodjdani, A. Enard, G. Glastre, D. Rondi, R. Blondeau, C. Joergensen, T. Durhuus, B. Mikkelsen, K.E. Stubkjaer, A. Jourdan, and G. Soulage, "An all-optical Wavelength-converter with semiconductor optical amplifiers monolithically integrated in an asymmetric passive Mach-Zehnder interferometer", *IEEE Photon. Tech. Lett.*, vol. 7, no. 10, pp. 992-994, Oct. 1995.

[RATO97] F. Ratovelomanana, N. Vodjdani, A. Enard, G. Glastre, D. Rondi, R. Blondeau, A. Dupas, L. Billès, and J.C. Simon, "Regeneration Improvement in All-Optical Wavelength Converter, Based on a Mach-Zehnder Interferometer, by means of a Phase-Shifter Section", *Electron. Lett.*, vol. 33, no. 19, pp. 1629-30, Sept. 1997.

[ROBE99a] K.B. Roberts, J.E.A. Whiteaway, and M. Tait, *Optical Logic Devices and Methods*, United States patent 5,999,283, Dec. 7, 1999.

[ROBE99b] K.B. Roberts, *Optical Detection and Logic Devices with Latching Function*, United States patent 5,999,284, Dec. 7, 1999.

[SALE91] B.E.A. Saleh and M.C. Teich, *Fundamentals of Photonics*, Wiley-Interscience, John-Wiley & Sons Inc., Toronto, 1991.

[SANC91] F. Sanchez, "Matrix Algebra for All-Fibre Optical Resonators", *IEEE J. Light. Tech.*, vol. 9, no. 7, pp. 838-844, Jul. 1991.

[SATO04] R. Sato, K. Magari, I. Ogawa, Y. Inoue, R. Kasahara, M. Okamoto, Y. Tohmori, and Y. Suzuki, "10-Gb/s Low-Input-Power SOA-PLC Hybrid Integrated Wavelength Converter and Its 8-Slot Unit", *IEEE J. Light. Tech.*, vol. 22, no. 5, pp. 1331-1337, May 2004.

[SCHI94] M. Schilling, K. Daub, W. Idler, D. Baums, U. Koerner, E. Latch, G. Laube, and K. Wünstel, "Wavelength Converter Based on Integrated All-Active Three-Port Mach-Zehnder Interferometer", *IEEE Electron. Lett.*, vol. 30, no. 25, pp. 2128-2130, Dec. 1994.

[SOKO93] J.P. Sokoloff, P.R. Prucnal, I. Glesk, and M. Kane, "A Terahertz Optical Asymmetric Demultiplexer (TOAD)", *IEEE Photon. Tech. Lett.*, vol. 5, no. 7, pp. 787-790, Jul. 1993.

[SOTO99] H. Soto, D. Erasme, and G. Guekos, "Cross-Polarization Modulation in Semiconductor Optical Amplifiers", *IEEE Photon. Tech. Lett.*, vol. 11, no. 8, pp. 970-972, Aug. 1999.

[SPIE98] L.H. Spiekman, "Progress in Integrated Devices for Wavelength Conversion", *IEEE Lasers and Electro-Optics Society Annual Meeting*, vol. 2, pp. 259 -260, Dec. 1998.

[STAR99] M. Starzomski, *Characterization and Application of a Phase Modulating Liquid Crystal Display*, Master of Applied Science Thesis, Dalhousie University, Halifax, Nova Scotia, Canada, 1999.

[STUB00] K.E. Stubkjaer, "Semiconductor Optical Amplifier-Based All-Optical Gates for High-Speed Optical Processing", *IEEE J. Sel. Topics in Quantum Electron.*, vol. 6, no. 6, pp. 1428-1435, Nov./Dec. 2000.

[TAJI93] K. Tajima, "All-Optical Switch with Switch-Off Time Unrestricted by Carrier Lifetime", *Jpn. J. Appl. Phys.*, vol. 32, pt. 2, no. 12A, pp. L1746-L1749, Dec. 1993.

[TAKE04] M. Takenaka and Y. Nakano, "Realization of an All-Optical Flip-flop using Directionally Coupled Bistable Laser Diode", *IEEE Photon. Tech. Lett.*, vol. 16, no. 1, pp. 45-47, Jan. 2004.

[TOMI86] A. Tomita, T. Terakado, and A. Suzuki, "Turn-Off Characteristics of Bistable Laser Diode", *J. Appl. Phys.*, vol. 59, no. 6, pp. 1839-1842, Mar. 1986.

[UENO96] H. Uenohara, R. Takahashi, Y. Kawamura, and H. Iwamura, "Static and Dynamic Response of Multi-Quantum-Well Voltage-Controlled Bistable Laser Diodes", *IEEE J. Quantum Electron.*, vol. 32, no. 5, pp. 873-883, May 1996.

[USKO94] A. Uskov, J. Mørk, and J. Mark, "Wave Mixing in Semiconductor Laser Amplifiers Due to Carrier Heating and Spectral-Hole Burning", *IEEE J. Quantum Electron.*, vol. 30, no. 8, pp. 1769-1781, Aug. 1994.

[VAHA97] K. Vahala, R. Paiella, and G. Hunziker, "Ultrafast WDM Logic", *IEEE J. Sel. Topics in Quantum Electron.*, vol. 3, no. 2, pp. 698-701, Apr. 1997.

[VAND99] R. Van Dommelen, *Bistable Distributed Feedback Laser Diodes*, Master's of Applied Science Thesis, Dalhousie University, Halifax, Nova Scotia, Canada, 1999.

[VAND00a] R. Van Dommelen and M. Cada, "Theory of Four-Wave Mixing in Semiconductor Optical Amplifiers", Report for the Canadian Institute for Photonic Innovations, Mar. 2000.

[VAND00b] R. Van Dommelen and M. Cada, "All-Optical Logic Using SOA Wavelength Converters", Report for the Canadian Institute for Photonic Innovations, Oct. 2000.

[VAND01] R. Van Dommelen and M. Cada, "Cross-Gain and Cross-Phase Modulation in Semiconductor Optical Amplifier Wavelength Converters", Unpublished Report for the Canadian Institute for Photonic Innovations, Apr. 2001.

[VAND02] R. Van Dommelen and M. Cada, "Semiconductor Optical Amplifier Mach-Zehnder Interferometers with Feedback", *Nonlinear Guided Waves Conference*, OSA, Stresa, Italy, 2002.

[VAND03] R. Van Dommelen, S. Nutter, and M. Cada, "All-Optical Regenerators and Latches", *Proceedings of SPIE Vol. 5445*, Microwave and Optical Technology 2003, Ostrava, Czech Republic, pp. 91-94, 2003.

[WALL01] S.G. Wallace, *InGaAsP/GaAs Quantum Well Lasers: Material Properties, Laser Design and Fabrication, Ultrashort Pulse External Cavity Operation*, Doctor of Philosophy Thesis, McMaster University, Hamilton, Ontario, Canada, 2001.

[WANG97] J.-Y. Wang, M. Cada, R. Van Dommelen, and T. Makino, "Dynamic Characteristics of Bistable Laser Diodes", *IEEE J. of Sel. Topics in Quantum Electron.*, vol. 3, no. 5, pp. 1271-1279, Oct. 1997.

[WANG00] C.C. Wang, M.A. Summerfield, R.S. Tucker, "Performance of Cascaded Wavelength Converters", *Lasers and Electro-Optics Society 2000 Annual Meeting*, IEEE LEOS 2000 13th Annual Meeting, vol. 2, pp. 631-632, Nov. 2000.

[WILL95] A.E. Willner and W. Shieh, "Optimal Spectral and Power Parameters for All-Optical Wavelength Shifting: Single Stage, Fanout, and Cascadability", *IEEE J. Light. Tech.*, vol. 13, no. 5, pp. 771-781, May 1995.

[WOLF96] S. Wolfram, *The Mathematica Book*, Wolfram Media, Champaign, Illinois, USA, 1996.

[WOLF98] D. Wolfson, B. Mikkelsen, S.L. Danielsen, H.N. Poulsen, P.B. Hansen, K.E. Stubkjaer, "Experimental and Theoretical Investigation of Electro-optic and All-optical Implementations of Wavelength Converting 2R-Regenerators", *Optical Fiber Communication Conference*, paper WB3, pp. 103-105, 1998.

[WOLF00] D. Wolfson, D. Kloch, T. Fjelde, C. Janz, B. Dagens, and M. Renaud, "40 Gb/s All-Optical Wavelength Conversion, Regeneration, and Demultiplexing in an SOA-Based All-Active Mach-Zehnder Interferometer", *IEEE Photon. Tech. Lett.*, vol. 12, no. 3, pp. 332-334, Mar. 2000.

[YAMA95] Y. Yamaguchi, A. Yamada, T. Otsubo, K. Shinone, K. Miyagi, A. Taniguchi, "Tensile Strained MQW Semiconductor Optical Amplifier", *Seventh International Conference on Indium Phosphide and Related Materials*, pp. 500-503, May 1995.

[YASE99] A.A. Yasseen, J.N. Mitchell, J.F. Klemic, D.A. Smith, and M. Mehregany, "A Rotary Electrostatic Micromotor 1x8 Optical Switch", *IEEE J. Sel. Topics in Quantum Electron.*, vol. 5, no. 1, pp. 26-32, Jan./Feb. 1999.

[ZHEN00] X. Zheng, F. Liu, and A. Kloch, "Experimental Investigation of the Cascadability of a Cross-Gain Modulation Wavelength Converter", *IEEE Photon. Tech. Lett.*, vol. 12, no. 3, pp. 272-274, Mar. 2000.

[ZHOU97] J. Zhou, M. Cada, and T. Makino, "All-Optical Bistable Switching Dynamics in 1.55-μm Two-Segment Strained Multiquantum-Well Distributed-Feedback Lasers", *IEEE. J. Light. Tech.*, vol. 15, no. 2, pp. 342-355, Feb. 1997.

APPENDIX

A

PROPAGATION EQUATIONS

The basic equations used in this thesis are the carrier rate equation and the propagation equations. The propagation equations include the travelling wave equation and the phase equations. The carrier rate equation derivation requires the use of the density-matrix approach, which is beyond the scope of this thesis. The derivation of the propagation equations is presented here, beginning with the time-independent wave equation. This derivation can be found in [AGRA86], [CAO03], and likely other texts, but is provided here for completeness.

As a starting point the time-independent wave equation is

$$\nabla^2\tilde{E} + \epsilon k_0^2 \tilde{E} = 0, \tag{A.1}$$

where $\tilde{E}$ is the complex field amplitude, k_0 is the wavenumber in free space given by $k_0 = \omega/c$, ω is the frequency, and c is the speed of light in a vacuum. The complex dielectric constant, ϵ, is defined as

$$\epsilon = 1 + \chi + j\frac{\sigma}{\epsilon_0\omega} = 1 + \chi_0 + \chi_p + j\frac{\sigma}{\epsilon_0\omega}, \tag{A.2}$$

where χ is the total susceptibility, χ_0 is the unpumped susceptibility and χ_p is the contribution due to pumping, including both optical injection and electrical

current injection. Also, ϵ_0 is the permittivity of free space and σ is the conductivity of the medium.

Now consider a plane wave travelling along the z axis. The complex amplitude of the electric field is

$$\tilde{E}(x,y,z,\omega)=\hat{\mathbf{x}}F(x,y)\tilde{G}(z,\omega), \tag{A.3}$$

where $\hat{\mathbf{x}}$ is the polarization unit vector, $F(x,y)$ is the field distribution and $\tilde{G}(z,\omega)$ describes the field in the longitudinal direction as a function of frequency. Substituting (A.3) in (A.1) yields

$$\left(\frac{\partial^2}{\partial x^2}+\frac{\partial^2}{\partial y^2}\right)F(x,y)+\left(\eta_b^2-\eta^2\right)k_0^2F(x,y)=0, \tag{A.4}$$

where

$$\eta_b^2=1+\mathrm{Re}(\chi_0)=\epsilon_b, \tag{A.5}$$

and where η_b is the background refractive index of the unpumped material and ϵ_b is the background dielectric constant. η is the effective refractive index of the guided mode. Also,

$$\frac{\partial^2}{\partial z^2}\tilde{G}(z,\omega)+\left(\eta^2+\Gamma\chi'\right)k_0^2\tilde{G}(z,\omega)=0, \tag{A.6}$$

where

$$\chi'=j\,\mathrm{Im}(\chi_0)+\chi_p+j\frac{\sigma}{\epsilon_0\omega}, \tag{A.7}$$

and where

$$\Gamma=\frac{\int_0^w\int_0^d\left|F(x,y)\right|^2\mathrm{d}x\,\mathrm{d}y}{\int_{-\infty}^{\infty}\int_{-\infty}^{\infty}\left|F(x,y)\right|^2\mathrm{d}x\,\mathrm{d}y} \tag{A.8}$$

is referred to as the confinement factor. The transverse dimensions of the waveguide are designated w and d. This term is necessary because only the portion of the mode within the active region experiences gain. The value of χ' depends on the carrier density and photon density and thus varies with z, however, these variations are small compared to the average value of χ' and also η. Thus, χ' can be considered independent of z. The solution of (A.6) is then

$$\tilde{G}(z,\omega)=\tilde{G}_0(\omega)e^{j\tilde{\beta}z}, \tag{A.9}$$

where $\tilde{G}_0(\omega)$ is the amplitude of the optical signal at the input of the SOA and $\tilde{\beta}$ is the propagation constant given by

$$\tilde{\beta}=k_0\sqrt{\eta^2+\Gamma\chi'}\approx k_0\eta\left(1+\frac{\Gamma\chi'}{2\eta^2}\right). \tag{A.10}$$

The electric field given by (A.3) is converted to the time domain through the use of the inverse Fourier transform. Thus

$$\boldsymbol{E}(x,y,z,t)=\frac{1}{2\pi}\int_{-\infty}^{\infty}\tilde{\boldsymbol{E}}(x,y,z,\omega)e^{-j\omega t}d\omega=\hat{\boldsymbol{x}}\,F(x,y)G(z,t), \tag{A.11}$$

where

$$G(z,t)=\frac{1}{2\pi}\int_{-\infty}^{\infty}\tilde{G}(z,\omega)e^{-j\omega t}\mathrm{d}\omega. \tag{A.12}$$

Substituting (A.9) and (A.10) in (A.12) yields

$$G(z,t)=\frac{1}{2\pi}\int_{-\infty}^{\infty}\tilde{G}_0(\omega)e^{j\frac{\Gamma\chi'k_0}{2\eta}z}e^{j(\beta z-\omega t)}\mathrm{d}\omega, \tag{A.13}$$

where

$$\beta=k_0\eta=\frac{\eta\omega}{c} \tag{A.14}$$

is the propagation constant. It can be assumed that the spectral width of the input optical pulses is much smaller than the carrier frequency. By defining the frequency offset from the center carrier frequency as

$$\Delta\omega = \omega - \omega_0, \tag{A.15}$$

and noting that η is a function of ω, β can be expanded in a Taylor series expansion about ω_0, giving

$$\beta(\omega) = \beta_0 + \beta_1(\Delta\omega) + \frac{1}{2}\beta_2(\Delta\omega)^2 + \cdots, \tag{A.16}$$

where

$$\beta_m = \left.\frac{\mathrm{d}^m \beta}{\mathrm{d}\omega^m}\right|_{\omega=\omega_0}. \tag{A.17}$$

Using (A.15) and (A.16), (A.13) can then be rewritten

$$\begin{aligned} G(z,t) &= \left\{ \frac{1}{2\pi}\int_{-\infty}^{\infty} \tilde{G}_0(\Delta\omega) e^{j\left[\left(\frac{\Gamma\chi' k_0}{2\eta} + \sum_{m=1}^{\infty}\frac{\beta_m \Delta\omega^m}{m!}\right)z - \Delta\omega t\right]} \mathrm{d}\Delta\omega \right\} e^{j(\beta_0 z - \omega_0 t)} \\ &= A(z,t) e^{j(\beta_0 z - \omega_0 t)} \end{aligned} \tag{A.18}$$

where $A(z,t)$ is the slowly varying envelope of the optical input pulse. Noting that

$$\frac{\partial^k}{\partial t^k} A(z,t) = \frac{1}{2\pi}\int_{-\infty}^{\infty} \tilde{G}_0(\Delta\omega)(-j\Delta\omega)^k e^{j\left[\left(\frac{\Gamma\chi' k_0}{2\eta} + \sum_{m=1}^{\infty}\frac{\beta_m \Delta\omega^m}{m!}\right)z - \Delta\omega t\right]} \mathrm{d}\Delta\omega, \quad k = 1,2,3,... \tag{A.19}$$

and taking derivative of $A(z,t)$ with respect to z yields

$$\frac{\partial A}{\partial z} - \sum_{m=1}^{\infty} \frac{\beta_m}{(-1)^m j^{m-1} m!}\frac{\partial^m A}{\partial t^m} = j\frac{\Gamma\chi' k_0}{2\eta c} A. \tag{A.20}$$

For the short lengths used in SOAs it is sufficient to retain the first term of the summation only. Noting that the group velocity is given by

$$v_g = \frac{d\omega}{d\beta} = \frac{1}{\beta_1}, \tag{A.21}$$

(A.20) can be rewritten

$$\frac{\partial A}{\partial z} - \frac{1}{v_g}\frac{\partial A}{\partial t} = j\frac{\Gamma\chi' k_0}{2\eta c}A. \tag{A.22}$$

Using (A.7) we can rewrite (A.10) as

$$\tilde{\beta} = \left[k_0\eta + \frac{k_0\Gamma \mathrm{Re}(\chi_p)}{2\eta}\right] + j\left[\frac{k_0\Gamma}{2\eta}\left(\mathrm{Im}(\chi_0 + \chi_p) + \frac{\sigma}{\varepsilon_0\omega}\right)\right], \tag{A.23}$$

which is of the form

$$\tilde{\beta} = \beta' - j\frac{1}{2}\alpha' \tag{A.24}$$

where β' is the real valued propagation constant and α' is the total attenuation coefficient (or absorption coefficient). The factor of ½ is used because it is the intensity, not the amplitude, that attenuates by α' over a unit length [SALE pg. 175]. This total attenuation accounts for the gain in the active region, waveguide losses and all other losses. As the gain applies only to the portion of the optical mode within the active region, phenomenologically α' can be expanded to

$$\alpha' = \Gamma g - \alpha. \tag{A.25}$$

where g is the gain coefficient and α is the attenuation coefficient. Finally, a term describing the change in refractive index due to pumping is introduced as

$$\Delta\eta = \frac{\mathrm{Re}(\chi_p)}{2\eta}. \tag{A.26}$$

Using (A.25), (A.24), and (A.23), (A.7) becomes

$$\chi' = -j\frac{\eta c}{\omega_0}\left(g - \frac{1}{\Gamma}\alpha\right) + 2\eta\Delta\eta . \tag{A.27}$$

Substituting (A.27) in (A.22) yields

$$\frac{\partial A(z,t)}{\partial z} + \frac{1}{v_g}\frac{\partial A(z,t)}{\partial t} = \frac{1}{2}(\Gamma g - \alpha)A(z,t) + j\Gamma k_0 \Delta\eta A(z,t), \tag{A.28}$$

which describes the pulse propagation in the SOA. $A(z,t)$ can be rewritten as

$$A(z,t) = \sqrt{P(z,t)}\, e^{-j\phi(z,t)}, \tag{A.29}$$

where $P(z,t)$ and $\phi(z,t)$ are the power and phase of the optical pulse, respectively. Substituting (A.29) in (A.28), and separating real and imaginary terms yields

$$\frac{\partial P}{\partial z} + \frac{1}{v_g}\frac{\partial P}{\partial t} = (\Gamma g - \alpha)P, \tag{A.30}$$

and

$$\frac{\partial \phi}{\partial z} + \frac{1}{v_g}\frac{\partial \phi}{\partial t} = -\Gamma k_0 \Delta\eta . \tag{A.31}$$

Finally, using a reference frame that moves with the pulse [AGRA89], defined by

$$t' = t - \frac{z}{v_g}, \tag{A.32}$$

equations (A.30) and (A.31) can be rewritten as,

$$\frac{\partial P}{\partial z} = (\Gamma g - \alpha)P, \tag{A.33}$$

and

$$\frac{\partial \phi}{\partial z} = -\Gamma k_0 \Delta\eta . \tag{A.34}$$

APPENDIX

B

SIMULATION CODE

In Chapter 4 of this thesis, numerical models were developed to simulate various configurations of SOAs, and MZI-SOAs with and without feedback. Numerous programs were used to obtain the various plots, generally with minor variations between them. Included here is an example program that might be useful for the reader who may wish to recreate some of the plots, or develop the models further for other purposes. They were written for *Mathematica*.

■ Dynamic Simulation of Proposed Mach-Zehnder Interferometer Based Flip-Flip

This program is an example of those used in the thesis. This particular program calculates the Output response of the proposed flip-flip to a Set pulse followed by a Reset pulse. It is written for *Mathematica*.

Ronnie Van Dommelen, Dalhousie University, 2005

■ Define Constants

This section defines the parameters that describe both the SOA and some details about the optical inputs.

```
a = 2.5 * 10^-16;                    (* Differential Gain [cm^2] *)
κ0 = 3 * 10^-17;                     (* Peak Material Gain Shift Constant [nm cm^-3]*)
N0 = 0.9 * 10^18;                    (* Transparency Carrier Density [cm^-3] *)
At = 2.5 * 10^8;                     (* Nonradiative Recombination Rate [s^-1] *)
Bt = 10^-10;                         (* Bimolecular Recombination Rate [cm^3 s^-1] *)
Ct = 9.4 * 10^-29;                   (* Auger Recombination Rate [cm^6 s^-1] *)
γ1 = 0.074;                          (* Material Gain Constant [cm^-1 nm^-2] *)
γ2 = 3.155 * 10^-4;                  (* Material Gain Constant [cm^-1 nm^-3] *)
λ0 = 1605;                           (* Peak Material Gain Wavelength at Transparency [nm] *)
q = 1.6 * 10^-19;                    (* Electon Charge [C] *)
L = 500 * 10^-4;                     (* Length of SOA [cm] *)
V = L (2 * 10^-4) (0.15 * 10^-4);    (* Volume of SOA Active Region [cm^3] *)
S = (2 * 10^-4) (0.15 * 10^-4);      (* Cross Sectional Area of SOA Active Region [cm^2] *)
Γ = 0.3;                             (* Optical Confinement Factor *)
α = 20;                              (* Waveguide Loss [cm^-1] *)
dNdn = -1.2 * 10^-20;                (* Change in Refractive Index with respect to Carrier Density [cm^3] *)
λprobe = 1550;                       (* Wavelength of Probe (CW Input) [nm] *)
λpumpset = 1555;                     (* Wavelength of Set Signal [nm] *)
λpumpreset = 1555;                   (* Wavelength of Reset Signal [nm] *)
J1 = 70 * 10^-3;                     (* SOA Injection Current [nm] *)
PcwdBm0 = -6;                        (* CW Input Power [dBm] *)
Powermatchingfactor = 1.02;          (* Arm-Power-Ratio *)
Plimit = 10^-9;                      (* For Debugging *)
```

■ Define Functions

This section defines some frequently used functions.

```
(* Calculates Photon Energy *)
hν[λ_] := (3 * 10^8) (6.62 * 10^-34) / (λ * 10^-9);
(* Calculates Peak Material Gain Wavelength Shift *)
λN[x_] := λ0 - κ0 (x - N0);
(* Calculates Material Gain *)
g[x_, λ_] := a (x - N0) - γ1 (λ - λN[x])^2 + γ2 (λ - λN[x])^3;
(* Calculates Spontaneous Carrier Lifetime *)
τN[x_] := (At + Bt x + Ct x^2)^-1;

(* In these functions, the dummy variable x represents the average carrier density in the SOA. In
    each case the power of the particular optical signal is calculated at the output of the SOA *)
PsetL[x_, λ_] := Pset0 Exp[(g[x, λ] Γ - α) L];
PcwL[x_, λ_] := Pcw0 Exp[(g[x, λ] Γ - α) L];
PfeedbackL[x_, λ_] := Pfeedback0 Exp[(g[x, λ] Γ - α) L];
PloopL[x_, λ_] := Ploop0 Exp[(g[x, λ] Γ - α) L];
PresetL[x_, λ_] := Preset0 Exp[(g[x, λ] Γ - α) L];
```

■ Define Input Waveforms

This section defines the Set and Reset input waveforms, as arrays, and also prepares an array representing the Feedback signal.

```
(* This variable determines the time step of the program.  The time step is
     1 ns / scale.  As the time step decreases in duration, the arrays that define the input signals
     become larger.  The input signal arrays are constructed for an arbitrary 601 ns time period. *)
scale = 10;

setsignal = {};
(* The Set signal consists of a single input pulse. *)
setstart = 50 * scale;      (* Start time of the Set pulse, unscaled time in [ns] *)
setend = 102 * scale;       (* End time of the Set pulse, unscaled time in [ns] *)
setlow = -25;               (* Set power representing a logic low [dBm] *)
sethigh = 5;                (* Set power representing a logic high [dBm] *)
(* The Set signal is defined as an input power in [dBm] for each time step. *)
For[t = 1, t < setstart, t = t + 1,  AppendTo[setsignal, {t, setlow}];];
For[
  t = setstart, t < setend, t = t + 1,  AppendTo[setsignal, {t, sethigh}];];
For[
  t = setend, t < 601 * scale, t = t + 1,  AppendTo[setsignal, {t, setlow}];];

resetsignal = {};
(* The Reset signal consists of a single input pulse. *)
resetstart = 150 * scale;     (* Start time of the Reet pulse, unscaled time in [ns] *)
resetend = 202 * scale;       (* End time of the Reet pulse, unscaled time in [ns] *)
resetlow = -22;               (* Reset power representing a logic low [dBm] *)
resethigh = 8;                (* Reset power representing a logic high [dBm] *)
(* The Reset signal is defined as an input power in [dBm] for each time step. *)
For[
  t = 1, t < resetstart, t = t + 1,  AppendTo[resetsignal, {t, resetlow}];];
For[t = resetstart, t < resetend,
  t = t + 1,  AppendTo[resetsignal, {t, resethigh}];];
For[t = resetend, t < 601 * scale,
  t = t + 1,  AppendTo[resetsignal, {t, resetlow}];];

feedbacksignal = {};
delay = 50 * scale;           (* The feedback loop delay, unscaled time in [ns] *)
 (* As an initial condition, the power in the feedback loop must be defined. *)
For[t = 1, t < (delay + 1), t = t + 1,  AppendTo[feedbacksignal, {t, -25}];];
```

■ Upper Arm of MZI

Calculates the output power and phase of the unmodulated upper arm of the MZI.

```
(* In this simulation the upper arm of the MZI is unmodulated,
   so its output power and phase can be calculated once. These parameters determine the shape of the MZI transfer
    function. Note that the feedback is assumed to be zero at this point, we are only interested in the MZI itself. *)

PsetdBm0 = -15;                          (* Power corresponding to MZI destructive interference [dBm] *)
Pset0 = 0.001 * 10^(PsetdBm0/10);        (* Convert the above value to [W] *)
Pcw0 = 0.001 * 10^(PcwdBm0/10);          (* Convert the CW input power from [dBm] to [W] *)

(* Calculate the steady state carrier density of the SOA in the lower
     arm. The factor of 1/4 accounts for losses due to couplers between the Set input and the
     SOA. Equation has been rearranged so that the terms of the equation are of the order one. *)
Clear[n1];
answer = FindRoot[
    0 == J1 τN[n1] / (q V n1) - 1 - τN[n1] (1 / 4) (PsetL[n1, λpumpset] - Pset0) / (n1 hν[λpumpset] S L) -
      τN[n1] (PcwL[n1, λprobe] - Pcw0) / (n1 hν[λprobe] S L), {n1, 2 * 10^18}];
n1 = n1 /. answer;

(* Using the carrier density,
   the power and phase of the CW light can be calculated for the lower arm. For perfect destructive interference,
   the upper arm of the MZI supplies an equal power and oppsite phase. In this simulation the power from the upper
    arm is modified slightly by the Powermatchingfactor to prevent perfect destructive interference. *)
ϕ2 = -(2 Pi L Γ (n1 - N0)) / (λprobe * 10^-7) dNdn;
Pout2 = PcwL[n1, λprobe] * Powermatchingfactor;
```

■ Initialize the Flip-Flop

Using steady state equations, the program parameters are initialized.

```
t = 1;                                          (* Initialize the time step variable *)
data = {};                                      (* Define an empty array which will hold output data *)
stream = OpenWrite["C:\data.txt"];              (* Open a file which will hold hold output data *)

PsetdBm0 = Part[Part[setsignal, t], 2];         (* Obtain the Set power for time step t *)
Pset0 = 0.001 * 10^(PsetdBm0/10);               (* Convert Set power from [dBm] to [W] *)
Pcw0 = 0.001 * 10^(PcwdBm0/10);                 (* Convert CW power from [dBm] to [W] *)

(* Calculate the steady state carrier density of the SOA in the lower arm. *)
(* The factor of 1/4 accounts for losses due to couplers between the Set input and the SOA. *)
(* Equation has been rearranged so that the terms of the equation are of the order one. *)
Clear[n1];
answer =
 FindRoot[0 == J1 τN[n1]/(q V n1) - 1 - τN[n1] (1/4) (PsetL[n1, λpumpset] - Pset0)/(n1 hν[λpumpset] S L) -
     τN[n1] (PcwL[n1, λprobe] - Pcw0)/(n1 hν[λprobe] S L), {n1, 2 * 10^18}];
n1 = n1 /. answer;

(* Using the carrier density, calculate the power and phase of the CW light in the lower arm. *)
Pout1 = PcwL[n1, λprobe];
ϕ1 = -(2 Pi L Γ (n1 - N0))/(λprobe * 10^-7) dNdn;

(* Knowing the power and phase from each arm, the total output power of the MZI is calculated. *)
(* The factor of 1/8 accounts for couplers and splitters between the MZI SOAs and the Output. *)
Pout = 1/8 (Pout1 + Pout2 + 2 Sqrt[Pout1] Sqrt[Pout2] Cos[ϕ2 - ϕ1 + Pi]);

(* Force a minimum output power from MZI. Typically not used, but useful when debugging. *)
If[Pout < Plimit, Pout = Plimit];

PoutdBm = 10 * Log[10, 10^3 * Pout];            (* Convert the Output from [W] to [dBm] *)
AppendTo[data, {t, PoutdBm}];                   (* Append this Output power to the data array *)

(* Now consider the feedback SOA *)
(* It was determined that for good XGM extinction ratio,
  the SOA input power should be -15 dBm. Also, considering the ideal case of a lumped gain of 1.6,
  the output power of the feedback SOA should be 4.6 dBm. Thus the engineered losses at the input and
    output of the SOA were determined. Expressed as gains, they are 1/50 and 1/4.4, respectively. *)
J3 = 100 * 10^-3;                               (* Injection current supplied to feedback SOA *)
PresetdBm0 = Part[Part[resetsignal, t], 2];     (* Obtain the Reset power for time t. *)
```

```
Preset0 = 0.001 * 10^(PresetdBm0/10);   (* Convert Reset power from [dBm] to [W] *)
Ploop0 = Pout / 50;                     (* Engineered loss applied to feedback signal before SOA *)

(* Calculate the steady state carrier density of the feedback SOA. *)
(* Equation has been rearranged so that the terms of the equation are of the order one. *)
Clear[n3];
answer =
 FindRoot[0 == J3 τN[n3] / (q V n3) - 1 - τN[n3] (PloopL[n3, λprobe] - Ploop0) / (n3 hν[λprobe] S L) -
    τN[n3] (PresetL[n3, λpumpset] - Preset0) / (n3 hν[λpumpset] S L), {n3, 2 * 10^18}];
n3 = n3 /. answer;

(* Using the carrier density, calculate the feedback power exiting the feedback SOA. *)
Ploopout = PloopL[n3, λprobe];   (* Feedback optical power immediately after feedback SOA *)
Ploopout = Ploopout / 4.4;       (* Engineered loss applied to feedback signal after SOA *)
(* Convert feedback power from [W] to [dBm] and record in the feedback singal data array. *)
(* A complete cycle of the feedback loop has been completed, so the loop delay must be considered. *)
AppendTo[feedbacksignal, {t + delay, 10 Log[10, Ploopout / 0.001]}];
```

■ Calculate Remaining Data Points

Use Eulers method to calculate data points for the remaining time steps.

```
(* Now calculate the remaining data points. *)
For[t = 2, t < 400 * scale, t = t + 1,
 (* Obtain the feedback optical power for time t *)
  PfeedbackdBm0 = Part[Part[feedbacksignal, t], 2];
 PsetdBm0 = Part[Part[setsignal, t], 2];   (* Obtain the Set signal power for time t *)
 Pset0 = 0.001 * 10^(PsetdBm0/10);         (* Convert Set power from [dBm] to [W] *)
 Pfeedback0 = 0.001 * 10^(PfeedbackdBm0/10);   (* Convert feedback from [dBm] to [W] *)
 Pcw0 = 0.001 * 10^(PcwdBm0/10);           (* Convert CW power from [dBm] to [W] *)

  (* Update the carrier density for the SOA in the lower arm of the MZI *)
  (* The factors of 1/4 account for losses due to couplers. *)
 deltat = (1 / scale) * 10^-9;
 slope1 =
   (J1 τN[n1] / (q V n1) - 1 - τN[n1] (1 / 4) (PfeedbackL[n1, λprobe] - Pfeedback0) / (n1 hν[λprobe] S L) -
      τN[n1] (PcwL[n1, λprobe] - Pcw0) / (n1 hν[λprobe] S L) -
      τN[n1] (1 / 4) (PsetL[n1, λpumpset] - Pset0) / (n1 hν[λpumpset] S L)) n1 L / τN[n1];
 n1 = n1 + slope1 * deltat;
```

```
(* Using the carrier density, calculate the power and phase of the CW light in the lower arm. *)
Pout1 = PcwL[n1, λprobe];
ϕ1 = - (2 Pi L Γ (n1 - N0)) / (λprobe * 10^-7) dNdn;

(* Knowing the power and phase from each arm, the total output power of the MZI is calculated. *)
  (* The factor of 1/8 accounts for couplers and splitters between the MZI SOAs and the Output. *)
Pout = 1/8 (Pout1 + Pout2 + 2 Sqrt[Pout1] Sqrt[Pout2] Cos[ϕ2 - ϕ1 + Pi]);

(* Force a minimum output power from MZI. Typically not used, but useful when debugging. *)
If[Pout < Plimit, Pout = Plimit];

PoutdBm = 10 * Log[10, 10^3 * Pout];  (* Convert the Output from [W] to [dBm] *)
AppendTo[data, {t, PoutdBm}];  (* Append this Output power to the data array *)
(* Append the time step and this Output power to the text file. *)
  (* For long data sets, it may be necessary to write data only intermitantly. *)
WriteString[stream, ToString[t], "\t", ToString[PoutdBm], "\n"];

(* Now consider the feedback SOA *)
PresetdBm0 = Part[Part[resetsignal, t], 2];  (* Obtain the Reset power for time t. *)
Preset0 = 0.001 * 10^PresetdBm0/10;  (* Convert Reset power from [dBm] to [W] *)
Ploop0 = Pout / 50;  (* Engineered loss applied to feedback signal before SOA *)

(* Update the carrier density for the feedback SOA *)
slope3 = (J3 τN[n3] / (q V n3) - 1 - τN[n3] (PloopL[n3, λprobe] - Ploop0) / (n3 hν[λprobe] S L) -
    τN[n3] (PresetL[n3, λpumpreset] - Preset0) / (n3 hν[λpumpreset] S L)) n3 L / τN[n3];
n3 = n3 + slope3 * deltat;

(* Using the carrier density, calculate the feedback power exiting the feedback SOA. *)
Ploopout = PloopL[n3, λprobe];
  (* Feedback optical power immediately after feedback SOA *)
Ploopout = Ploopout / 4.4;
  (* Engineered loss applied to feedback signal after SOA *)
  (* Convert feedback power from [W] to [dBm]. *)
  (* Record feedback optical power, noting the feedback loop delay. *)
AppendTo[feedbacksignal, {t + delay, 10 Log[10, Ploopout / 0.001]}];
];

(* Plot the Output signal. *)
plota = ListPlot[data,
   PlotJoined -> True, PlotRange -> {{0, 400 * scale}, {-42, 10}},
   Frame -> True, FrameLabel -> {"Time", "Output Power [dBm]"}]
(* Close the text file. *)
```